

**THEORETICAL INVESTIGATION ON
THERMAL PROPERTIES OF SILICON
BASED NANOSTRUCTURES**

CHEN JIE

**NATIONAL UNIVERSITY OF SINGAPORE
2011**

**THEORETICAL INVESTIGATION ON
THERMAL PROPERTIES OF SILICON
BASED NANOSTRUCTURES**

CHEN JIE

(M.Sc., Nanjing University)

**A THESIS SUBMITTED
FOR THE DEGREE OF DOCTOR OF PHILOSOPHY
DEPARTMENT OF PHYSICS
NATIONAL UNIVERSITY OF SINGAPORE**

2011

Dedicated to my wife Chunliu and our parents

THEORETICAL INVESTIGATION ON THERMAL PROPERTIES OF
SILICON BASED NANOSTRUCTURES

Copyright © 2011 by CHEN JIE. All rights reserved.

Department of Physics and Centre for Computational Science & Engineering

Block S12, 2 Science Drive 3

National University of Singapore

Singapore

117542

Email: chenjienju@gmail.com

Acknowledgements

First and foremost, I would like to express my sincere gratitude to my supervisor at National University of Singapore, Prof. Li Baowen. This thesis would not have been possible without his immense knowledge, invaluable guidance and continuous encouragement throughout the course of my candidature. Meanwhile, I am extremely grateful to my collaborator Prof. Zhang Gang at Peking University for his guidance, enthusiasm, patience and numerous discussions. Besides, I also want to thank Prof. Wang Jian-Sheng at National University of Singapore for many helpful discussions.

In addition, I want to acknowledge the financial support from President's Graduate Fellowship during my candidature.

I am also grateful to many group members and friends in Singapore for their help: Dr. Lan Jinghua, Dr. Tang Yunfei, Dr. Zhang Qi, Dr. Zhou Jie, Dr. Li Nianbei, Dr. Jiang Jin-Wu, Dr. Yang Nuo, Dr. Wu Xiang, Mr. Yao Donglai, Mr. Zhang Lifa, Ms. Zhu Guimei, Ms. Zhang Kaiwen, Ms. Shi Lihong, Mr. Liu Sha, Mr. Zhang Xun, Ms. Ma Jing, to name a few.

Finally, I would like to express my deepest gratitude to my wife Chunliu and our parents. I am always indebted for their generous support, encouragement, tolerance and love.

Table of Contents

Acknowledgements	iii
Abstract	viii
List of Publications	x
List of Tables	xii
List of Figures	xiii
1 Introduction	1
1.1 Semiconductor Nanowires	2
1.1.1 Background	2
1.1.2 Experimental Synthesis	3
1.1.3 Silicon Nanowires	5

1.2	Thermoelectrics	10
1.2.1	Thermoelectric Effect and Application	10
1.2.2	Efficiency and Challenge	12
1.2.3	Recent Advance	14
1.3	Thesis Outline	21
2	Simulation Methods	23
2.1	Brief Introduction to Molecular Dynamics	24
2.2	Stillinger-Weber Potential	27
2.3	Velocity Verlet Algorithm	29
2.4	Non-equilibrium Molecular Dynamics	30
2.4.1	Background	30
2.4.2	Effect of Heat Bath	34
2.4.3	Summary	47
2.5	Equilibrium Molecular Dynamics	47
2.5.1	Green-Kubo Formula	47
2.5.2	Overview of Different Implementations	51
2.5.3	Improvement of Accuracy	53

2.5.4	Summary	69
2.6	Brief Introduction to Lattice Dynamics	69
3	Tunable Thermal Conductivity of $\text{Si}_{1-x}\text{Ge}_x$ Nanowires	75
3.1	Motivation	76
3.2	Si/Ge Randomly Doped Nanowires	77
3.3	Si/Ge Superlattice Nanowires	82
3.4	Summary	87
4	Remarkable Reduction of Thermal Conductivity in Si Nanotubes	88
4.1	Motivation	89
4.2	Thermal Conductivity of Si Nanotubes	90
4.3	Phonon Mode Analysis	97
4.4	Summary	101
5	Phonon Coherent Resonance in Core-Shell Nanowires	103
5.1	Motivation	104
5.2	Oscillation in Heat Current Autocorrelation Function	105
5.3	Coupling Picture	115
5.4	Coherent Mechanism to Tune Thermal Conductivity	118

5.5	Summary	123
6	A Universal Gauge for Thermal Conductivity of Si Nanowires	125
6.1	Motivation	126
6.2	Universal Gauge Above Threshold	127
6.3	Deviation Below Threshold	134
6.4	Discussion and Summary	140
7	Conclusions	142
7.1	Contribution	142
7.2	Future Work and Outlook	145
	Bibliography	148

Abstract

With the continuous decrease of fossil fuel supplies but increasing demand for energy in the world, thermoelectrics has attracted wide attention in recent years due to its ability to provide sustainable energy harvested from wasted heat. It has been challenging to increase the thermoelectric efficiency over the past five decades, until very recently exciting progresses have been achieved in this field by using semiconductor nanostructures. These recent advances are achieved mainly due to the significant reduction of thermal conductivity in these low-dimensional materials. This thesis is devoted to search for various strategies that can effectively reduce thermal conductivity of semiconductor nanostructures, which is of great interest to further enhance the thermoelectric efficiency.

To begin with, we discuss some critical aspects of molecular dynamics simulations, which are used in this study to investigate the thermal properties of silicon based nanostructures. Using silicon nanowires (SiNWs) and silicon-germanium nanojunctions as examples, we study the effect of heat bath on calculated thermal properties in non-equilibrium molecular dynamics simulations. In addition, we examine different implementations of Green-Kubo formula and discuss how to improve the accuracy of thermal conductivity calculations in equilibrium molecular

dynamics simulations.

In the second part, we demonstrate through molecular dynamics simulations various strategies that can effectively reduce thermal conductivity of SiNWs, including random doping, superlattice and hollow nanostructure. These approaches belong to the incoherent mechanisms that reduce thermal conductivity by enhancing the phonon scattering rate. Moreover, we discuss in core-shell NWs an intriguing oscillation effect in heat current autocorrelation function, while the same effect is absent in pure silicon nanowires, nanotube structures and randomly doped nanowires. Detailed characterizations of the oscillation signal reveal that this intriguing oscillation is caused by the coherent resonance effect of the transverse and longitudinal phonon modes, which offers a coherent mechanism to tune thermal conductivity in core-shell NWs.

Finally, we study thermal conductivity of SiNWs with different cross sectional geometries. Interestingly, a universal linear dependence of thermal conductivity on surface-to-volume ratio is found in SiNWs with modest cross sectional area larger than about 20 nm^2 (threshold), regardless of the specific cross sectional geometry. This offers a simple approach to tune thermal conductivity by geometry. Moreover, the physical mechanisms that cause the deviation from the universal linear relation for very thin SiNWs below the threshold are also discussed.

List of Publications

- [1] [J. Chen](#), G. Zhang, and B. Li, “A universal gauge for thermal conductivity of silicon nanowires with different cross sectional geometries”, *J. Chem. Phys.* **135**, 204705 (2011).
- [2] [J. Chen](#), G. Zhang, and B. Li, “Phonon coherent resonance and its effect on thermal transport in core-shell nanowires”, *J. Chem. Phys.* **135**, 104508 (2011).
- [3] [J. Chen](#), G. Zhang, and B. Li, “Remarkable Reduction of Thermal Conductivity in Silicon Nanotubes”, *Nano Lett.* **10**, 3978 (2010).
- [4] [J. Chen](#), G. Zhang, and B. Li, “How to improve the accuracy of equilibrium molecular dynamics for computation of thermal conductivity?”, *Phys. Lett. A* **374**, 2392 (2010).
- [5] [J. Chen](#), G. Zhang, and B. Li, “Molecular Dynamics Simulations of Heat Conduction in Nanostructures: Effect of Heat Bath”, *J. Phys. Soc. Jpn.* **79**, 074604 (2010).
- [6] [J. Chen](#), G. Zhang, and B. Li, “Tunable thermal conductivity of $\text{Si}_{1-x}\text{Ge}_x$ nanowires”, *Appl. Phys. Lett.* **95**, 073117 (2009).

- [7] L. Shi, [J. Chen](#), G. Zhang, and B. Li, “Thermoelectric Figure of Merit in Ga-Doped [0001] ZnO Nanowires”, *Submitted*.
- [8] J. -W. Jiang, [J. Chen](#), J. -S. Wang, and B. Li, “Edge states induce boundary temperature jump in molecular dynamics simulation of heat conduction”, *Phys. Rev. B* **80**, 052301 (2009).

List of Tables

2.1 EMD simulation results for thermal conductivity of crystalline silicon at 1000 K.	62
3.1 The fitting parameters of thermal conductivity for both Langevin and Nosé-Hoover heat bathes.	80

List of Figures

1.1	In situ TEM images recorded during the process of Ge nanowires growth. Adapted from Ref. [7].	4
1.2	Thermoelectric module for both cooling and power generation. Adapted from Ref. [49].	11
1.3	Thermoelectric properties versus carrier concentration. Adapted from Ref. [51].	13
1.4	Thermoelectric figure of merit as a function of temperature and year illustrating important milestones. Adapted from Ref. [52].	15
1.5	Measured thermal conductivity of individual SiNWs with different diameters. Adapted from Ref. [55].	16
1.6	Measured thermal conductivity of rough SiNWs with different diameters. Adapted from Ref. [44].	17

1.7 Thermoelectric properties of rough SiNWs versus temperature. Adapted from Ref. [44].	18
1.8 Device geometries and thermal conductivity measurements. Adapted from Ref. [58].	20
2.1 Schematic picture for NEMD simulation of SiNWs.	32
2.2 Temperature profile of SiNWs in NEMD simulation.	33
2.3 Impacts of the number of heat bath layers on thermal properties of SiNWs.	36
2.4 Normalized autocorrelation function of velocity in different heat bathes.	39
2.5 Temperature profile with different number of layers of Berendsen heat bath.	40
2.6 Impacts of heat bath parameter on thermal properties of SiNWs.	42
2.7 J_{\pm} in Si/Ge nanojunctions versus heat bath parameters.	46
2.8 Time dependence of normalized heat current autocorrelation function based on different definitions of heat current.	56

2.9 Time dependence of normalized heat current autocorrelation function $Cor(t)/Cor(0)$, relative fluctuation of $Cor(t)$, and accumulative thermal conductivity κ_a for two typical realizations in a $4 \times 4 \times 4$ super cell.	58
2.10 Calculated thermal conductivity versus super cell size from different methods with first avalanche at 1000 K.	61
2.11 Raw data and the corresponding fitted curve according to double exponential fitting of the normalized heat current autocorrelation function before the cut-off time for the same two realizations shown in Fig. 2.9.	66
2.12 Typical participation ratio for bulk Si and SiNWs.	74
3.1 Normalized thermal conductivity of $Si_{1-x}Ge_x$ NWs versus Ge content at 300 K.	79
3.2 Averaged phonon participation ratio versus Ge content in $Si_{1-x}Ge_x$ NWs.	81
3.3 Schematic picture for Si/Ge superlattice nanowires.	83
3.4 Thermal conductivity κ of Si/Ge superlattice NWs versus period length at 300 K.	84

3.5 Normalized power spectrum of different atoms in Si/Ge superlattice NWs.	86
3.6 Overlap ratio of power spectrum versus period length.	87
4.1 A typical cross sectional view of SiNTs.	90
4.2 Heat current autocorrelation function and thermal conductivity of SiNWs.	92
4.3 Thermal conductivity of SiNWs and SiNTs versus cross section area at 300 K.	94
4.4 Thermal conductivity of SiNWs and SiNTs versus temperature.	96
4.5 Participation ratio of each eigen-mode for SiNTs and SiNWs with the same cross section area.	98
4.6 Normalized energy distribution on the cross section plane of SiNWs and SiNTs at 300 K.	100
5.1 Cross sectional view of [100] Ge/Si core-shell NWs.	105
5.2 Lattice constant of Ge/Si core-shell NWs versus core-shell ratio calculated after structure relaxation.	106

5.3 Time dependence of normalized heat current autocorrelation function.	108
5.4 Long-time region of normalized HCACF for different core-shell NWs.	109
5.5 Structure and temperature dependence of the oscillation effect in Ge/Si core-shell NWs.	111
5.6 Amplitude of the fast Fourier transform of the long-time region of normalized HCACF.	114
5.7 Coupling strength versus core-shell ratio in Ge/Si core-shell NWs.	118
5.8 Averaged phonon participation ratio versus core-shell ratio in Ge/Si core-shell NWs.	119
5.9 Structure dependence of thermal conductivity in Ge/Si core-shell NWs with different cross section areas at 300 K.	121
5.10 Temperature dependence of thermal conductivity reduction in Ge/Si core-shell NWs.	122
6.1 Cross sectional view of the ideal geometry and actual lattice structure of [100] SiNWs.	128

6.2 Thermal conductivity of [100] SiNWs versus surface-to-volume ratio at different temperature.	130
6.3 Normalized thermal conductivity of SiNWs versus temperature for different cross sectional geometries.	133
6.4 Averaged phonon participation ratio versus surface-to-volume ratio in SiNWs.	135
6.5 Normalized energy distribution for the localized phonon modes on the cross sectional plane of SiNWs with large cross sectional area at 300 K.	137
6.6 Normalized energy distribution for the localized phonon modes on the cross sectional plane of SiNWs with small cross sectional area at 300 K.	139

Chapter 1

Introduction

In this chapter, we introduce the background of the present study, including semiconductor nanowires and thermoelectrics. The field of semiconductor nanowires is one of the most active research areas in recent years. Semiconductor nanowires provide a unique platform to explore interesting phenomena at nanoscale, and are expected to play a critical role in future electronic, optoelectronic and thermoelectric devices. In this chapter, some aspects of the research regarding semiconductor nanowires, including experimental synthesis process, physical properties and potential applications, are reviewed, with emphasis on silicon nanowires. Moreover, the basic principles and applications of thermoelectric effect are discussed. The challenges and recent advances in thermoelectrics are also reviewed. Finally, the outline of this thesis is presented.

1.1 Semiconductor Nanowires

1.1.1 Background

Low dimensional nanostructures have attracted much attention in the last two decades, since the experimental synthesis of carbon nanotubes (CNTs) by Iijima [1] in the early 1990s. From the fundamental physics point of view, they are of great interest because they can serve as a unique platform to probe certain intriguing physical phenomena. For instance, Brandbyge *et al.* [2] studied the electrical conductance of Au nanowires in experiment based on measurements with scanning tunneling microscope. Their experimental results have shown clear signs of electrical conductance quantization in the unit of $2e^2/h$, which e is the charge of electron and h is the Planck constant. Moreover, Hu *et al.* [3] have observed the Coulomb blockade effect in silicon nanowires at room temperature, which is encouraging for the application of single-electron transistors (SETs).

In addition to the physical interest, low dimensional nanostructures are also important in industry to sustain the historical scaling trend beyond the complementary metal-oxide-semiconductor (CMOS). Novel one-dimensional (1D) nanostructures, including CNTs and semiconductor nanowires, have been proposed as the building blocks in future nanoscale devices and circuits. CNTs are constructed by rolling up graphene sheet. One unique feature of CNTs is that their electronic structure can be either metallic or semiconducting, depending on the exact way that they are wrapped up (chirality) [4]. On the one hand, this unique property makes CNTs very interesting materials with richer physics, and thus great efforts have been devoted to the field of CNTs. On the other hand, it has also hindered the applications of CNTs based devices because of the difficulties to synthesize

uniform semiconducting CNTs in experiment [5].

Compared with CNTs, semiconductor nanowires can be synthesized with reproducible electronic properties in high-yield, which is usually required for large scale commercial applications. In addition, the well-controlled nanowire growth technique facilitates that materials with distinct chemical composition, structure, size and morphology can be integrated [6]. With such an ability, it may lead to the bottom-up assembly of integrated circuits [6], which has the advantage of parallel production of massive number of devices with similar material properties.

1.1.2 Experimental Synthesis

Semiconductor nanowires are usually synthesized by using metal nanoclusters as catalysts via the vapour-liquid-solid (VLS) process. Fig. 1.1 shows the *in situ* transmission electron microscopy (TEM) images during the synthesis process of Ge nanowires adapted from Ref. [7]. In the VLS process, the metal nanoclusters are first heated above the eutectic temperature for the metal-semiconductor system of interest with the vapour-phase source of the semiconductor. The semiconductor reactant is then continuously fed into the liquid droplet, giving rise to the supersaturation of the eutectic and the nucleation of the solid semiconductor. The solid-liquid interface acts as a sink causing the continued semiconductor incorporating into the lattice and the growth of nanowire with the alloy droplet riding on the top.

The gaseous semiconductor reactants can be generated through the decomposition of precursors in a chemical vapour deposition (CVD) process, or through the momentum and energy transfer methods, such as pulsed laser ablation [8] or molecular beam epitaxy (MBE) [9] from solid targets. So far, CVD has been

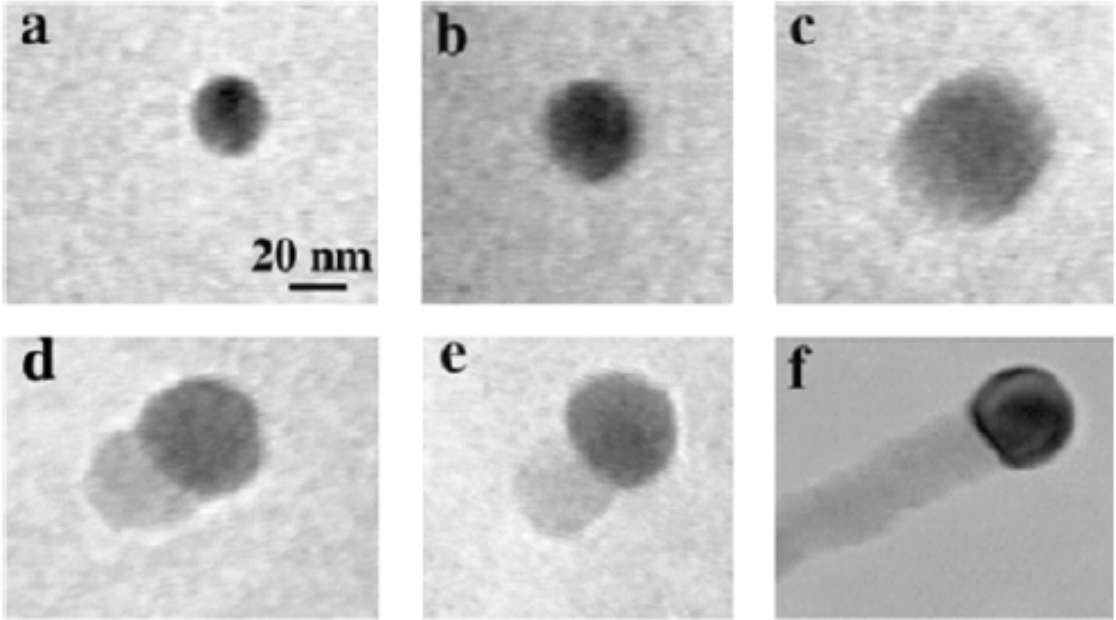


Figure 1.1: **In situ TEM images recorded during the process of Ge nanowires growth.** a Au nanoclusters in solid state at 500 °C. b Alloying initiates at 800 °C, at this stage Au exists mostly in solid state. c Liquid Au/Ge alloy. d Nucleation of Ge nanocrystal on the alloy interface. e Ge nanocrystal elongates with further Ge condensation and eventually forms a nanowire in f. Adapted from Ref. [7].

the most popular technique. In CVD-VLS growth technique, the metal nanocluster serves as the catalyst where the gaseous precursor decompose, providing the gaseous semiconductor reactants. For instance, in the growth process of silicon nanowires, silane (SiH_4) and Au nanoparticles are usually used as the precursor and catalysts, respectively. Uniform nanowires with negligible diameter variation can be achieved through careful control of the growth conditions, including the use of local heaters to reduce uncontrolled decomposition of silane [10]. The diameter

of the nanowire is determined by that of the starting nanocluster. Uniform and atomic-scale nanowires can be synthesized in a well controlled growth process as nanoclusters with diameters down to a few nanometers are now available [11].

Compared with other approaches to fabricate nanostructures, the VLS technique has one important advantage: it is possible to synthesize heterostructures at the individual device level in a controlled fashion. Both radial heterostructures, in which core-shell structure form along the radial direction [12–14], and axial heterostructures, in which sections of different materials with the same diameter such as superlattice structure are grown along the wire axis [15, 16], have been realized by using VLS growth technique. The VLS technique has now become a widely used method for producing 1D nanostructures from a rich variety of pure and doped inorganic materials that include elemental semiconductors (Si, Ge) [7, 11], III-V semiconductors (GaN, GaAs, GaP, InP, InAs) [17–21], II-VI semiconductors (ZnS, ZnSe, CdS, CdSe) [22–24]. Interested readers can refer to the experimental review by Lu and Lieber [5] for more details about the growth technique of semiconductor nanowires.

1.1.3 Silicon Nanowires

Among various semiconductor nanowires, silicon nanowires (SiNWs) have been the focus of recent studies due to the wide abundance, low cost, and high compatibility to the well developed Si-based semiconductor industry. Due to the presence of surface dangling bonds, the average coordination number of SiNWs is lower than that of bulk Si. These surface dangling bonds make the surface atoms highly reactive and induce surface reconstructions, which can minimize the Wulff energy in pristine SiNWs [25]. In experiment, the surface of SiNWs is usually passivated

in order to saturate the surface dangling bonds and assure their chemical stability.

The surface passivation in SiNWs mainly originates from two factors: (a) the thermal oxidation of Si, (b) the presence of hydrogen in the growth environment during the synthesis. Compared to hydrogen passivation, passivation by oxidation is more difficult to model in simulation as the thermal oxide is amorphous and a large amount of atoms are required to describe the disordered phase. Therefore, hydrogen passivation is usually adopted in most theoretical studies. This approach can be justified by the fact that oxide layer can be removed after growth and hydrogen passivation can be simply realized by etching the surface with HF. This procedure is often performed in experiment in order to produce cleaner surface structures [11, 26, 27].

The surface passivation is crucial for the electronic properties since the Si dangling bonds form states in the bandgap which may lead to metallic SiNWs [28]. About the thermal properties, however, previous theoretical study [29] has shown that thermal conductance of SiNWs considering hydrogen passivation has a maximum deviation of 3% at different temperature as compared to the pure Si calculations. Therefore, leaving out the hydrogen in the empirical potential calculations is justified, and this approach has been widely used in many theoretical studies on thermal properties of nanostructures.

One of the most intriguing phenomena that arise in confined systems like SiNWs is the well-known quantum confinement, which is usually described by the particle-in-a-box model in most quantum mechanics text books. The confinement effect can be simplified as an infinite potential well where motions of particles are restricted in the direction of the confinement. In the presence of the infinite

potential well, the energies of the electron eigenstates are given by

$$E_n = \hbar^2 n^2 \pi^2 / (2m^* d^2), \quad (1.1)$$

where m^* is the effective mass, and d is the width of the potential well. We can see from Eq. (1.1) that quantum confinement has a critical impact on semiconductors because it directly affects their most important electronic property: the energy band gap, especially for smaller d . First principles calculations [30, 31] with realistic potential have shown that the band gap of SiNWs can be described as

$$E_{gap} = E_{gap}^{bulk} + C/d^\alpha, \quad (1.2)$$

where E_{gap}^{bulk} is the band gap of bulk silicon, and C is a constant. The exponent α for actual SiNWs deviates from the prediction of particle-in-a-box model ($\alpha = 2$) where infinitely high barrier is considered, and depends on the diameter [30, 31]. This diameter dependence of band gap is indeed observed in experiment by using scanning tunneling spectroscopy measurements [26]. Moreover, the band gap of SiNWs is strongly anisotropic among different orientations [31–33]. For SiNWs of comparable diameters, it follows the following order [34]

$$E_{gap}^{[100]} > E_{gap}^{[111]} \sim E_{gap}^{[112]} > E_{gap}^{[110]}, \quad (1.3)$$

where the band gap in [111] and [112] is close to each other [32, 33].

Although the band gap of SiNWs is highly anisotropic and also strongly depends on the diameter, it is rather insensitive to the cross sectional shape. Ng *et al.* [33] studied the effect of cross sectional shape on the band gap of SiNWs based on density-functional theory (DFT) calculations. 13 SiNWs with different cross sections are constructed by modifying [110] SiNWs with a diameter ~ 1 nm. They

found the band gap of these 13 SiNWs is almost constant, with insignificant variance within 0.09 eV. Later, Yao *et al.* [35] further demonstrated that SiNWs with different cross sections can have the same band gap, provided that their surface-to-volume ratio (SVR) is the same. They found the band gap of SiNWs with different cross sectional shapes has a universal relation with SVR as

$$E_{gap} = E_{gap}^{bulk} + aS, \quad (1.4)$$

where a is an adjustable parameter, and S is the value of SVR in the unit of nm⁻¹.

Bulk Si is not a good material for photonics applications due to its indirect band gap. For the electronic band structure of bulk Si, its valence band (VB) maximum is located at the Γ point, and its conduction band (CB) minimum is located approximately 85% from Γ to X [35]. In order to conserve the momentum, the indirect band gap requires the phonon to participate in the electronic transition, which is harmful to the practical applications such as light-emitting diode (LED).

As the dimension of Si shrinks from bulk to nanoscale, quantum confinement effect induces modifications to the electronic band structure, which increases the energy of CB and decreases the energy of VB, resulting in the increase of the band gap. Moreover, the modifications of the energy caused by the quantum confinement is different for each point in the Brillouin zone, and depends on the effective mass and orientation of the nanowire. The effective mass of electrons in bulk Si is higher at Γ point than at X point. Therefore, it can be easily understood from the effective mass theory that the energy of CB will be increased more at X point than at Γ point [36]. For SiNWs with sufficiently small diameter, this difference in energy modifications at different points in the Brillouin zone is sufficiently large to relocate the CB minimum to Γ point, and causes the material to undergo a transition from

the indirect to direct band gap. Detailed first-principles calculations of the band structure of SiNWs have shown that the critical size, at which this indirect to direct transition takes place, depends on the orientation and surface structure of SiNWs [36].

The direct band gap of SiNWs has inspired the use of SiNWs as optically active materials for photonics applications. For instance, Guichard *et al.* [37] have experimentally demonstrated the visible and near-infrared photoluminescence (PL) in SiNWs at room temperature. In their experiment, SiNWs with average diameter of 20 nm were etched and oxidized to passivate the nanowires. They found PL emission blue shifted continuously with the decrease of nanowire diameter. Furthermore, slowed oxidation was observed for small diameter SiNWs, which provides a high degree of control over the emission wavelength. Their study has encouraged the realization of a range of SiNW-based photonic devices using CMOS-compatible fabrication methods.

In addition to the photonic applications, many other applications of SiNWs have been demonstrated, ranging from high-performance field-effect transistors (FETs) [38], logic gates [39], nonvolatile memories [40], photovoltaics [41], to biological sensors [42, 43]. Moreover, giant piezoresistance effect [27] and enhanced thermoelectric performance [44, 45] in SiNWs have also been reported. Interested readers can refer to many review articles [46–48] for more information about the applications of SiNWs.

1.2 Thermoelectrics

1.2.1 Thermoelectric Effect and Application

The thermoelectric (TE) effect arises from the fact that when the charge carriers in metals or semiconductors move inside the materials like gas molecules, they are carrying charge as well as heat at the same time. When a temperature gradient is applied to TE material, the mobile charge carriers will diffuse from the hot side to the cold side, which leads to the accumulation of charge carriers at the cold side and a build-up electric voltage across the material. This effect is known as Seebeck effect and is the basis for TE power generation. On the other hand, when applying an electric voltage to TE material, the charge carriers will be driven by the electric voltage to one side of the material, therefore cooling the other side of the material. This effect is known as Peltier effect and has been used for TE cooling. Fig. 1.2 adapted from Ref. [49] shows the typical framework of a TE module for both cooling and power generation. This TE module contains many TE couples consisting of n-type and p-type TE elements that are connected electrically in series and thermally in parallel. Cooling or power generation can be realized in the same device by applying external electric power supply or temperature gradient.

With the continuous decrease of fossil fuel supplies but increasing demand for energy in the world, thermoelectrics has attracted significant attention because it can provide sustainable energy harvested from wasted heat. As the environmental impact of global climate change due to the combustion of fossil fuel is becoming increasingly alarming, TE module for power generation has the advantage of being environmentally friendly. In addition, as TE module is solid-state device without any moving parts, it is silent, reliable and scalable, which makes it ideal for small

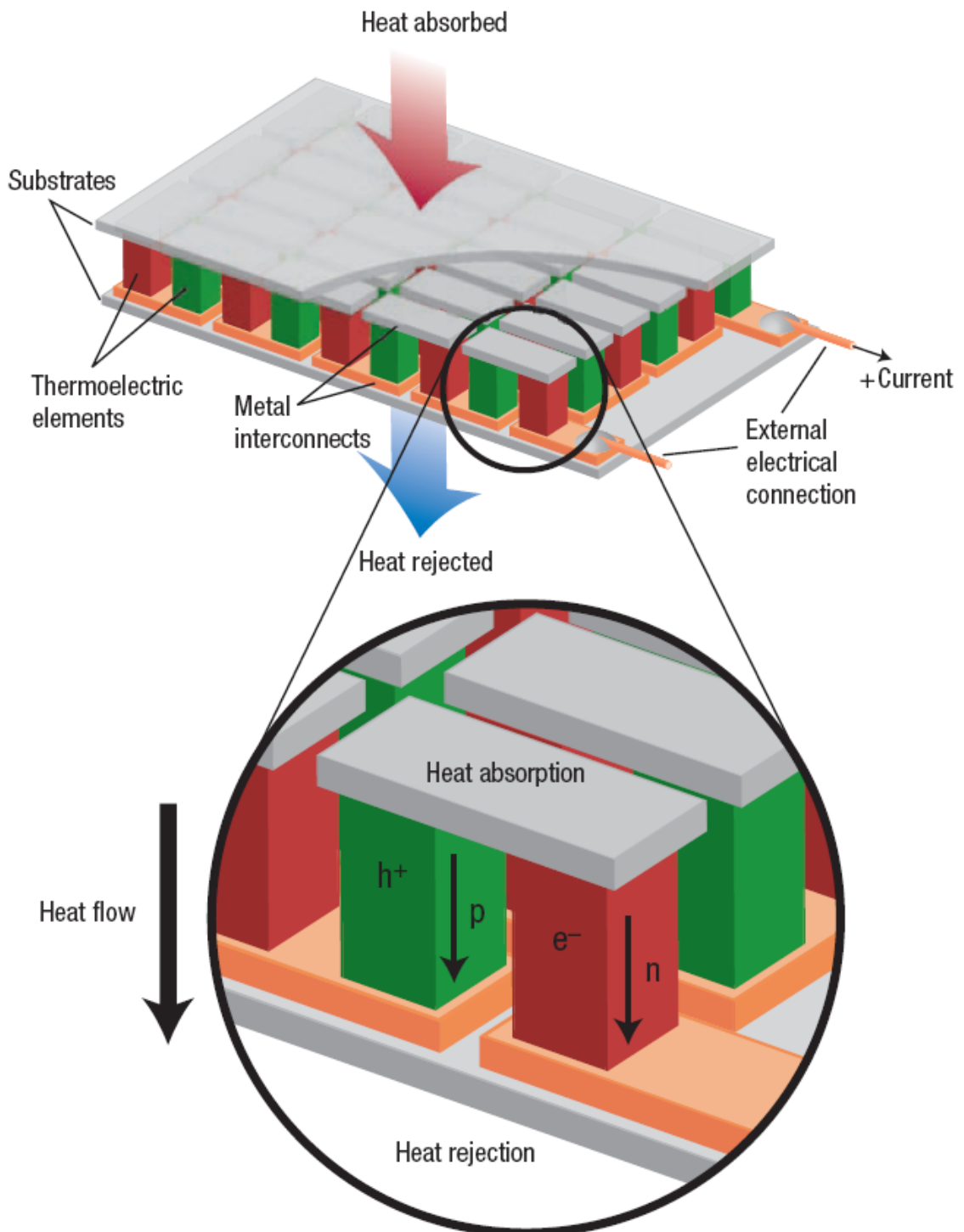


Figure 1.2: **Thermoelectric module for both cooling and power generation.** Adapted from Ref. [49].

and distributed power generation.

1.2.2 Efficiency and Challenge

The performance of TE materials can be characterized by the dimensionless quantity known as thermoelectric figure of merit ZT defined as

$$ZT = S^2 \sigma T / \kappa, \quad (1.5)$$

where S , σ , T , and κ are, respectively, the Seebeck coefficient, electrical conductivity, absolute temperature, and thermal conductivity. For a TE device, the maximum efficiency η can be evaluated by the following equation [49]

$$\eta = \eta_c \frac{\sqrt{1 + Z\bar{T}} - 1}{\sqrt{1 + Z\bar{T}} + T_C/T_H}, \quad (1.6)$$

where T_C and T_H are the temperature of the cold and hot side, respectively, $\bar{T} = (T_C + T_H)/2$ is the average temperature, and $\eta_c = (T_H - T_C)/T_H$ is the Carnot efficiency.

Because of the interrelationship between those quantities in Eq. (1.5), it has been very challenging to enhance ZT of a conventional bulk material. For instance, the Seebeck coefficient of metals or degenerate semiconductors is given by [49]

$$S = \frac{8\pi^2 k_B^2}{3e h^2} m^* T \left(\frac{\pi}{3n} \right)^{2/3}, \quad (1.7)$$

where e is the charge of electron, n is the carrier concentration, and m^* is the effective mass of the carrier. Therefore, materials with low carrier concentration have large Seebeck coefficient. On the other hand, the electrical conductivity is proportional to the carrier concentration as

$$\sigma = ne\mu, \quad (1.8)$$

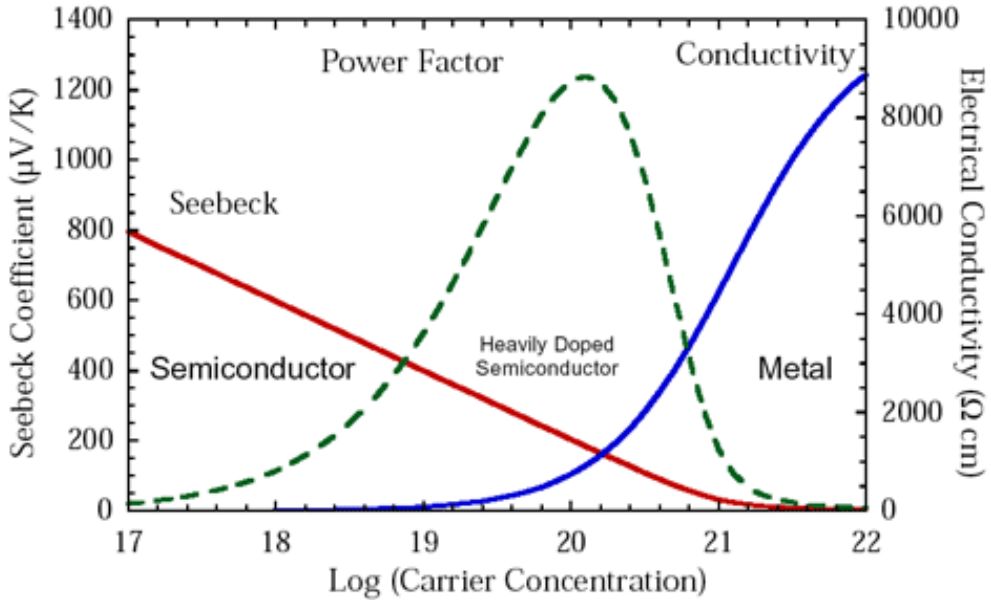


Figure 1.3: **Thermoelectric properties versus carrier concentration.**

Trends shown here are modeled from Bi_2Te_3 based on empirical data in Ref. [50]. The red solid line and blue solid line denote Seebeck coefficient and electric conductivity, respectively. The green dashed line denotes power factor. Adapted from Ref. [51].

where μ is the carrier mobility.

Due to the opposite trend of Seebeck coefficient and electrical conductivity with respect to carrier concentration, thermoelectric power factor ($S^2\sigma$) of a material has a maximum peak at some optimal carrier concentration, as shown in Fig. 1.3. This peak depends on particular material system and typically occurs at carrier concentration between 10^{19} and 10^{21} carriers per cm^3 , which falls in between common metals and heavily doped semiconductors [49]. A similar balance must be considered for the effective mass because large effective mass can increase the Seebeck coefficient, but at the same time decrease the carrier mobility, thus resulting

in the decrease of electrical conductivity.

Other conflicting factors in achieving high ZT include electric and thermal conductivity. Thermal conductivity in TE materials stems from two contributions

$$\kappa = \kappa_e + \kappa_l, \quad (1.9)$$

where κ_e denotes the electric contribution from charge carrier (electron or hole), and κ_l denotes the lattice contribution from phonon. Most of the electric term κ_e is directly related to electrical conductivity through the Wiedemann-Franz law

$$\kappa_e = L\sigma T, \quad (1.10)$$

where L is the Lorenz factor. Therefore, the increase of electrical conductivity can induce the increase of electric contribution to thermal conductivity, which makes it difficult to enhance ZT .

1.2.3 Recent Advance

While each property of ZT (S , σ , and κ) can individually be changed by several orders of magnitude, the interrelationships between these properties as mentioned above have made it extremely challenging to enhance $ZT > 1$ in the past five decades until the recent decade. Fig. 1.4 adapted from Ref. [52] highlights some of the significant progresses in producing high ZT materials in recent years. The significant enhancement of ZT in various materials results from two different strategies widely used in TE community. One is to develop the next generation TE materials by using advanced novel bulk materials [53]. The basic idea is to design novel bulk materials that contain heavy-ion species with large vibrational amplitudes at partially filled structural sites, thereby providing effective phonon scattering centers [54].

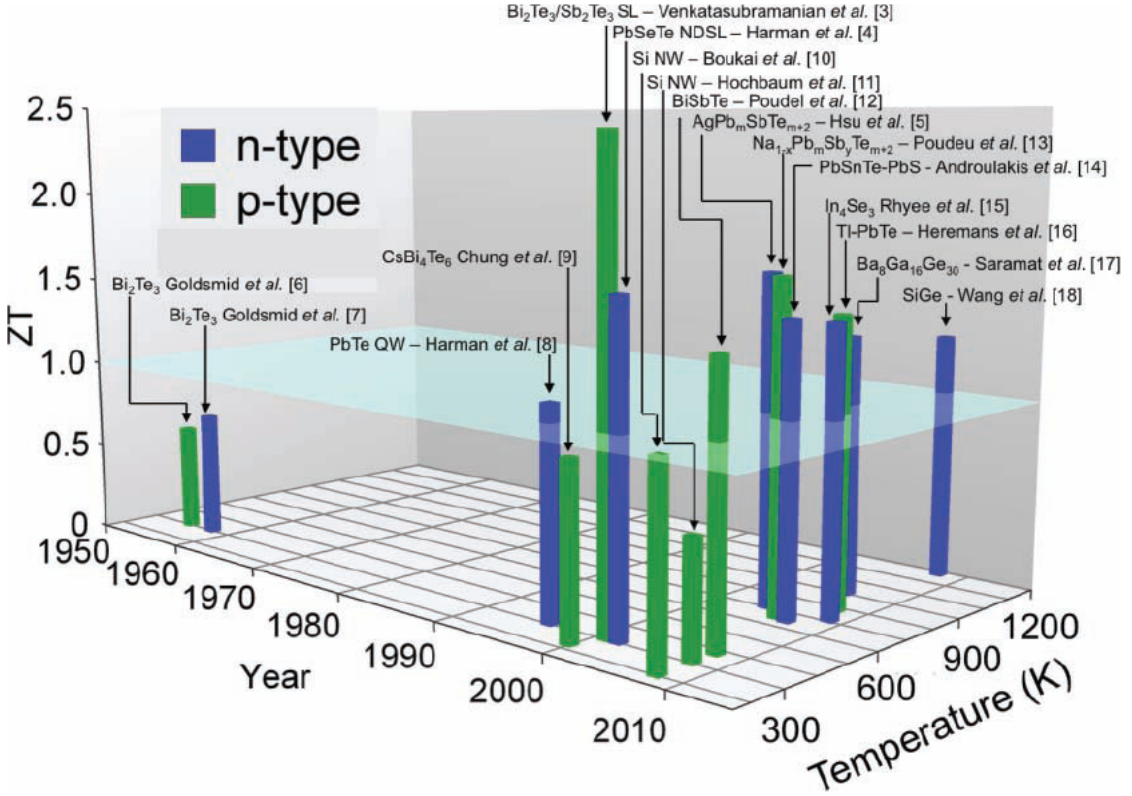


Figure 1.4: Thermoelectric figure of merit ZT as a function of temperature and year illustrating important milestones. Adapted from Ref. [52]. All references listed in this figure should be referred to Ref. [52].

The other widely used strategy is to use nanostructure materials. Nanostructure materials are quite different from their bulk counterparts in the sense that their properties are usually size-dependent. For instance, Li *et al.* [55] measured thermal conductivity of individual single crystalline SiNWs with different diameters using a microfabricated suspended device. Fig. 1.5 shows their measurement results over the temperature range from 20 to 320 K. They found thermal conductivity of SiNWs depends on the diameter remarkably and is more than two orders

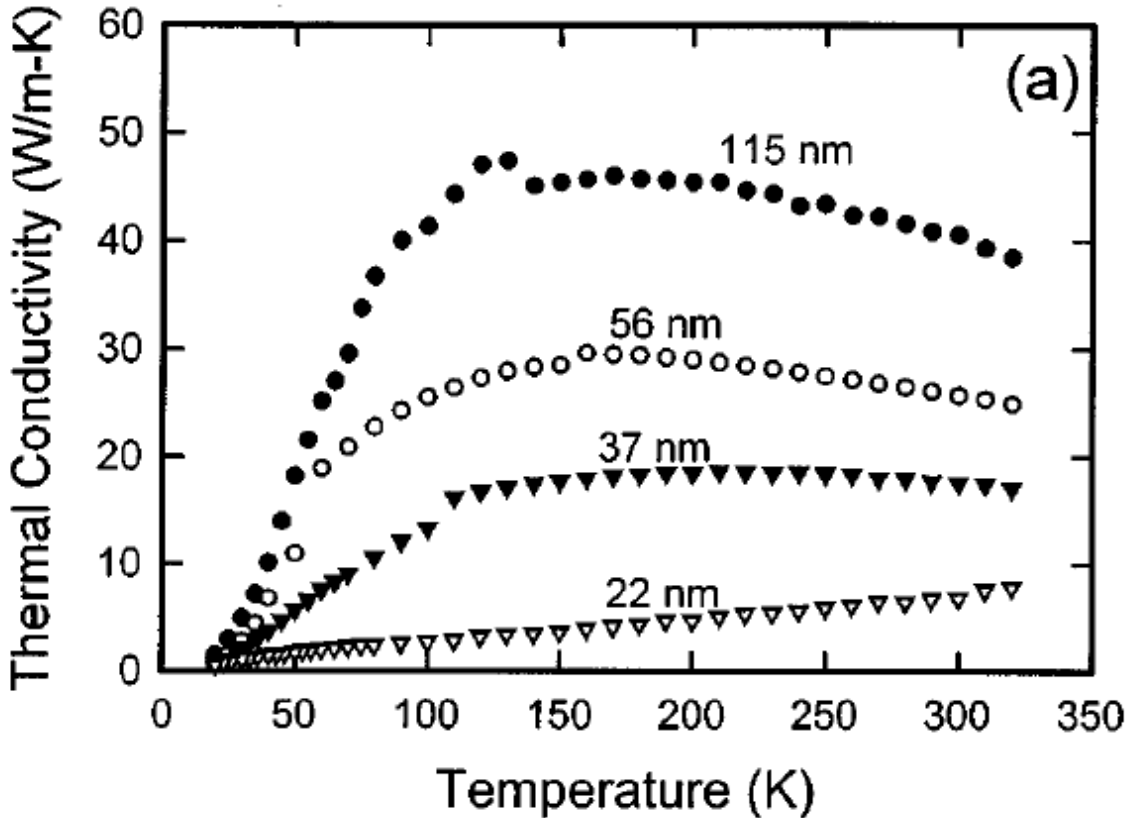


Figure 1.5: Measured thermal conductivity of individual SiNWs with different diameters. Adapted from Ref. [55].

of magnitude lower than the bulk value.

Bulk Si is a poor TE material due to its high thermal conductivity (~ 150 W/mK at room temperature), leading to $ZT \approx 0.01$ at 300 K [56]. The huge reduction of thermal conductivity in SiNWs has inspired the effort to develop high ZT material based on Si. This idea has been demonstrated by Hochbaum and Chen *et al.* [44] based on rough SiNWs. Due to the surface roughness introduced by etching in the synthesis, as shown in Fig. 1.6 , thermal conductivity of rough SiNWs is further reduced compared with single crystalline SiNWs, approaching the

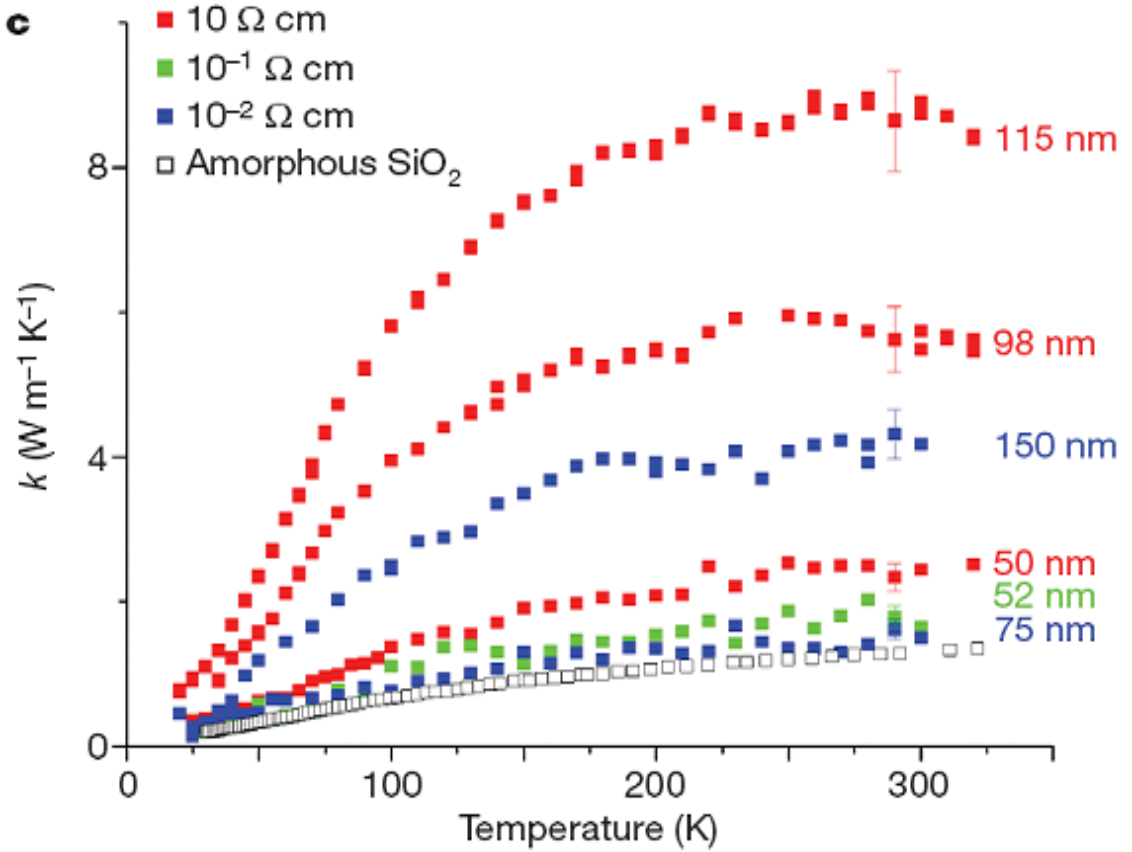


Figure 1.6: **Measured thermal conductivity of rough SiNWs with different diameters.** Adapted from Ref. [44].

amorphous limit for Si [57] ($\sim 1 \text{ W/mK}$). As shown in Fig. 1.7, their experimental results demonstrate that by significantly reducing thermal conductivity without affecting too much the power factor, ZT of rough SiNWs can be largely enhanced to about 1 at room temperature, which is about 2 order of magnitude enhancement compared to bulk Si. The same idea has been independently demonstrated at the same time by Boukai and Bunimovich *et al.* [45] with very thin SiNWs. Their experimental results have shown that $ZT \approx 1$ can be achieved with 20 nm wide

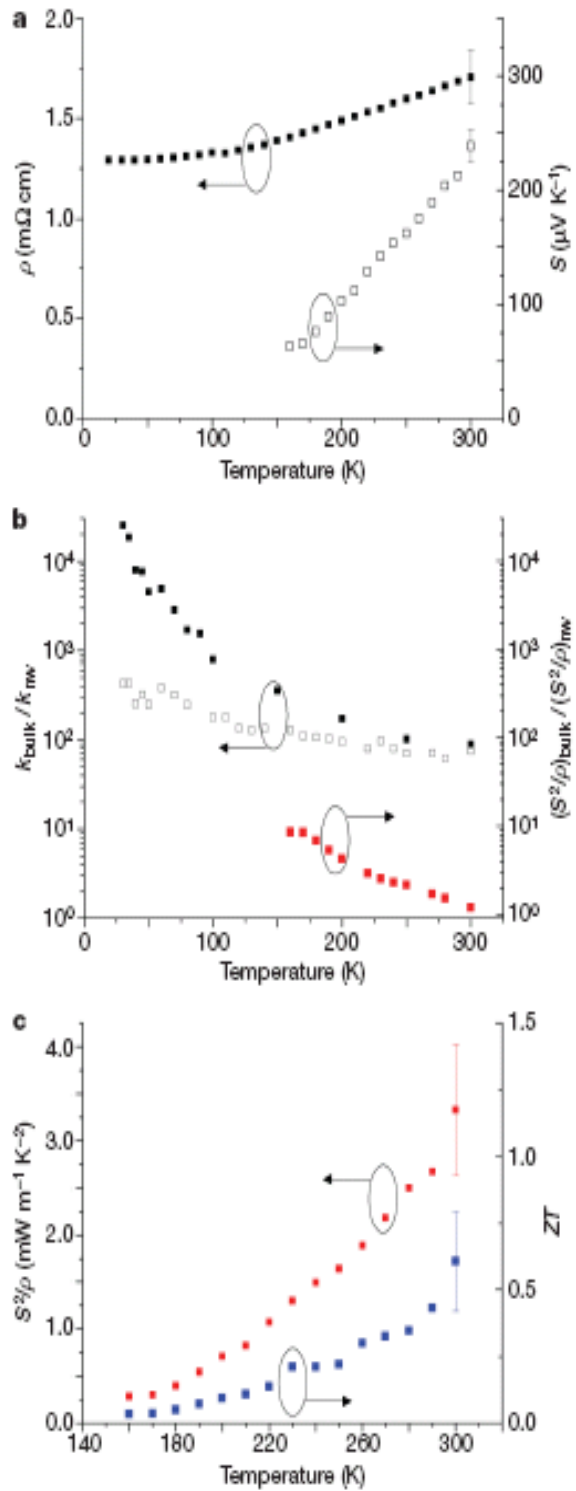


Figure 1.7: Thermoelectric properties of rough SiNWs versus temperature. Adapted from Ref. [44].

SiNWs at 200 K.

The significant reduction of thermal conductivity in these studies result from the enhanced surface scattering, either by etching the surface or reducing the diameter of the nanowires, which is the incoherent mechanism to reduce thermal conductivity. Very recently, the coherent mechanism to lower thermal conductivity by modifying phonon band with periodic structures has attracted much attention. Yu and Mitrovic *et al.* [58] have demonstrated this coherent mechanism through the nanomesh structures. As shown in Fig. 1.8a, they introduce nanoscale meshes (NM) in a periodic fashion to the Si thin film. Three reference devices are fabricated for comparison: nanowire array (NWA), thin film (TF), and large feature-size mesh produced by electron-beam lithography (EBM). They found thermal conductivity of NM is the lowest, approaching the amorphous limit for Si, even lower than that of NWA which has a higher surface-to-volume ratio. The low thermal conductivity of NM is attributed to the Brillouin-zone folding introduced by the periodic NM structure. As a result, the phonon bands are folded and considerably flattened when compared to bulk Si bands. Further study has demonstrated that thermoelectric performance of such holey Si thin film can be largely enhanced to $ZT \approx 0.4$ at room temperature, by reducing the pitch of the hexagonal holey pattern down to 55 nm with 35 % porosity [59].

The widely used commercial thermoelectric materials are bismuth-telluride based semiconductors, with $ZT \approx 1$ at room temperature. However, due to the limited availability, it is quite difficult to scale bismuth-telluride to large-scale. In addition, it is also expensive to fabricate nanostructures based on bismuth-telluride. These drawbacks of bismuth-telluride based semiconductors greatly limit their large-scale application in energy conversion. Silicon, on the other hand, is

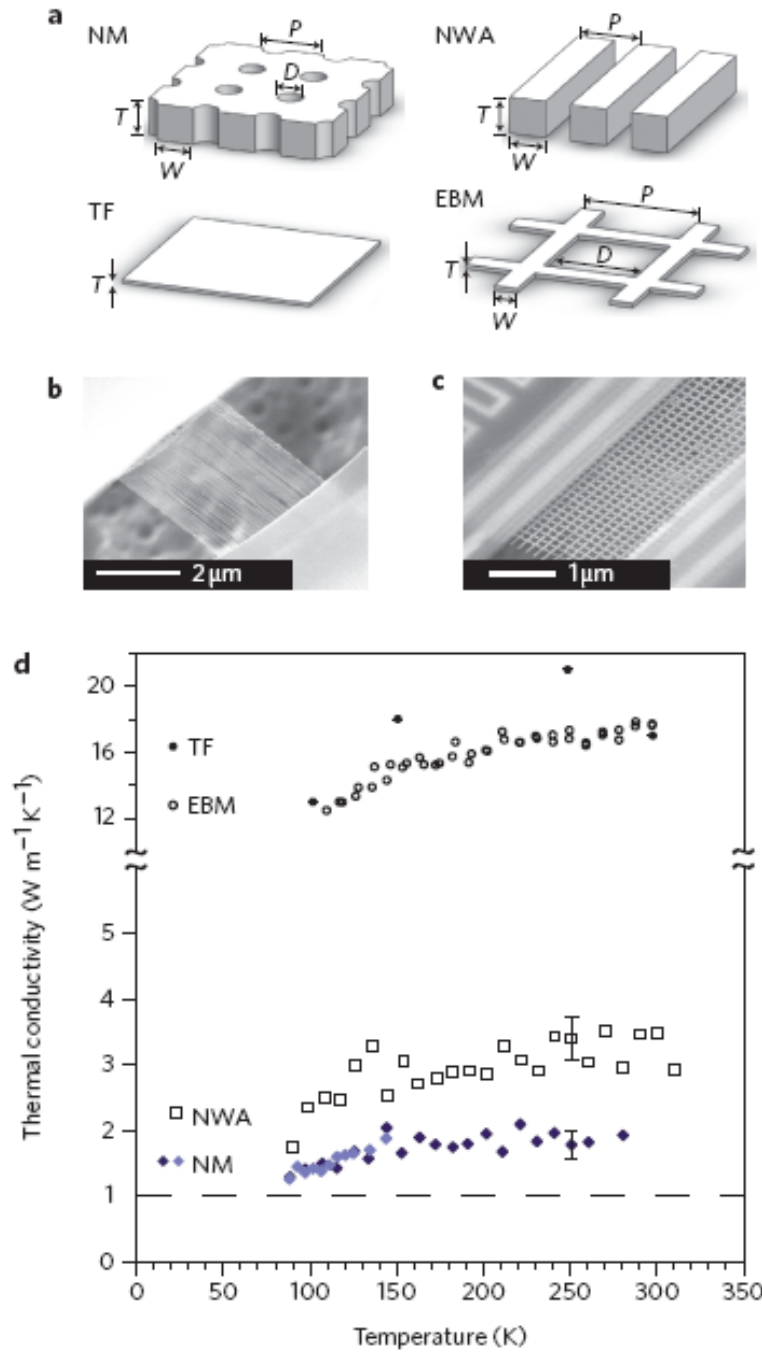


Figure 1.8: **Device geometries and thermal conductivity measurements.**

Thermal conductivity of nanomesh (NM) structure is compared with that of three reference devices: nanowire array (NWA), thin film (TF), and large feature-size mesh produced by electron-beam lithography (EBM). Adapted from Ref. [58].

the most abundant and widely used semiconductor, with a large industrial infrastructure for low-cost and high-yield production. A number of recent studies [44, 45, 58, 59] have demonstrated the feasibility to develop high efficiency thermoelectric devices based on Si. Moreover, all these recent advances have suggested that low thermal conductivity is a dominant factor to achieve high ZT in these Si based nanostructures. From this point of view, in order to further enhance ZT , it is crucial and desirable to further reduce thermal conductivity of Si based nanostructures through nanoscale engineering.

1.3 Thesis Outline

The rest part of this thesis is organized as follows:

In Chapter 2, we first introduce molecular dynamics (MD) simulations that are used in this study to calculate thermal conductivity of Si based nanostructures. We then discuss our works on MD methodology in two aspects. One is the effect of heat bath on calculated thermal properties in non-equilibrium MD simulation, and the other is to improve the accuracy of thermal conductivity prediction based on Green-Kubo formula in equilibrium MD simulation. Finally, the basic principles of lattice dynamics, which is used in this study to calculate the phonon eigen-modes and explore the phonon localization effect in nanostructures, are briefly introduced.

In Chapter 3, we demonstrate that thermal conductivity of SiNWs can be effectively reduced by randomly doping Ge atoms. The composition dependence of thermal conductivity in Si-Ge nanowires is explained in terms of localization effect of phonon modes. In addition, thermal conductivity of Si/Ge superlattice structured NWs with changeable period length is also studied. The dependence of

thermal conductivity on the period length is explained by the overlap of phonon power spectrum.

In Chapter 4, we propose to reduce thermal conductivity of SiNWs by introducing small hole at the center, i.e., construct silicon nanotube structures. Using equilibrium MD simulation, thermal conductivity of SiNTs is calculated, which shows remarkable reduction of thermal conductivity compared with SiNWs. The physical mechanism responsible for the remarkable reduction is discussed based on phonon mode analysis.

In Chapter 5, we discuss in core-shell NWs an intriguing oscillation effect in heat current autocorrelation function, while the same effect is absent in pure silicon nanowires, nanotube structures and randomly doped nanowires. The physical origin of this oscillation effect is uncovered through detailed characterizations of the oscillation signal. Moreover, we further reveal a coherent mechanism to tune thermal conductivity in core-shell NWs by utilizing this oscillation effect.

In Chapter 6, we study thermal conductivity of SiNWs with different cross sectional geometries. We found a universal linear dependence of thermal conductivity on surface-to-volume ratio among different cross sectional geometries, when the cross sectional area is greater than certain threshold. Moreover, the physical mechanisms that cause the deviation from the universal linear relation for very thin SiNWs below the threshold are also discussed.

Finally, we summarize this thesis and give the conclusions in Chapter 7.

Chapter 2

Simulation Methods

In this chapter, we first introduce the basic principles of molecular dynamics (MD) simulations, which are used in this study to investigate the thermal properties of silicon based nanostructures. After introducing the force field and numerical integration algorithm used in our simulations, we present our works on MD methodology in the following two aspects. One is the effect of heat bath on calculated thermal properties in non-equilibrium MD simulations, and the other is to improve the accuracy of thermal conductivity prediction based on Green-Kubo formula in equilibrium MD simulations. Finally, we briefly introduce the the basic principles of lattice dynamics, which is used in this study to calculate the phonon eigen-modes and explore the phonon localization effect in nanostructures.

2.1 Brief Introduction to Molecular Dynamics

The physical properties of the matter are to be found in the structure and motion of its constituent building blocks, and the dynamics is contained in the solution to the many-body problem. The many-body problem originated from the dynamics of the solar system, and its analytic solution turns out to be insoluble for three or more bodies. Although it is quantum mechanics instead of classical mechanics that describes the fundamental physics of condensed matter, the attempt to numerically solve the Schrödinger equation for a system of many nuclei and electrons is too formidable and not at all feasible in practice. Thus, one has to resort to approximations.

Molecular dynamics (MD) simulation is an extremely powerful tool to handle many-body problems at atomic level based on classical mechanics, which numerically solves Newton's equation of motion for a many-body system. It has the advantage of simulating realistic material with accurate many-body interatomic interaction obtained from first-principles calculations, which was not available but simplified by the two-body potentials with analytical form in the earlier theoretical model. The applications of MD simulation have covered a wide range of research topics, such as liquids [60], defects [61], fatigue [62], surface [63, 64], clusters [65, 66], biomolecules [67]. Therefore, MD simulation has become indispensable in today's research of physical and material science.

The typical feature size that current first-principle calculations, such as density-functional theory (DFT), can be used to explore the thermal properties of nanostructures is on the order of several nm [29, 68, 69]. With MD simulations, the system size under study can be enlarged a lot. For instance, MD simulations of

silicon nanowires with length up to μm [70] and cross sectional area up to 806 nm^2 [71] have been reported. Moreover, Markussen *et al.* [29] studied thermal properties of thin silicon nanowires with both DFT and classical calculations based on Tersoff potential. They found calculation results of thermal conductance obtained from DFT and Tersoff calculations agree within 10% [29].

The validity of the classical approximation can be evaluated based on the de Broglie thermal wavelength [72] defined as

$$\Lambda = \sqrt{\frac{2\pi\hbar^2}{mk_B T}}, \quad (2.1)$$

where \hbar is Planck's constant, m is the atom mass, k_B is Boltzmann's constant, and T is the temperature. The classical approximation is valid if $\Lambda \ll a$, where a is the nearest neighbor separation. Under this condition, the entire system can be treated as the dilute gas model based on which the classical kinetic gas theory is formulated [73]. In this case, each molecule can be considered as a classical particle with a well-defined position and momentum. Moreover, different molecules are distinguishable from each other [73]. Take the diamond structured silicon for instance, its lattice constant is $L_0=5.43 \text{ \AA}$, and $a=\sqrt{3}L_0/4=2.35 \text{ \AA}$. The de Broglie thermal wavelength at room temperature is $\Lambda=0.19 \text{ \AA}$, which is one order of magnitude smaller than the nearest neighbor separation. Therefore, for the group IV semiconductors with diamond structure considered in this study, such as silicon and germanium, the classical approximation is appropriate above room temperature from the dilute gas point of view. Furthermore, quantum effects become important for any system when the temperature is sufficiently low. The drop of the heat capacity for crystals below the Debye temperature is a well known example of measurable quantum effects in solids. This is of particular importance in the study of thermal transport [74].

In the context of thermal transport, MD simulation is a statistical mechanics approach, which relates the microscopic behavior in a system with its thermodynamics. According to statistical mechanics, physical quantities can be evaluated by averaging over configurations distributed according to a certain statistical ensemble. For the N -particle system, MD simulation calculates the trajectory in a $6N$ -dimensional phase space ($3N$ positions and $3N$ momenta) at each instantaneous time. This trajectory obtained from MD simulation provides such a set of configurations. To get the thermodynamic variables such as temperature, it relies on the ergodicity hypothesis of statistical mechanics, which asserts that the phase space can be fully recovered in the long time limit and the time average is equivalent to the ensemble average. Therefore, thermodynamic variables of interest can be obtained by the time average along the trajectory in MD simulation.

A typical procedure of MD simulation can be described by the following key steps. To begin with, an appropriate force field that can accurately describe the interatomic interaction in the system of interest is required. The next step is to construct the initial position and velocity of each atom in the system, and generate the list for the nearest neighbor interaction. Usually atoms are initially located at their equilibrium positions and assigned with random velocity according to Gaussian distribution. After that, one calculates the force applied to each atom according to the force field, numerically solves Newton's equation of motion, and updates the position and velocity of each atom. This is the major step in MD simulation, which involves many technical details such as boundary conditions, numerical integration algorithm, and heat bath (reservoir) that can realize the canonical ensemble. Finally, one calculates the ensemble average of the thermodynamic variables of interest with long enough simulation time.

2.2 Stillinger-Weber Potential

In general, the potential energy for a N -particle system can be resolved into contributions from one-body, two-body, three-body, etc., interaction as follows:

$$\begin{aligned} V(\mathbf{r}_1, \mathbf{r}_2, \mathbf{r}_3, \dots, \mathbf{r}_N) &= \sum_i v_1(\mathbf{r}_i) + \sum_{\substack{i,j \\ i < j}} v_2(\mathbf{r}_i, \mathbf{r}_j) \\ &\quad + \sum_{\substack{i,j,k \\ i < j < k}} v_3(\mathbf{r}_i, \mathbf{r}_j, \mathbf{r}_k) + \dots + v_N(\mathbf{r}_1, \mathbf{r}_2, \dots, \mathbf{r}_N), \end{aligned} \quad (2.2)$$

where v_N denotes the N -body interaction, and \mathbf{r}_i denotes the position of atom i . The one-body term normally describes the external force applied to the system, which can be neglected for the isolated system. The higher order terms usually contribute less to the total energy compared to the lower order terms. Stillinger-Weber (SW) potential is a Keating type potential [75] and consists of the two-body and three-body term defined as [76]

$$v_2(\mathbf{r}_i, \mathbf{r}_j) = \epsilon f_2(r_{ij}/\sigma), \quad (2.3)$$

$$v_3(\mathbf{r}_i, \mathbf{r}_j, \mathbf{r}_k) = \epsilon f_3(\mathbf{r}_i/\sigma, \mathbf{r}_j/\sigma, \mathbf{r}_k/\sigma), \quad (2.4)$$

where r_{ij} is the distance between atom i and j , and ϵ and σ denotes the energy and length unit, respectively. These two units are determined in such a way that ϵ is chosen to give f_2 depth -1, and σ is chosen to make $f_2(2^{1/6})$ vanish.

The reduced pair potential f_2 reads

$$f_2(r) = \begin{cases} A(Br^{-p} - r^{-q}) \exp[(r - a)^{-1}], & r < a \\ 0, & r \geq a \end{cases} \quad (2.5)$$

where a is the cutoff distance above which interaction vanishes. The three-body interaction f_3 is defined as

$$f_3(\mathbf{r}_i, \mathbf{r}_j, \mathbf{r}_k) = h(r_{ij}, r_{ik}, \theta_{jik}) + h(r_{ji}, r_{jk}, \theta_{ijk}) + h(r_{ki}, r_{kj}, \theta_{ikj}), \quad (2.6)$$

$$h(r_{ij}, r_{ik}, \theta_{jik}) = \lambda \exp[\gamma(r_{ij} - a)^{-1} + \gamma(r_{ik} - a)^{-1}] (\cos \theta_{jik} + \frac{1}{3})^2, \quad (2.7)$$

where θ_{jik} is the angle between \mathbf{r}_j and \mathbf{r}_k subtended at vertex i . The ideal tetrahedral geometry is favored by the angle $\theta_t = \cos^{-1}(-1/3)$ in Eq. (2.7).

SW potential is widely used in MD simulation as it can accurately describe elastic properties and thermal expansion coefficients [76–79]. The parameter set of SW potential for Si was devised by Stillinger and Weber in Ref. [76] as the following

$$\begin{aligned} \epsilon &= 50 \text{ kcal/mol}, \\ \sigma &= 0.20951 \text{ nm}, \\ A &= 7.049556277, \\ B &= 0.6022245584, \\ p &= 4, q = 0, a = 1.80, \\ \lambda &= 21.0, \gamma = 1.20. \end{aligned} \quad (2.8)$$

The parameter set of SW potential for Ge was later developed by Ding *et al.* in Ref. [80] as the following

$$\begin{aligned} \epsilon &= 1.93 \text{ eV}, \\ \sigma &= 0.2181 \text{ nm}, \\ A &= 7.049556277, \\ B &= 0.6022245584, \\ p &= 4, q = 0, a = 1.80, \\ \lambda &= 31.0, \gamma = 1.20. \end{aligned} \quad (2.9)$$

These two parameter sets are different in parameter ϵ , σ , and λ . To model the Si-Ge bond, the length unit σ_{Si-Ge} is taken as the arithmetic average of individual

Si and Ge parameters, while the energy unit ϵ_{Si-Ge} and λ_{Si-Ge} are taken as the geometric average of individual Si and Ge parameters [81].

2.3 Velocity Verlet Algorithm

Velocity Verlet algorithm is one of the most popular numerical integration algorithms. In mathematics, a numerical integration scheme is a symplectic integrator if it conserves the two-form $\sum_j dp_j \wedge dq_j$ [82], where p_j and q_j denote the momentum and position of particle j , respectively. Some of the widely used integration algorithms, such as Euler and Runge-Kutta scheme, are not symplectic integrators. Velocity Verlet is mathematically a symplectic algorithm and thus is ideal to handle the Hamiltonian mechanics where the total energy is conserved with respect to time. This symplectic nature is extremely important in MD simulation as the simulation is usually performed for a very long time in order to get a good sampling of the phase space. The detailed derivation and error analysis of this algorithm can be found in many textbooks for computational science [83]. Thus, only key steps of this algorithm are listed here.

Suppose $\mathbf{r}(t)$, $\mathbf{v}(t)$, and $\mathbf{a}(t)$ is the position, velocity, and acceleration at time t , respectively. $V(\mathbf{r}(t))$ is the potential energy, m is the mass, and Δt is the time step. To update these variables at time $t + \Delta t$, the Velocity Verlet algorithm is

carried out in the following steps

$$\mathbf{r}(t + \Delta t) = \mathbf{r}(t) + \mathbf{v}(t)\Delta t + (1/2)\mathbf{a}(t)\Delta t^2, \quad (2.10)$$

$$\mathbf{v}(t + \Delta t/2) = \mathbf{v}(t) + (1/2)\mathbf{a}(t)\Delta t, \quad (2.11)$$

$$\mathbf{a}(t + \Delta t) = -(1/m)\nabla V(\mathbf{r}(t + \Delta t)), \quad (2.12)$$

$$\mathbf{v}(t + \Delta t) = \mathbf{v}(t + \Delta t/2) + (1/2)\mathbf{a}(t + \Delta t)\Delta t. \quad (2.13)$$

2.4 Non-equilibrium Molecular Dynamics

2.4.1 Background

There are two different approaches in non-equilibrium molecular dynamics (NEMD) simulations. One approach is to set up a temperature gradient across the system by fixing the two ends of the system at different temperature, and then calculate the resultant heat flux running through the system in the non-equilibrium steady state. In this approach, temperature of the two ends is fixed by putting the two ends in contact with heat bath, which induces additional force to the particles in it and the dynamics of the whole system is governed by the Hamiltonian. This approach is in analogy to real experimental measurement, and is also known as direction method. More importantly, it is consistent with the actual physical picture of heat conduction: the temperature gradient across the system is the “*cause*” of heat conduction, and consequently the heat flux running through the system is the “*effect*”. Moreover, the way to fix temperature with heat bath, such as Langevin heat bath, is based on Brownian dynamics which is the well known microscopic picture of the motions of the particles, and is also consistent with the fluctuation-dissipation theory [84]. The deficiency of this approach is

that it usually takes a long time simulation to obtain the constant heat flux in the non-equilibrium steady state.

The other approach is to reverse the usual cause and effect picture. The “effect”, *heat flux*, is now imposed to the system, and the “cause”, *temperature gradient*, is obtained from simulations. In this approach, the constant heat flux is artificially introduced to the two ends of the system, by either exchanging the velocity of the particles at two ends [85] or scaling the velocity of the particles at two ends [86]. This approach has the advantage that the slowly converging quantity *heat flux* is now known exactly and needs not to be calculated. As a result, the total simulation time can be reduced as only the relatively fast converging quantity *temperature* needs to be calculated in the simulation. However, the deficiency of this approach is obvious: it is not consistent with the actual physical picture of heat conduction. Moreover, the heat flux is artificially introduced and there is no fundamental theoretical basis for it. As a result, the dynamics of the whole system is not completely governed by the Hamiltonian.

Therefore, the first approach in NEMD simulation is employed throughout this thesis. Fig. 2.1 shows the schematic picture for NEMD simulation of silicon nanowires (SiNWs). Here we set longitudinal direction along x axis, and atoms in the same layers means they have the same x coordinate. Boundary condition (BC) is imposed on the boundary layers (indicated by arrows in Fig. 2.1) at two ends of SiNWs, either fixed or free BC. Next to the boundary layers, several layers of SiNWs are put in contact with the heat bath (inside the rectangular box in Fig. 2.1), which can reproduce the canonical ensemble (i.e., constant temperature). To simulate the heat source and sink in real experiment, two heat bathes at high temperature T_H and low temperature T_L are used. The local temperature is defined

as

$$T = \left\langle \sum_{i=1}^N m_i \mathbf{v}_i \cdot \mathbf{v}_i \right\rangle / (3Nk_B), \quad (2.14)$$

where N is the total number of atoms in the same layer, k_B is Boltzmann's constant, m_i and \mathbf{v}_i is the mass and velocity (vector form) of atom i , respectively, and the angular bracket denotes the ensemble average.

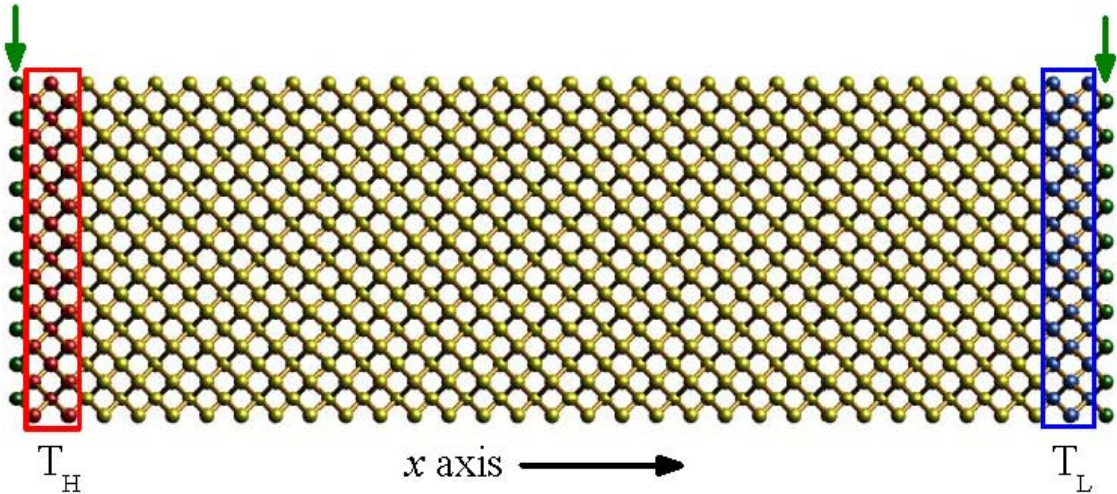


Figure 2.1: **Schematic picture for NEMD simulation of SiNWs.** The longitudinal direction is set along x axis. The green arrows point the boundary atoms. Atoms in red and blue boxes are put in contact with the heat bath at high temperature T_H and low temperature T_L , respectively.

NEMD simulation is usually performed long enough to allow the system to reach the non-equilibrium steady state where the temperature gradient is well established (Fig. 2.2) and the heat current going through the system is time independent. Thermal conductivity is calculated according to Fourier's law of heat conduction

$$\kappa = -J_L / \nabla T, \quad (2.15)$$

where ∇T is the temperature gradient that can be calculated from the linear fit line of temperature profile (Fig. 2.2), and J_L is the heat current along the longitudinal direction defined as the energy transported along the nanowire in unit time through the unit cross sectional area [87].

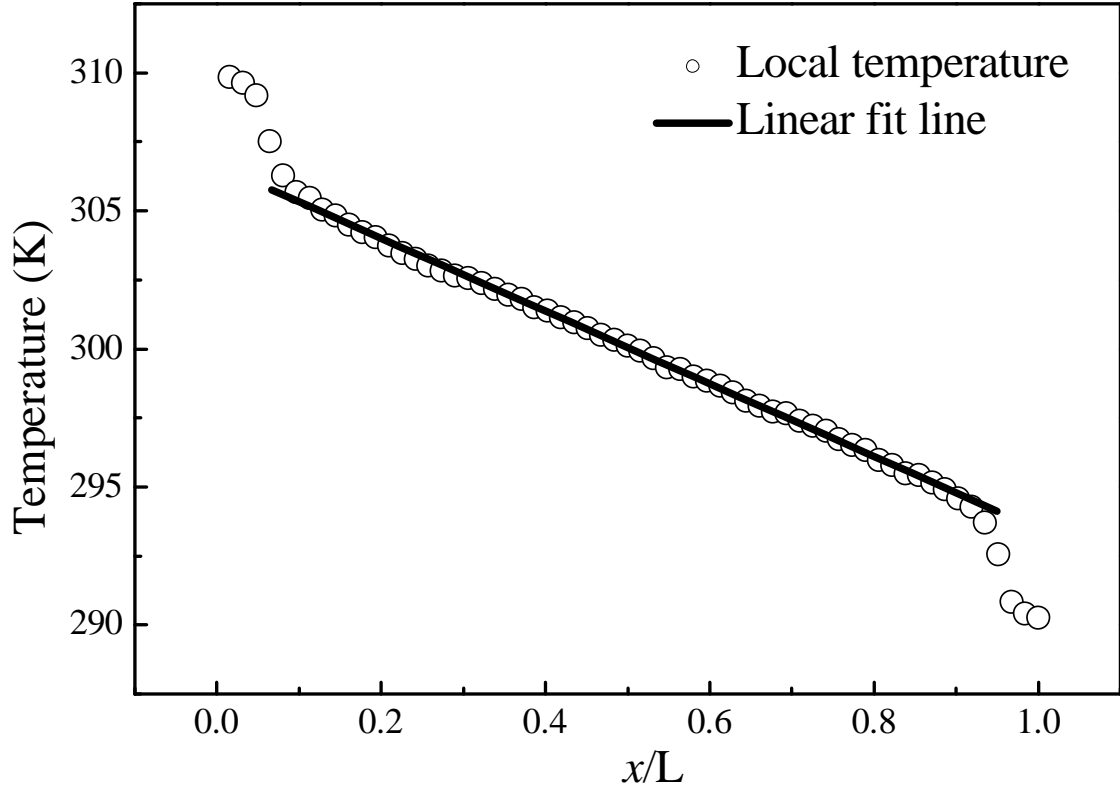


Figure 2.2: **Temperature profile of SiNWs in NEMD simulation.** The longitudinal direction is set along x axis. The hollow circle plots the local temperature of each layer along the longitudinal direction, and the solid line is the linear fit line of the local temperature.

2.4.2 Effect of Heat Bath

In NEMD simulations, heat bath is used to set up temperature gradient in the system. There are two representative approaches used to control the temperature: Nosé-Hoover (NH) heat bath [88, 89] which is an example of deterministic heat bath, and Langevin heat bath [90] which is an example of stochastic heat bath. The evolution of the particles in thermal contact with NH heat bath can be ruled by the equation as:

$$\frac{d\mathbf{q}_i}{dt} = \frac{\partial H}{\partial \mathbf{p}_i}, \quad \frac{d\mathbf{p}_i}{dt} = -\frac{\partial H}{\partial \mathbf{q}_i} - \zeta \mathbf{p}_i, \quad (2.16)$$

where H is the Hamiltonian of the system, \mathbf{p}_i and \mathbf{q}_i are the momentum and coordinate of particle i , respectively, and ζ is an auxiliary variable modeling the microscopic action of the heat bath. The dynamics of ζ is governed by the following equation:

$$\frac{d\zeta}{dt} = \frac{1}{\tau^2} \left(\frac{\sum_{i \in S} \mathbf{p}_i \cdot \mathbf{p}_i}{3mk_B T N} - 1 \right), \quad (2.17)$$

where T and τ are the aimed temperature and response time of heat bath, respectively, m is the mass of the particle, and N is the total number of particles that are in contact with heat bath.

With Langevin heat bath, the equation of motion can be described as

$$\frac{d\mathbf{p}_i}{dt} = -\frac{\partial H}{\partial \mathbf{q}_i} + \xi - \lambda \mathbf{p}_i, \quad (2.18)$$

where λ is the dissipation rate, and ξ is the random force that follows Wiener process with zero mean and variance $2m\lambda k_B T$ according to the fluctuation-dissipation theorem.

In both schemes of heat bathes, there is a free parameter, namely τ in NH heat bath and λ in Langevin heat bath, which controls the strength of the noise

in heat bath. In this section, we take SiNWs as an example to study the impact of heat bath on the calculated thermal properties of homogeneous materials. Moreover, we extend our study to heterogeneous materials, such as Si/Ge NW junctions, in which a rectification of heat current in different directions can be studied. Velocity Verlet algorithm (Chap. 2.3) is used to numerically integrate Newton's equation of motion. To derive the force term, SW potential (Chap. 2.2) is used. The temperature of hot and cold heat bathes are set as 310 K and 290 K, respectively. Simulations are performed long enough to allow the system to reach a non-equilibrium steady state where the heat current going through the system is time independent. All results given in this section are obtained by averaging about 5×10^7 time steps, and each time step is set as 0.8 fs ($1 \text{ fs} = 10^{-15} \text{ s}$). Free boundary condition is used to atoms on the outer surface of the nanowires, and fixed boundary condition is imposed on the boundary layers at two ends of the nanowires. Thermal conductivity is calculated according to Eq. (2.15).

We first study thermal conductivity of [100] SiNWs with a cross section of 3×3 unit cells (lattice constant is 0.543 nm, 8 atoms in each unit cell) and 10 unit cells in the longitudinal direction. It has been reported that due to the lack of stability of the nanowire surfaces, it can lead to scattered computed results [91]. In our calculations, at room temperature and with the small temperature difference between the two ends, the surface structure is stable, and the different heat bath and the difference in temperature profile have no impact on the stability of nanowire surfaces.

In Fig. 2.3 we show the effect of the number of heat bath layers (NL) on the thermal properties of SiNWs. Here $\tau=0.1$ and $\lambda=10$ are used in NH heat bath and Langevin heat bath, respectively. A linear temperature gradient is always observed

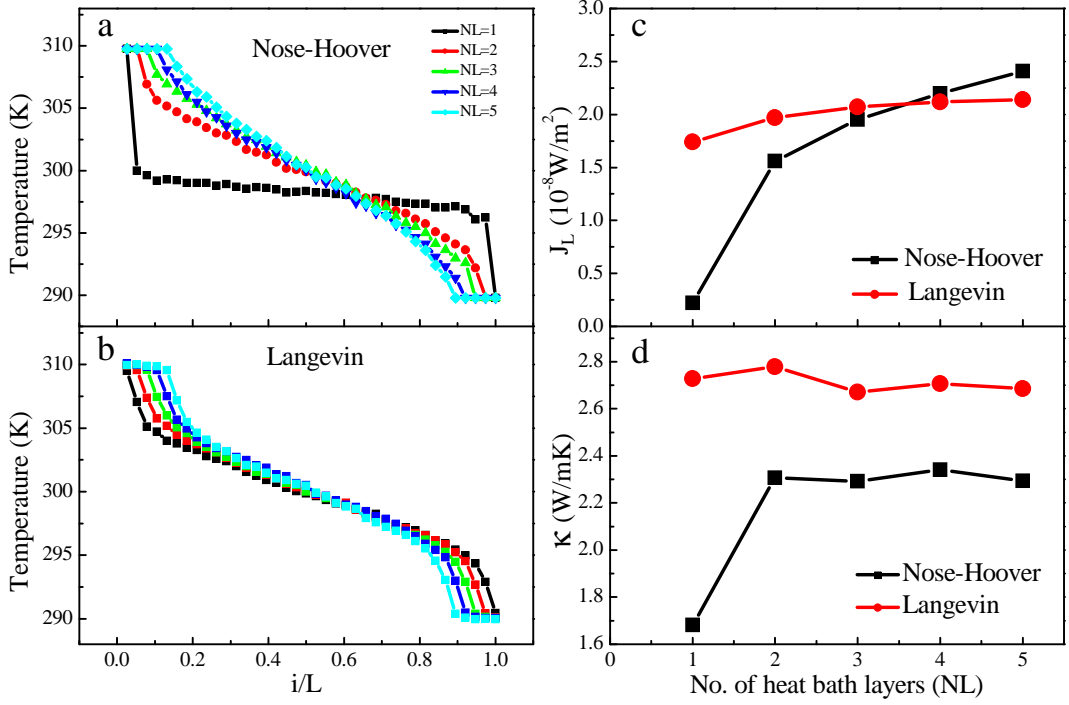


Figure 2.3: **Impacts of the number of heat bath layers (NL) on thermal properties of SiNWs.** a Temperature profile with different NL of Nosé-Hoover heat bath. b Temperature profile with different NL of Langevin heat bath. c Heat current along the longitudinal direction J_L versus NL. d Thermal conductivity κ versus NL.

in the interior, and the main difference in temperature profile between different heat bath types is the temperature jump between the heat bath layers and interior layers. With only one layer of NH heat bath, there exists a large temperature jump (TJ) between the heat bath layer and its neighboring layer (shown in Fig. 2.3a), while the temperature jump is much smaller with one layer of Langevin heat bath (shown in Fig. 2.3b).

This temperature jump can be explained by localized edge mode (LEM) of phonons. With fixed boundary condition, there exists edge mode localized at the

neighboring layer next to the fixed boundary [92]. This edge mode is actually a quite generic feature of materials in thermal transport and essentially originated from the specific geometrical configuration of the edge region [93], very similar to the electronic and/or spin edge states [94–96]. It should be emphasized that localization effect is a quite generic consequence of the broken of spatial periodicity due to the imposed boundary condition in finite system. Therefore, LEM also exists with other boundary conditions in finite system (e.g., free or periodic) [92].

Due to the localization, LEM contributes little to heat transport. If heat bath is applied to this region, LEM will be excited and localized at this region, while other modes can propagate and contribute to the heat transport. We can see from Eq. (2.20) and (2.17) that in order to maintain a constant temperature, the mechanism of NH heat bath is to introduce a viscosity force which is proportional to the velocity, and the proportionality is determined from the velocities of all the particles. Due to this deterministic characteristic of NH heat bath, once LEM is excited, it will accumulate at the heat bath layer over time, because LEMs have a larger amplitude than other modes and account for a large percentage of the total modes [92]. As a result, although the heat bath can maintain a constant temperature, the major contribution comes from LEM which cannot be utilized in heat transport. Therefore, there exists a large TJ when there is only one layer of NH heat bath. With the number of heat bath layer increasing, TJ will be reduced as shown in Fig. 2.3a. This is because of the exponential decay feature of LEM over distance. With multiple layers of heat bath which are away from the localized region, other modes can be excited and dominate in heat transport. Therefore, the localized effect on the thermal transport is suppressed. The reduction in TJ leads to large increase in J_L from NL=1 to NL=2 as shown in Fig. 2.3c. Further

increase of heat bath layers cannot eventually eliminate TJ. The small retained TJ is due to the thermal interface resistance between heat bath and rest parts.

With Langevin heat bath, the accumulation effect of LEM can be removed automatically, resulting in a small TJ even with one layer of heat bath as shown in Fig. 2.3b. In addition, when NL increases, J_L converges to a constant value much faster than the case with NH heat bath. The reason is that with Langevin heat bath, each mode can be excited randomly at every time step due to the stochastic characteristic of Langevin heat bath, which can effectively suppress the accumulation of LEM over time.

The large TJ induced by LEM can be further understood by looking at the autocorrelation function of velocity. Fig. 2.4 plots the normalized autocorrelation function of velocity of atoms in the middle of NWs with the same parameters used in Fig. 2.3a and 2.3b. With one layer of NH heat bath, since it mainly utilizes LEM to maintain the constant temperature, there exists obviously nonvanishing correlation in the long-time region. This artificial correlation is the direct evidence of the existence and accumulation effect of LEM mentioned above, which leads to the large TJ. With multiple layers of NH, the artificial correlation vanishes because all the modes can contribute to the thermal transport, thus a much smaller TJ. Moreover, due to the stochastic characteristic of Langevin heat bath, the artificial correlation does not exist, regardless of the number of heat bath layers applied.

It is worth mentioning that we have also checked the temperature jump in other popularly used deterministic heat bath, such as the Berendsen heat bath [97]. It is a velocity-scaling type heat bath, with the scaling factor [97]:

$$\gamma = \left[1 + \frac{\Delta t}{\tau_T} \left(\frac{T_0}{T} - 1 \right) \right]^{1/2}, \quad (2.19)$$

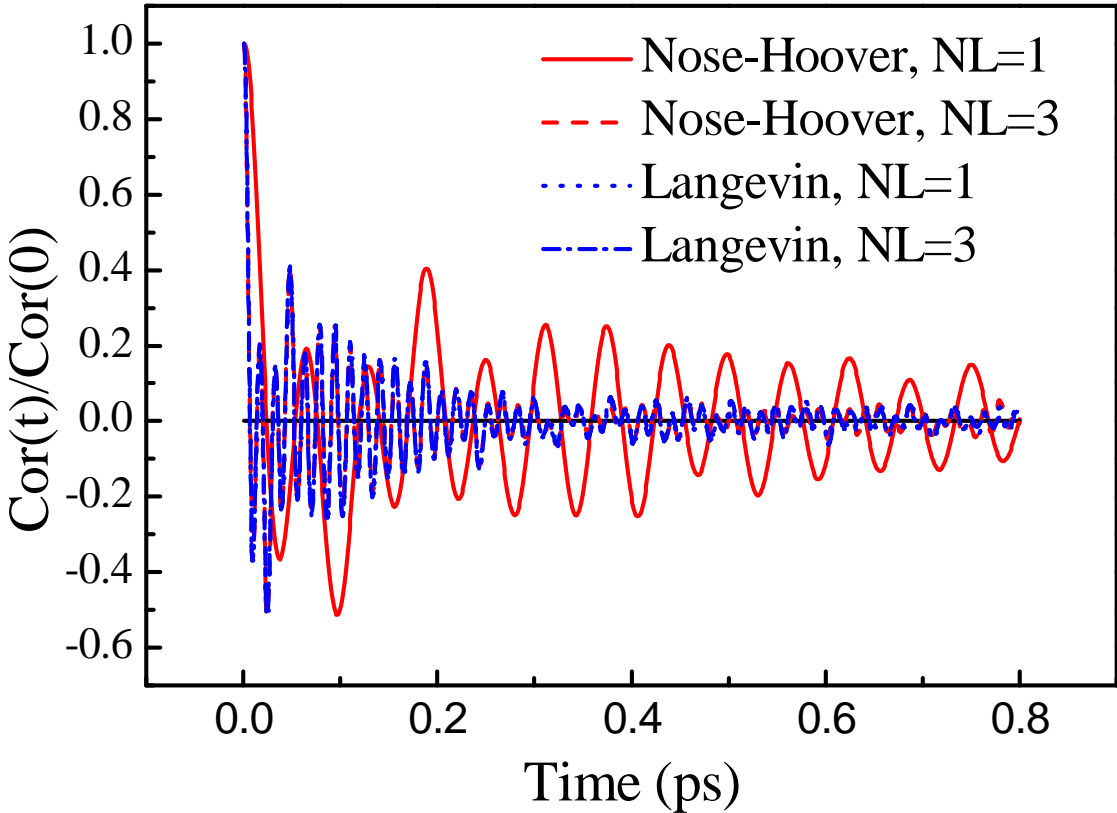


Figure 2.4: **Normalized autocorrelation function of velocity in different heat baths.** Except for the solid line, the other three lines almost overlap with each other.

where Δt is the time step, τ_T is the relaxation time, T_0 and T are the aimed temperature and instantaneous temperature, respectively. The relaxation time τ_T should be properly chosen to avoid unrealistically low temperature fluctuations with small τ_T , and the inactive sampling with large τ_T (e.g., $\tau_T \rightarrow \infty$) [98]. Based on such considerations, we set $\tau_T = \Delta t \times 10^4$ (8 ps) in our study. As shown in Fig. 2.5, with Berendsen heat bath, the NW fails to reach the aimed temperature (310 K and 290 K) at two ends. More seriously, large temperature jump persists

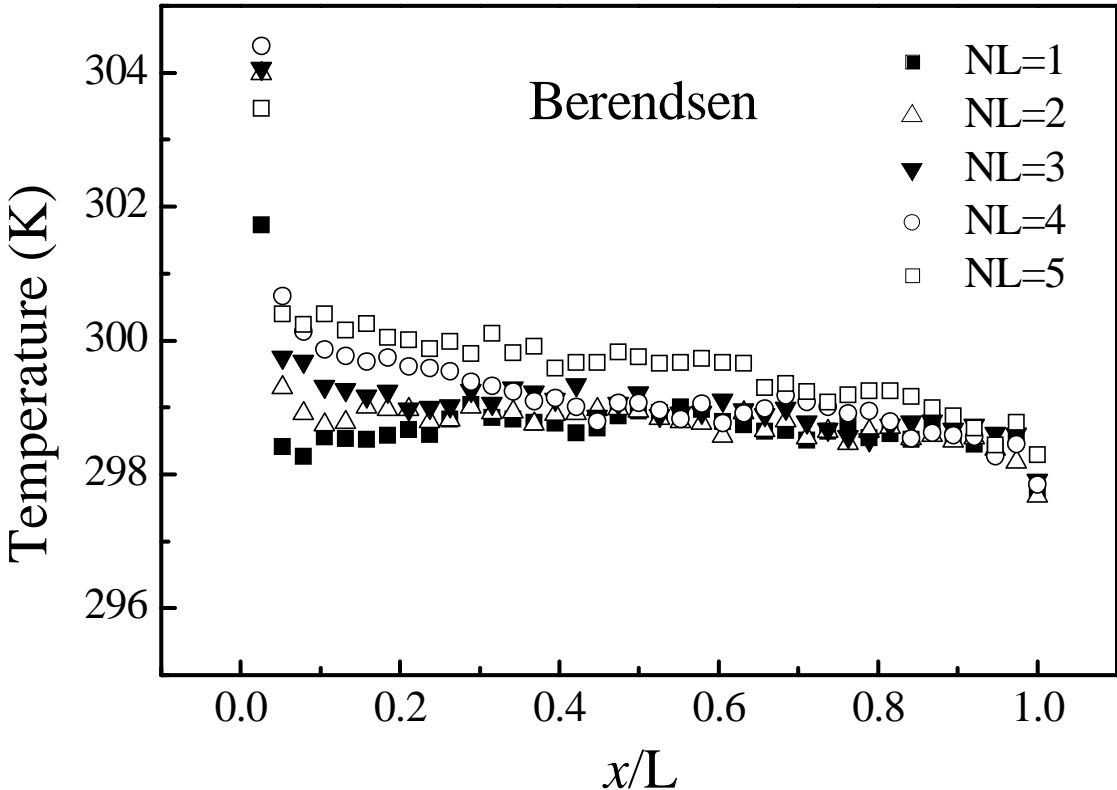


Figure 2.5: Temperature profile with different number of layers (NL) of Berendsen heat bath.

regardless of the number of heat bath layers applied. This even poorer performance of Berendsen heat bath is an expected consequence of its inability to reproduce canonical ensemble, because of the artificial velocity-scaling scheme [98], which has been reported to cause artifacts in various studies [99–102]. Therefore, in the following part, we mainly concentrate on the parameter effect of both NH and Langevin heat bath.

From the calculated heat current and temperature gradient, we can obtain the thermal conductivity. From Fig. 2.3d, it is obvious that with Langevin heat bath,

one can obtain a consistent result regardless of the number of heat bath layers applied. However, due to the existence of LEM and the deterministic nature of NH heat bath, multiple heat bath layers are required in order to get a consistent result. In both NH and Langevin heat bath, the calculated thermal conductivity converges to a constant when $NL \geq 3$. However, the converged values of thermal conductivity are different in these two heat bathes. Moreover, there is a free heat bath parameter (τ/λ) which effectively controls the strength of noise (response time of NH heat bath/dissipate rate of Langevin heat bath). Since we fix the heat bath parameter in the first part of this study, to what extent can the choice of free parameter in different heat bath influence the calculated thermal properties are yet not clear. In the following part, we fix the heat bath temperature at 310 K and 290 K, and tune the heat bath parameters to study their impacts on heat current, temperature profile and thermal conductivity.

Next we set $NL=3$ for both NH and Langevin heat bath. In Fig. 2.6 we plot the impacts of heat bath parameter on the calculated thermal properties of SiNWs. For NH heat bath, τ cannot be too small (e.g., $\tau=0.01$ in Fig. 2.6a) since it produces a wrong temperature profile in this case, although the heat bath still can reach the aimed temperature and a temperature gradient can be established in the middle region. With the increase of τ from 0.01, the temperature gradient in the middle region is almost the same, but the mean temperature decreases until $\tau=0.2$. This results in a decrease in heat current when $\tau < 0.2$. Particularly when $\tau=0.04$, TJ at the left boundary is nearly zero, while TJ at the right boundary is about 5 K. This should be a numerical artifact because TJ has its physical origin from the thermal interface resistance between heat bath and the middle region, thus cannot be eliminated by tuning parameter. With further increase

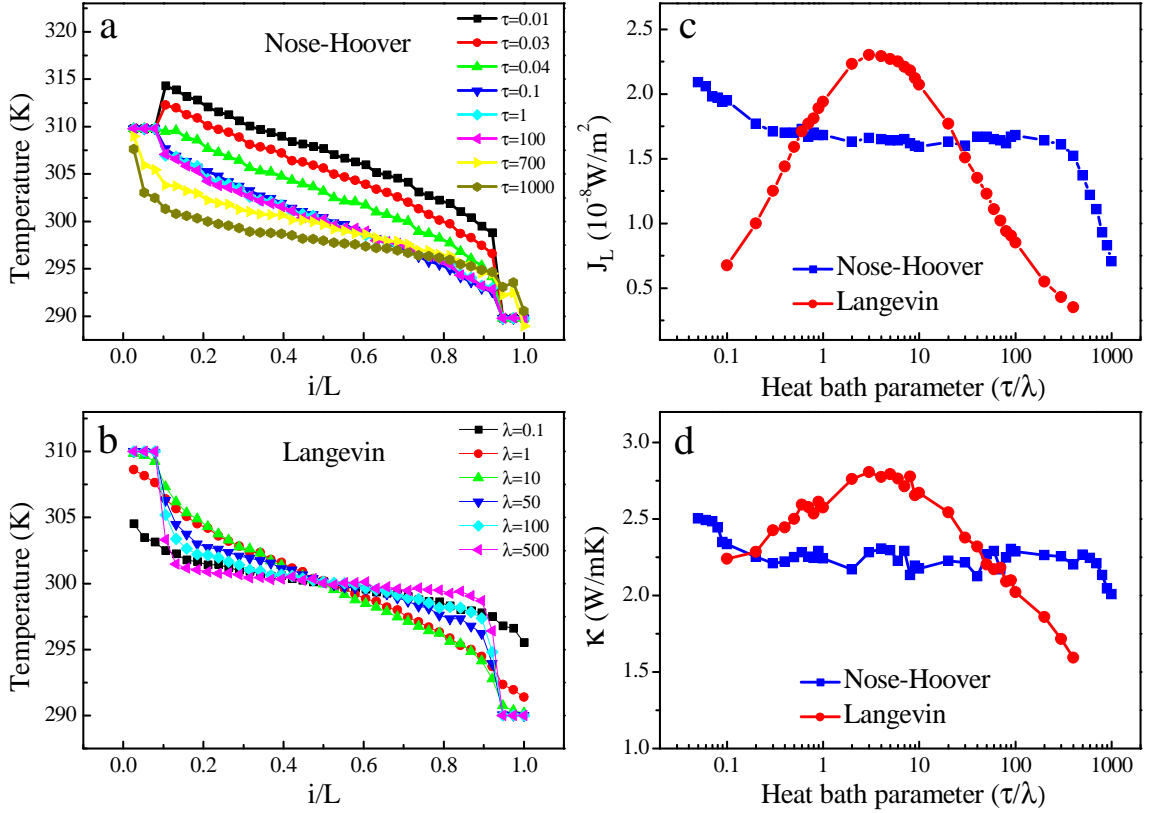


Figure 2.6: **Impacts of heat bath parameter on thermal properties of SiNWs.** The nanowire has a fixed cross section of 3×3 unit cells. In the longitudinal direction, it has a fixed length of 10 unit cells with 3 layers of heat bath at each end.

- a Temperature profile with parameter τ of Nosé-Hoover heat bath.
- b Temperature profile with parameter λ of Langevin heat bath.
- c Heat current J_L versus τ/λ for Nosé-Hoover/Langevin heat bath.
- d Thermal conductivity κ versus τ/λ for Nosé-Hoover/Langevin heat bath.

Here $0.05 \leq \tau \leq 1000$, and $0.1 \leq \lambda \leq 400$.

of τ ($0.2 < \tau < 300$), temperature profile becomes correct and stable: both J_L and temperature gradient become insensitive to τ , thus the calculated thermal conductivity in Fig. 2.6d is almost a constant with small fluctuation. Next, when $\tau > 300$, temperature gradient becomes smaller and J_L decreases quickly. This is because in the large τ range, the distribution of ζ values becomes a δ -function [90]. As a result, it would require longer simulation times in order to ensure the decay of correlations. This causes the heat bath cannot reach the aimed temperature due to the limited simulation time, also a smaller temperature gradient. Therefore, from the consideration of a practical computational time, one should not choose too large τ .

For Langevin heat bath, in the weak coupling limit $\lambda \rightarrow 0$ (e.g., $\lambda = 0.1$ in Fig. 2.6b), the heat bath cannot reach the aimed temperature. However, in the strong coupling limit (e.g., $\lambda = 500$ in Fig. 2.6b), although the heat bathes can reach the aimed temperature, large TJ is observed at the boundary. In both cases, small temperature gradient is generated, which induces a small heat current. In the middle range of λ , a temperature profile with correct heat bath temperature and small TJ can be established. This causes J_L and thermal conductivity first increase then decrease with the increase of λ as shown in Fig. 2.6c and 2.6d. All these are consistent with the results obtained from Fermi-Pasta-Ulam (FPU) chain in Ref. [90].

The parameter λ in Langevin heat bath has the physical meaning of dissipate rate, which characterizes the damping coefficient of the surrounding environment in the heat bath. Therefore, the variation of λ is essentially changing the surrounding environment in the heat bath, which leads to the variation of contact resistance at the interface between the heat bath and central segment. This is illustrated

by the variation of temperature gradient and heat flux with respect to λ shown in Fig. 2.6. From experimental point of view, one should choose a material with high thermal conductivity as the contact so that a notable heat current can be detected. Similarly, the choice of parameter λ should be selected in order to: (a) maximize the heat current so that obvious temperature gradient can be established to minimize the error in the calculation of temperature gradient; (b) the heat bath region should reach the aimed temperature. Based on these considerations, we suggest parameter region $2 \leq \lambda \leq 10$ for Langevin heat bath and $1 \leq \tau \leq 100$ for NH heat bath.

Heterogeneous materials such as carbon nanotube based [87] and graphene based [103] nanojunctions are promising candidates for thermal rectifier application. In these systems, it is problematic to define thermal conductivity according to Fourier's law, due to the large temperature jump at the interface of two different materials. Instead, because of the asymmetry of the heterogeneous materials, people are more interested in the rectification effect of heat current in such materials [104], namely the difference between the heat current in different directions. In the following part, we extend our study to heterogeneous materials and discuss the effect of heat bath parameter on the heat current rectification.

We use Si/Ge nanojunction as an example. It has a fixed cross section of 3×3 unit cells, 5 unit cells of Si and 5 unit cells of Ge in the longitudinal direction. Three layers of heat bath are applied at each end, with heat bath temperature set at 310 K and 290 K. Here we define J_+ (J_-) to be the heat current of non-equilibrium steady state when Si (Ge) end is attached to the high temperature heat bath. We define the rectification ratio to be:

$$RE = (J_+ - J_-)/J_- \quad (2.20)$$

Figures 2.7a and 2.7b show the dependence of heat current on heat bath parameters. It has been checked that temperature profiles are all correct with these parameters for both NH and Langevin heat bath. With NH heat bath, J_+ and J_- have the distinct dependence on τ . In the small τ limit, J_+ is much larger than J_- . With the increase of τ , J_+ drops rapidly and finally converges to a small value, while J_- first increases, then decreases, and finally converges to a value which is slightly larger than J_+ . As a result, there exists a large value of RE in the small τ limit as shown in Fig. 2.7c. Moreover, RE changes from positive to negative when $0.05 \leq \tau \leq 100$. Thus NH heat bath fails to give a consistent result.

On the contrary, with Langevin heat bath, Fig. 2.7b shows the same dependence on λ for both J_+ and J_- , and there is only a small difference between them. This results a small value of RE (5% by maximum) as shown in Fig. 2.7c for Langevin heat bath. More importantly, Langevin heat bath can produce a consistent result ($RE < 0$) that J_- is always larger than J_+ , regardless of the heat bath parameter λ . Si-Ge nanowire is a mass graded nanojunction. The results calculated with Langevin heat bath and NH heat bath with large τ ($\tau > 1$) suggest that the heat current runs preferentially along the direction of decreasing mass. This conclusion is consistent with experimental result by Chang *et al.* [105]. In Ref. [105], they demonstrated the thermal rectification effect in carbon and boron nitride nanotubes that were inhomogeneously mass-loaded with heavy molecules. A larger heat flow was observed when heavy-mass end is at higher temperature, and maximum thermal rectification is only 7%. Moreover, Landry and McGaughey [106] theoretically studied thermal boundary resistance of Si/Ge interface at 500 K and no thermal rectification was observed in their study. Therefore, the significant rectification predicted by NH heat bath with small τ might be artificial.

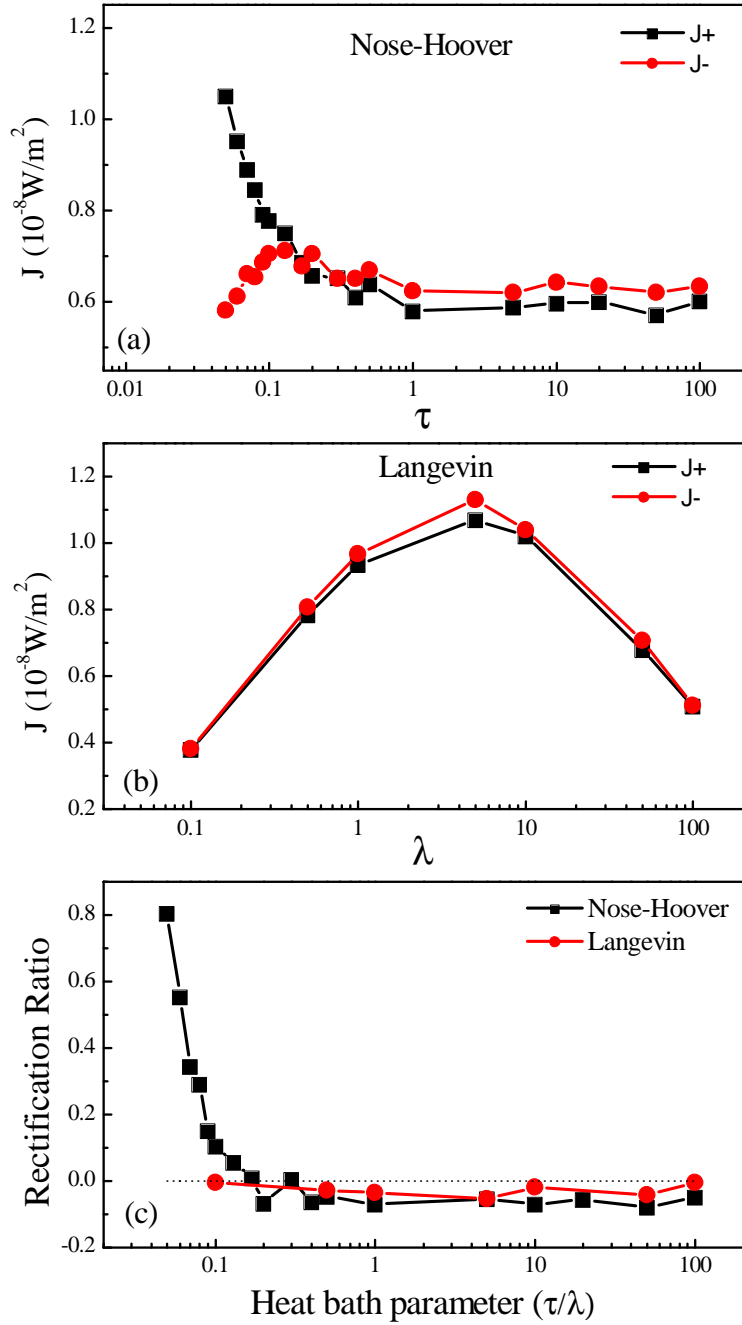


Figure 2.7: J_{\pm} in Si/Ge nanojunctions versus heat bath parameters. The square and circle denote the results for Nosé-Hoover (τ) and Langevin (λ) heat bath, respectively. a J_{\pm} versus parameter τ of Nosé-Hoover heat bath. b J_{\pm} versus parameter λ of Langevin heat bath. c Rectification ratio versus heat bath parameter.

2.4.3 Summary

In conclusion, we have studied the impacts of heat bath on calculated thermal properties of nanostructures in non-equilibrium molecular dynamics simulations. Due to the existence of localized edge modes and their accumulation effect induced by the deterministic characteristic of Nosé-Hoover heat bath, multiple layers of Nosé-Hoover heat bath are required in order to reduce the temperature jump at the boundary. Even with one layer of Langevin heat bath, it can eliminate the accumulation of localized edge modes due to its stochastic excitation of all modes, giving rise to a small temperature jump at the boundary. In addition, in order to obtain the correct temperature profile, intermediate values of heat bath parameter, $1 \leq \tau \leq 100$ for Nosé-Hoover heat bath and $2 \leq \lambda \leq 10$ for Langevin heat bath, are recommended. Moreover, for the study of heat current rectification in heterogeneous materials, Langevin heat bath is recommended because it can produce consistent results with experiment, regardless of the heat bath parameter.

2.5 Equilibrium Molecular Dynamics

2.5.1 Green-Kubo Formula

Equilibrium molecular dynamics (EMD) simulation is based on the Green-kubo formula (GKF) derived from the fluctuation-dissipation theorem [84] and linear response theory, which relates thermal conductivity with heat current autocorrelation function (HCACF) [107–109]. In GKF, the entire dynamics of the systems is expressed through the time correlation function in thermal equilibrium, which invokes little assumption about the physical property of the material. Thus,

EMD simulation has been applied to study thermal properties of various materials [110–114].

Several derivations of GKF exist in literature [115]. Here we follow the derivation by Kubo *et al.* in Ref. [116], with emphasis on some essential steps. There is also a Kubo formula for electrons [108], which relates electrical conductivity to the electrical current autocorrelation function. For the electrical case, there is a mechanical disturbance term [116] in the Hamiltonian, which describes the energy perturbation due to the applied external electrical field, and the derivation of electrical Kubo formula follows the standard perturbation theory. For the thermal case, however, the derivation of GKF is less straightforward but relies on the statistical hypothesis of local thermal equilibrium, which can be described by the local space-dependent temperature $T(\mathbf{r}) = [k_B\beta(\mathbf{r})]^{-1}$.

Consider a system with Hamiltonian H and volume V at temperature $T(\mathbf{r})$ subjected to a small thermal disturbance $\delta T(\mathbf{r})$. The local thermal equilibrium holds and can be described by the local equilibrium density matrix

$$\rho = \exp[-\int d^3\mathbf{r} \beta(\mathbf{r})h(\mathbf{r})]/Z, \quad (2.21)$$

where Z is the partition function, and $h(\mathbf{r})$ is the Hamiltonian density operator related to the Hamiltonian as $H = \int d^3\mathbf{r} h(\mathbf{r})$. Similarly, we define the heat current density operator $\mathbf{s}(\mathbf{r})$ as

$$\mathbf{S} = \int d^3\mathbf{r} \mathbf{s}(\mathbf{r}), \quad (2.22)$$

where \mathbf{S} is the total heat current operator. Due to the energy conservation, these two density operators are related through

$$\frac{\partial h(\mathbf{r})}{\partial t} + \nabla \cdot \mathbf{s}(\mathbf{r}) = 0. \quad (2.23)$$

Without $\delta T(\mathbf{r})$, the system is in thermal equilibrium so that $T(\mathbf{r}) = T_0 = [k_B\beta_0]^{-1}$ is a constant, and there is no net heat current ($\mathbf{J} = \text{Tr}[\rho_0 \mathbf{S}] = 0$). After applying the small thermal disturbance, the density matrix becomes

$$\rho = \exp[-\beta(H + H')]/Z, \quad (2.24)$$

where H' is the small perturbation to the Hamiltonian caused by the thermal disturbance. There is a fundamental equality in quantum mechanics for any two operators \hat{a} and \hat{b} such that [116]

$$e^{\beta(\hat{a}+\hat{b})} = e^{\beta\hat{a}}(1 + \int_0^\beta d\lambda e^{-\lambda\hat{a}}\hat{b}e^{\lambda(\hat{a}+\hat{b})}), \quad (2.25)$$

where λ is a phase space variable. With this equality, the numerator of density matrix in Eq. (2.24) can be approximated to the first order as

$$e^{-\beta(H+H')} = e^{-\beta H}(1 - \int_0^\beta d\lambda e^{\lambda H} H' e^{-\lambda H}). \quad (2.26)$$

The small perturbation to the Hamiltonian can be expressed as

$$\begin{aligned} H' &= \frac{1}{T} \int d^3\mathbf{r} \delta T(\mathbf{r}) h(\mathbf{r}) \\ &= -\frac{1}{T} \int dt \int d^3\mathbf{r} \delta T(\mathbf{r}) \nabla \cdot \mathbf{s}(\mathbf{r}) \\ &= \frac{1}{T} \int dt \int d^3\mathbf{r} \nabla T(\mathbf{r}) \cdot \mathbf{s}(\mathbf{r}) \\ &= \frac{1}{T} \int dt \nabla T \cdot \mathbf{S}, \end{aligned} \quad (2.27)$$

where we have used the integrated form of Eq. (2.23), performed an integration by part, and assumed the temperature gradient to be a spatial constant.

With the small thermal disturbance, the net heat current becomes

$$\mathbf{J} = \text{Tr}[\rho \mathbf{S}] = -\frac{1}{TV} \int_0^\infty dt \int_0^\beta d\lambda \langle e^{\lambda H} (\nabla T \cdot \mathbf{S}(0)) e^{-\lambda H} \mathbf{S}(t) \rangle, \quad (2.28)$$

where the angular bracket denotes the ensemble average. According to the Fourier's law

$$\kappa_{\mu\nu} = -\frac{J_\mu}{\nabla_\nu T}, \quad (2.29)$$

where μ and ν are two Cartesian indices, thermal conductivity can be written in the tensor form as

$$\begin{aligned} \kappa_{\mu\nu} &= \lim_{\tau \rightarrow \infty} \lim_{V \rightarrow \infty} \frac{1}{TV} \int_0^\tau dt \int_0^\beta d\lambda \langle e^{\lambda H} S_\nu(t') e^{-\lambda H} S_\mu(t'') \rangle \\ &= \lim_{\tau \rightarrow \infty} \lim_{V \rightarrow \infty} \frac{1}{TV} \int_0^\tau dt \int_0^\beta d\lambda \langle e^{\lambda H} S_\nu(0) e^{-\lambda H} S_\mu(t) \rangle \\ &= \lim_{\tau \rightarrow \infty} \lim_{V \rightarrow \infty} \frac{1}{TV} \int_0^\tau dt \int_0^\beta d\lambda \langle S_\nu(-i\hbar\lambda) S_\mu(t) \rangle, \end{aligned} \quad (2.30)$$

where we have assumed that in the steady state HCACF in Eq. (2.30) only depends on the time difference ($t = t'' - t'$), and used the time dependence of operator in Heisenberg picture: $\hat{a}(t) = e^{i\frac{H}{\hbar}t} \hat{a}(0) e^{-i\frac{H}{\hbar}t}$. Notice that the order of the limits in Eq. (2.30) is important: the volume limit $V \rightarrow \infty$ must be taken first, followed by the time limit $\tau \rightarrow \infty$ [117]. For the sake of simplicity, we will omit the limits in Eq. (2.30) and put the time limit to infinity in the following discussions.

In the classical limit $\hbar \rightarrow 0$, Eq. (2.30) can be further simplified to

$$\begin{aligned} \kappa_{\mu\nu} &= \frac{1}{TV} \int_0^\infty dt \int_0^\beta d\lambda \langle S_\nu(0) S_\mu(t) \rangle \\ &= \frac{1}{k_B T^2 V} \int_0^\infty dt \langle S_\nu(0) S_\mu(t) \rangle. \end{aligned} \quad (2.31)$$

For bulk materials with cubic symmetry, thermal conductivity is usually expressed in scalar form as

$$\kappa = \frac{1}{3k_B T^2 V} \int_0^\infty dt \langle \mathbf{S}(0) \cdot \mathbf{S}(t) \rangle, \quad (2.32)$$

in which thermal conductivity is averaged over three diagonal terms. For low-dimensional materials without cubic symmetry, such as nanowire and nanotube, thermal conductivity should be calculated according to Eq. (2.31).

2.5.2 Overview of Different Implementations

The main difficulty to implement GKF in practical calculations arises from how to carry out the integral in Eq. (2.31) and Eq. (2.32) up to infinity. In this section, we review existing different implementations of GKF in literature. Most of them can be categorized into two types: one is the time-domain approach, and the other is the frequency-domain approach.

The time-domain approach is to handle GKF in time-domain. The simplest way is the direct integration method [118] which replaces the integral with summation and numerically records HCACF in time-domain as

$$\begin{aligned} Cor(t) &= \langle S_\nu(0)S_\mu(t) \rangle \\ &= \frac{1}{N-m} \sum_{n=0}^{N-m} [S_\nu(nt_0)S_\mu((n+m)t_0)], \end{aligned} \quad (2.33)$$

where t_0 is the time step, N is the total number of time steps in EMD simulations, and $m = t/t_0$ is the integer number for time t . In this method, the infinite integral in GKF is replaced by a summation up to a finite cut-off time τ_c

$$\kappa_{\mu\nu} = \frac{t_0}{k_B T^2 V} \sum_{t=0}^{\tau_c} Cor(t), \quad (2.34)$$

In addition to direct integration, several alternatives have also been proposed by making use of certain statistical properties of HCACF. For instance, the single exponential function was first used to fit HCACF [110]

$$Cor(t) = g e^{-t/\tau_0}, \quad (2.35)$$

and thermal conductivity is obtained by analytically calculating the infinite integral in GKF

$$\kappa_{\mu\nu} = \frac{g\tau_0}{k_B T^2 V}. \quad (2.36)$$

Later, Che *et al.* [111] found that in contrary to a single exponential decay, HCACF generally first decreases very fast at the beginning, and then decreases much slower in the long-time tail. To take into account this two-stage decaying characteristic of HCACF, Che *et al.* proposed to fit HCACF based on the double exponential function, and then calculate thermal conductivity based on the fitting parameters as [111]

$$Cor(t) = A_o e^{-t/\tau_o} + A_a e^{-t/\tau_a}, \quad (2.37)$$

$$\kappa_{\mu\nu} = \frac{A_o \tau_o + A_a \tau_a}{k_B T^2 V}. \quad (2.38)$$

The frequency-domain approach is an indirect way to handle GKF in frequency-domain by using Fourier transform and Wiener-Khinchin theorem. From mathematical point of view, one can consider GKF in Eq. (2.32) as the Fourier transform of HCACF, and thus can further define spectral thermal conductivity as

$$\kappa(\omega) = \frac{1}{3k_B T^2 V} \int_0^\infty dt \langle \mathbf{S}(0) \cdot \mathbf{S}(t) \rangle e^{i\omega t}, \quad (2.39)$$

in which the conventional thermal conductivity can be regarded as the spectral thermal conductivity in the static limit $\omega \rightarrow 0$. Similarly, spectral heat current can be defined as

$$\mathbf{S}(\omega) = \int_0^\infty dt \mathbf{S}(t) e^{i\omega t}. \quad (2.40)$$

Wiener-Khinchin theorem [119] asserts that in a stationary random process, the power spectral density is the Fourier transform of the corresponding autocorrelation function. Thus according to Wiener-Khinchin theorem, the heat current power spectral density can be written as

$$|\mathbf{S}(\omega)|^2 = \int_0^\infty dt \langle \mathbf{S}(0) \cdot \mathbf{S}(t) \rangle e^{i\omega t}. \quad (2.41)$$

Therefore, thermal conductivity can be calculated from the spectral density of heat current as [112]

$$\begin{aligned}\kappa &= \kappa(\omega)|_{\omega=0} \\ &= \frac{1}{3k_B T^2 V} |\mathbf{S}(\omega)|^2|_{\omega=0}.\end{aligned}\tag{2.42}$$

Strictly speaking, thermal conductivity can only be obtained from this method in the static limit $\omega \rightarrow 0$, which is in practice infeasible due to the finite time simulation. Therefore, the static limit is simply approximated by extrapolating the high frequency data to zero frequency [112]. Later, this spectral method was improved by Volz *et al.* [113] with the assumption of single exponential decay of HCACF in Eq. (2.35). Based on this assumption, the spectral thermal conductivity is then fitted at high frequency according to [113]

$$\kappa(\omega) = \frac{\kappa(0)}{1 + i\omega\tau_0},\tag{2.43}$$

where $\kappa(0)$ and τ_0 are two fitting parameters, corresponding to the static thermal conductivity and single exponential decay constant, respectively. In this method, the static thermal conductivity is obtained as the fitting parameter, thus no extrapolation is involved.

2.5.3 Improvement of Accuracy

In principle, the integral time in GKF should be infinitely long [108, 109] which is computationally infeasible. For any finite time simulation, the accuracy of HCACF calculated from Eq. (2.33) is limited by the total simulation time, which corresponds to the maximum ensemble average of the correlation function at $t=0$. HCACF becomes less accurate over time because of the smaller ensemble average

one can get from a finite time simulation. Therefore, numerical error (noise) is inevitably introduced into the calculation, and eventually can contaminate HCACF when it decays to a small value. Consequently, HCACF is only reliable up to a finite time (cut-off time τ_c). Thus, thermal conductivity can only be calculated from the truncated HCACF, which introduces the ambiguity and has caused controversial results in literatures [110, 111, 113, 118, 120, 121]. For instance, Che *et al.* [111] used a double exponential function to fit HCACF and their calculation result of thermal conductivity of diamond crystal was 60% lower than the experimental value at room temperature. They attributed this discrepancy to the accuracy of the empirical force field used in their simulations [111]. Schelling *et al.* [118] compared exponential fitting with direct integration and argued that the exponential fittings gives rise to an underestimated value of thermal conductivity.

In this section, we discuss how to improve the accuracy of thermal conductivity calculations based on GKF with the time-domain approach in EMD simulations. We propose a quantitative method to accurately determine the cut-off time of HCACF. Moreover, we suggest a correction to the double-exponential-fitting method based on physical argument. Using crystalline silicon and germanium as examples, we demonstrate that our proposed methods can give rise to the computation values of thermal conductivity in an excellent agreement with experimental ones.

In our simulations, we restrict ourselves to the high temperature regime where quantum effect can be neglected and classical MD simulation is expected to be highly valid [74]. SW potential (Chap. 2.2) is used to derive the force term.

According to Hardy's formulation [122], heat current can be defined as [118]

$$\mathbf{S} = \sum_i \mathbf{v}_i \varepsilon_i + \frac{1}{2} \sum_{\substack{i,j \\ i \neq j}} \mathbf{r}_{ij} (\mathbf{F}_{ij} \cdot \mathbf{v}_i) + \frac{1}{6} \sum_{\substack{i,j,k \\ i \neq j, j \neq k}} (\mathbf{r}_{ij} + \mathbf{r}_{ik}) (\mathbf{F}_{ijk} \cdot \mathbf{v}_i), \quad (2.44)$$

where \mathbf{v}_i and ε_i are the velocity and total energy of atom i , respectively, and \mathbf{F}_{ij} and \mathbf{F}_{ijk} denote the 2-body and 3-body force, respectively. The first term on the right-hand side of Eq. (2.44) describes the heat convection typically occurring in fluids, while the rest terms describe the heat conduction between the atoms, which is dominant part in solids [113]. Therefore, heat current can be simplified as [113]

$$\mathbf{S} = \frac{1}{2} \sum_{\substack{i,j \\ i \neq j}} \mathbf{r}_{ij} (\mathbf{F}_{ij} \cdot \mathbf{v}_i) + \frac{1}{6} \sum_{\substack{i,j,k \\ i \neq j, j \neq k}} (\mathbf{r}_{ij} + \mathbf{r}_{ik}) (\mathbf{F}_{ijk} \cdot \mathbf{v}_i), \quad (2.45)$$

which is computationally more efficient as the calculation of energy is not required.

Zero net momentum for the whole system is implicitly required in our simulations [111]. Numerically, velocity Verlet algorithm (Chap. 2.3) is employed to integrate Newton's equations of motion, and each MD step is set as 0.8 fs. A cubic super cell of $N \times N \times N$ unit cells is used, and periodic boundary conditions are applied to the super cell in all three directions. For each realization, all the atoms are initially placed at their equilibrium positions but have a random velocity according to Gaussian distribution. Canonical ensemble MD with Langevin heat reservoir first runs for 10^5 steps to equilibrate the whole system at 1000 K (Debye temperature of Si is 658 K [123]). Then micro-canonical ensemble MD runs for another 2×10^6 steps and heat current is collected at each step.

To explicitly check the effect of heat current definitions for SW silicon, we calculate HCACF based on heat current defined in Eq. (2.44) and Eq. (2.45) using the same computational code. Fig. 2.8 shows four realizations of HCACF in a $4 \times 4 \times 4$ super cell at 1000 K. The red solid line and blue dashed line draw

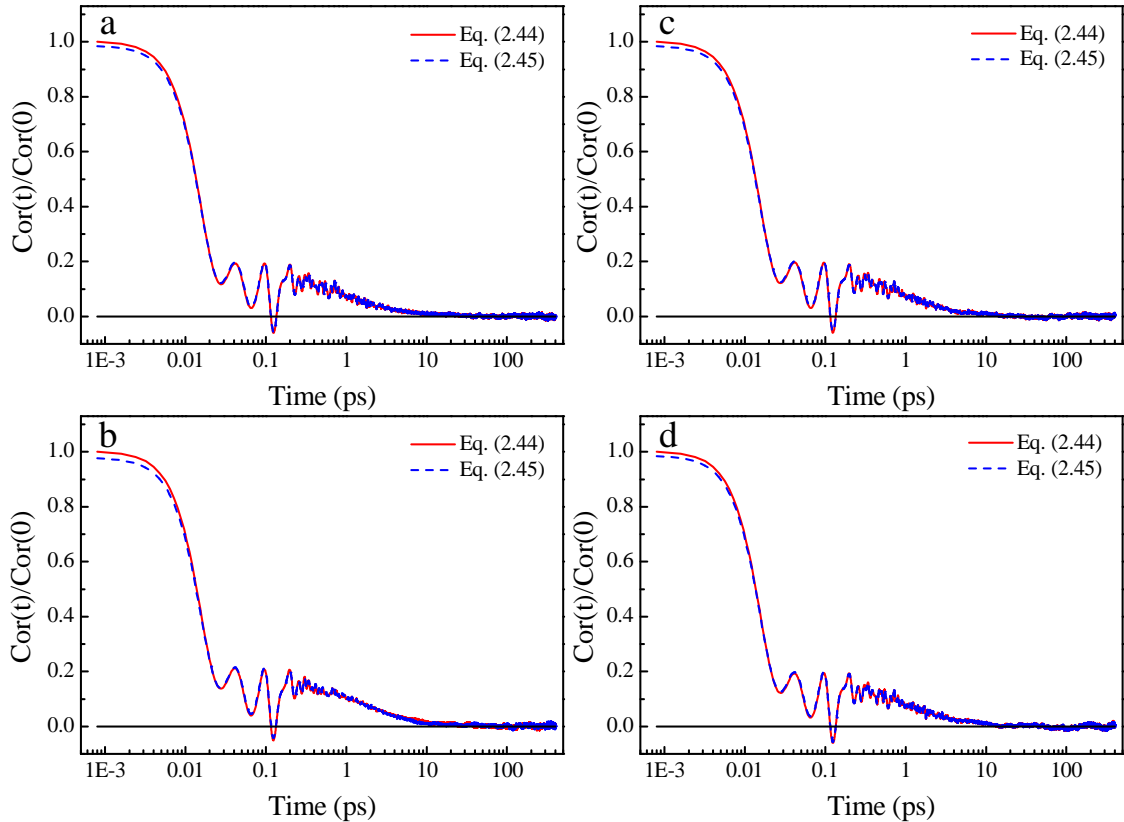


Figure 2.8: Time dependence of normalized heat current autocorrelation function based on different definitions of heat current. Here we show four realizations of HCACF in a $4 \times 4 \times 4$ super cell at 1000 K. The red solid line and blue dashed line draw calculation results based on heat current defined in Eq. (2.44) and Eq. (2.45), respectively. The black line draws the zero-axis for reference.

calculation results based on heat current defined in Eq. (2.44) and Eq. (2.45), respectively. It can be seen from this figure that these two curves almost overlap with each other, suggesting that the convection term in Eq. (2.44) can be omitted in the EMD simulation of SW silicon.

In the rest part of this chapter, the definition of heat current in Eq. (2.44) is used in the EMD simulation, consistent with a previous theoretical study [118]. Thermal conductivity is calculated from direct integration method according to Eq. (2.33) and Eq. (2.34). In the following part, thermal conductivity calculated from direct integration up to different cut-off time is referred as “accumulative thermal conductivity κ_a ”. The final result is averaged over 8 realizations with different initial conditions. We have calculated even more realizations and find that good convergence already can be obtained with 8 realizations.

Fig. 2.9a and 2.9d show the time dependence (0-400 ps) of the normalized HCACF for two typical realizations in a $4 \times 4 \times 4$ super cell (other realizations are similar). In all the realizations, HCACF has a very rapid decay at the beginning, followed by a long tail which has a much slower decay. This two-stage decaying characteristic of HCACF has been found in the study of various materials [111, 114, 118, 121]. The rapid decay corresponds to the contribution from short wavelength phonons to thermal conductivity, while the slower decay corresponds to the contribution from long wavelength phonons, which is the dominating part in thermal conductivity [111, 121]. Moreover, it is shown in Fig. 2.9 that HCACF decays to approximately zero at a time much shorter than the total simulation time of 1.6 ns. It has also been checked that even for the largest super cell size $N=12$ considered in our study, the HCACF still can be well relaxed within 1.6 ns, which means the total simulation time of 1.6 ns is adequate for the present study.

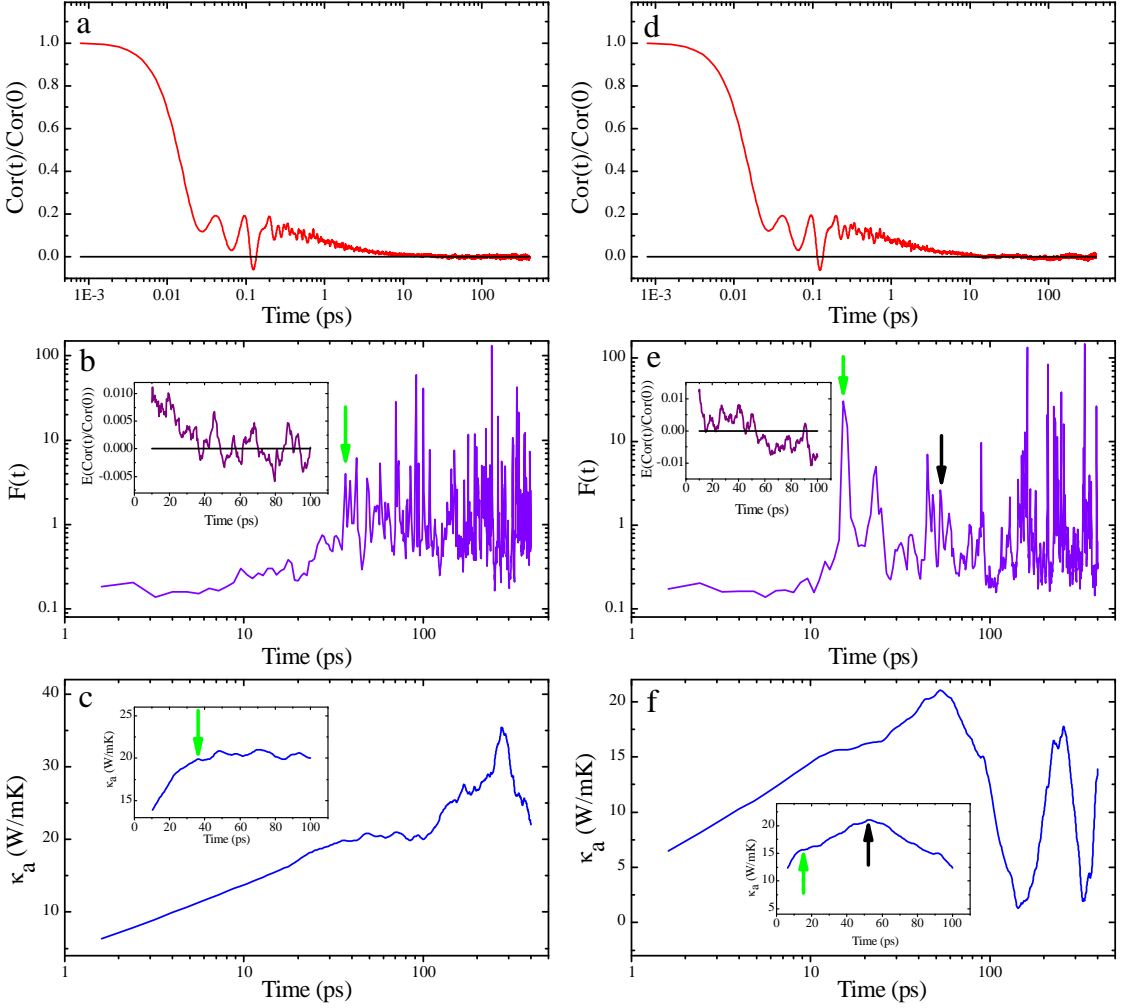


Figure 2.9: **Time dependence of normalized heat current autocorrelation function $\text{Cor}(t)/\text{Cor}(0)$ (red line), relative fluctuation of $\text{Cor}(t)$ (violet line), and accumulative thermal conductivity κ_a (blue line) for two typical realizations in a $4 \times 4 \times 4$ super cell.** A total time of 400 ps is plotted in the log-scale. Insets in b and e show the time dependence of the mean value of the normalized HCACF (purple line). The green and black arrows pinpoint the cut-off time estimated by first avalanche and first dip, respectively. The black line draws the zero-axis for reference.

Therefore, the following part of this section will be focused on how to improve the accuracy of EMD calculations of thermal conductivity for a given finite total simulation time.

In order to get a quantitative description of the numerical error, we define the relative fluctuation of HCACF as

$$F(t) = \left| \frac{\sigma(Cor(t))}{E(Cor(t))} \right|, \quad (2.46)$$

where σ and E denote the standard deviation and mean value of HCACF in the time interval $(t, t + \delta)$, respectively. In Fig. 2.9b and 2.9e we plot $F(t)$ for the above-mentioned two typical realizations. δ is chosen as 0.8 ps (10^3 time steps), and it has been verified that our estimation of τ_c is insensitive to δ . As shown in Fig. 2.9b and 2.9e, before a critical time, the relative fluctuation of HCACF $F(t)$ maintains a small value (e.g., less than 1) and does not change significantly. This indicates that HCACF is still reliable as it shows no large fluctuation. After the critical time, $F(t)$ suddenly jumps to a large value, and changes value drastically over time, which is a typical signature of the random noise. This indicates that HCACF has been contaminated and dominated by computational error, and thus is no longer reliable. In our study, we define this critical time (when $F(t)$ becomes larger than one) as the cut-off time, as marked by the green arrow in Fig. 2.9. We refer this method to estimate τ_c as “first avalanche” (FA) in this study. The essence of FA is to only take into account those contributions from HCACF which is before τ_c and discard the rest part of HCACF as noise. It is worth mentioning that the tiny but non-zero noise can accumulate over time and change the value of accumulative thermal conductivity dramatically as shown in Fig. 2.9c and 2.9f.

There are some factors which lead to the variation of the cut-off time. For

different realizations with the same super cell size, different initial conditions represent different samples of a thermodynamic ensemble, and they are not exactly equivalent to each other in a finite time simulation. This leads to a fluctuation of cut-off time with respect to different realizations as shown in Fig. 2.9. Moreover, in a larger super cell which contains longer wavelength phonon modes, HCACF decays slower than in a smaller super cell, thus increasing the cut-off time correspondingly. Therefore, simply selecting a unique cut-off time for different realizations and different super cell size can lead to suspicious value of thermal conductivity with quite large error bar [118].

In order to suppress the fluctuation in the calculation of thermal conductivity, we propose to search for the cut-off time and its corresponding accumulative thermal conductivity on a case-by-case basis, for both different realizations and different super cell size. Fig. 2.10a shows the calculation results for thermal conductivity of the crystalline silicon using the direct integration method with case-by-case based FA calculations. Due to the periodic boundary condition, finite size effect exists in the calculated thermal conductivity when simulation domain is small [111, 118]. In our simulations, the thermal conductivity of Si crystal saturates to about 31 W/mK (see Tab. 2.1) when the super cell size $N \geq 10$ unit cells. This saturated value is in excellent agreement with experimental result of 31.0 W/mK from Ref. [124, 125] at the same temperature. Moreover, a much smaller error bar is obtained in our study compared with those shown in literature [111, 118].

It is worth pointing out that there are other methods to obtain the cut-off time, such as the first dip (FD) method in which τ_c is the time when the tail of HCACF first decays to zero [110]. For FD method, τ_c corresponds to the time when $\kappa_a(t)$ first reaches a plateau or a peak. However, we found that the estimation

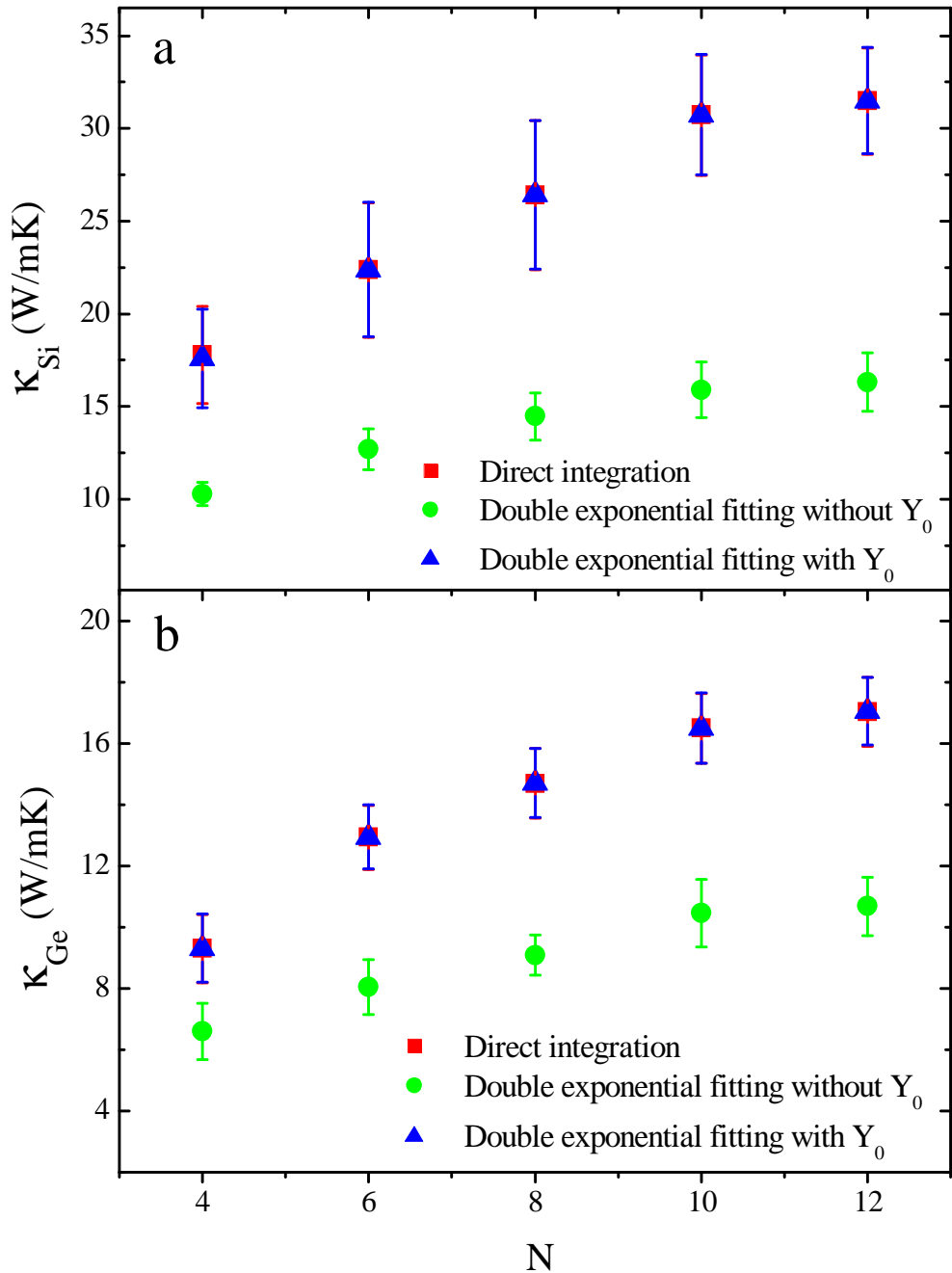


Figure 2.10: Calculated thermal conductivity versus super cell size ($N \times N \times N$ unit cells) from different methods with first avalanche at 1000 K. a Crystalline silicon. b Crystalline germanium. The symbols square, dot, and triangle denote calculation results based on direct integration and double-exponential-fitting without/with Y_0 , respectively.

Table 2.1: **EMD simulation results for thermal conductivity of crystalline silicon at 1000 K.** Experimental value is 31.0 W/mK from Ref. [124, 125]. A cubic super cell of $N \times N \times N$ unit cells is used, and the unit cell length of Si is 0.543 nm. κ_D denotes the calculation results using direct integration. κ_C and κ_F denote the calculation results using double exponential fitting without and with Y_0 , respectively.

N	Number of atoms	κ_D (W/mK)	κ_C (W/mK)	κ_F (W/mK)
4	512	17.78±2.61	10.27±0.63	17.59±2.66
6	1728	22.36±3.62	12.69±1.10	22.39±3.62
8	4096	26.41±4.02	14.47±1.27	26.42±4.01
10	8000	30.72±3.24	15.90±1.49	30.74±3.23
12	13824	31.48±2.86	16.31±1.57	31.50±2.85

of τ_c by FD method is not always reliable. When an obvious plateau in κ_a can be observed (shown in Fig. 2.9c), FD can make estimation of τ_c quite close to that estimated by FA. Consequently, both two methods can give estimation of thermal conductivity quite close to each other. In this case, the mean value of the normalized HCACF fluctuates around zero in a relatively short time (see insets in Fig. 2.9b). As a result, the noise does not accumulate over time, giving rise to a plateau in κ_a with small fluctuations. However, in the case without any obvious plateau in κ_a (shown in Fig. 2.9f), FD estimates τ_c (according to the peak in κ_a) to be about 52 ps (marked by black arrow), while $F(t)$ shows that HCACF has been already contaminated by noise after about 15 ps. In this case, FD overestimates the thermal conductivity by falsely taking into account the contribution from the

positive noise (see insets in Fig. 2.9e). This indeed can become a very serious problem when the noise remains positive over a very long time in some realizations (not shown here). Therefore, in our study, the cut-off time in all the realizations are estimated by FA.

Previous EMD simulations of SW silicon by Schelling *et al.* [118] reported $\kappa \sim 60$ W/mK at 1000 K using the direct integration method. In their work, the cut-off time was determined by empirical observation of the accumulative thermal conductivity versus time, even though no constant plateau was observed in the long-time limit. As already discussed above, the cut-off time can vary in different realizations and simulation domain size due to the finite simulation time. Selecting a unique and long enough cut-off time based on empirical observation can induce large fluctuation in the calculation of thermal conductivity (see Fig. 2.9), which is a serious issue in the practical EMD calculations with the finite simulation time and only a few independent realizations. The exact way to determine the cut-off time may cause the discrepancy between the calculation results presented in this thesis and those results in Ref. [118].

We have demonstrated that direct integration with FA on a case-by-case basis can be quite efficient to make a successful prediction of thermal conductivity and suppress the error bar. In the following part, we demonstrate the availability of a non-zero correction in the double exponential fitting approach. In our method, HCACF is fitted according to the following function

$$Cor(t)/Cor(0) = A_1 e^{-t/\tau_1} + A_2 e^{-t/\tau_2} + Y_0, \quad (2.47)$$

in which A_1 , A_2 , τ_1 , τ_2 , and Y_0 are fitting parameters. The decay of HCACF in bulk material will be exponential due to the macroscopic law of relaxation and

Onsager's postulate for microscopic thermal fluctuation [111]. It has been reported that the relaxation times generally decreases with increasing phonon frequency [126]. In bulk Silicon, the relaxation times of acoustic phonon (both longitudinal and transverse) are from one to hundreds ps, with the phonon frequency range is from 0 to 13 THz. However, for optical phonons (both longitudinal and transverse) with frequency greater than 13 THz, the relaxation times are from 1 to 10 ps, much shorter than those for acoustic phonons [126]. Thus in HCACF, the initial fast decay is due to the high frequency phonon modes, while the slow decay corresponds to the low frequency phonon modes. The time constant τ_1 and τ_2 correspond to the relaxation time of short wavelength and long wavelength phonons, respectively. Levenberg-Marquardt algorithm is used in the nonlinear least-square fitting.

The essential difference between Eq. (2.47) and Eq. (2.37) is the constant Y_0 . In our calculations, we first search for the cut-off time τ_c based on FA method, and then HCACF before τ_c is fitted according to Eq. (2.47). Finally, a finite time of integration up to τ_c based on Eq. (2.47) yields

$$\begin{aligned}\kappa &= \frac{1}{3k_B T^2 V} \int_0^{\tau_c} dt \text{Cor}(t) \\ &= \frac{1}{3k_B T^2 V} \int_0^{\tau_c} dt \text{Cor}(0)(A_1 e^{-t/\tau_1} + A_2 e^{-t/\tau_2} + Y_0) \\ &= \frac{\text{Cor}(0)}{3k_B T^2 V} [A_1 \tau_1 (1 - e^{-\tau_c/\tau_1}) + A_2 \tau_2 (1 - e^{-\tau_c/\tau_2}) + Y_0 \tau_c].\end{aligned}\quad (2.48)$$

At the cut-off time τ_c , the normalized HCACF decays to a very small value Y_0 (see the following section for more discussion), and those two terms $e^{-\tau_c/\tau_1}$ and $e^{-\tau_c/\tau_2}$ are negligible compared to unity. This can further simplify Eq. (2.48) to

the following equations

$$\kappa_C = \frac{Cor(0)}{3k_B T^2 V} (A_1 \tau_1 + A_2 \tau_2), \quad (2.49)$$

$$\kappa_F = \frac{Cor(0)}{3k_B T^2 V} (A_1 \tau_1 + A_2 \tau_2 + Y_0 \tau_c), \quad (2.50)$$

in which κ_C and κ_F means excluding and including the contribution from Y_0 , respectively.

Fig. 2.10a shows the calculation results based on double-exponential-fitting without and with Y_0 . In both cases, thermal conductivity saturates to a constant value with the increase of super cell size. Without Y_0 , the saturated value for κ_C is about 16 W/mK (see Tab. 2.1), which is only about half of the experimental value. This underestimation of thermal conductivity is quite similar to what was found in literatures [111, 113, 118]. With Y_0 correction, which is typically on the order of 10^{-3} for most of the realizations, the saturated value for κ_F is about 31 W/mK, in good agreement with experimental value [124, 125]. As shown in Tab. 2.1, double-exponential-fitting with Y_0 actually reproduces the same result as that calculated from direct integration, which indicates that this tiny but nonzero term Y_0 is physical rather than just a numerical error.

Fig. 2.11 shows the raw data and the corresponding fitted curve according to double-exponential-fitting (Eq. (2.47)) of the normalized HCACF before the cut-off time for the same two realizations shown in Fig. 2.9. The fitted curve can well fit the slow decay region of HCACF, which makes the dominating contribution to the thermal conductivity. The insets show the long time region near cut-off time (marked by the green arrow). At this region, although the raw data of HCACF can reach zero due to the fluctuation of noise, its average contribution (envelope) over time is not zero due to the finite cut-off time, and corresponds to the tiny

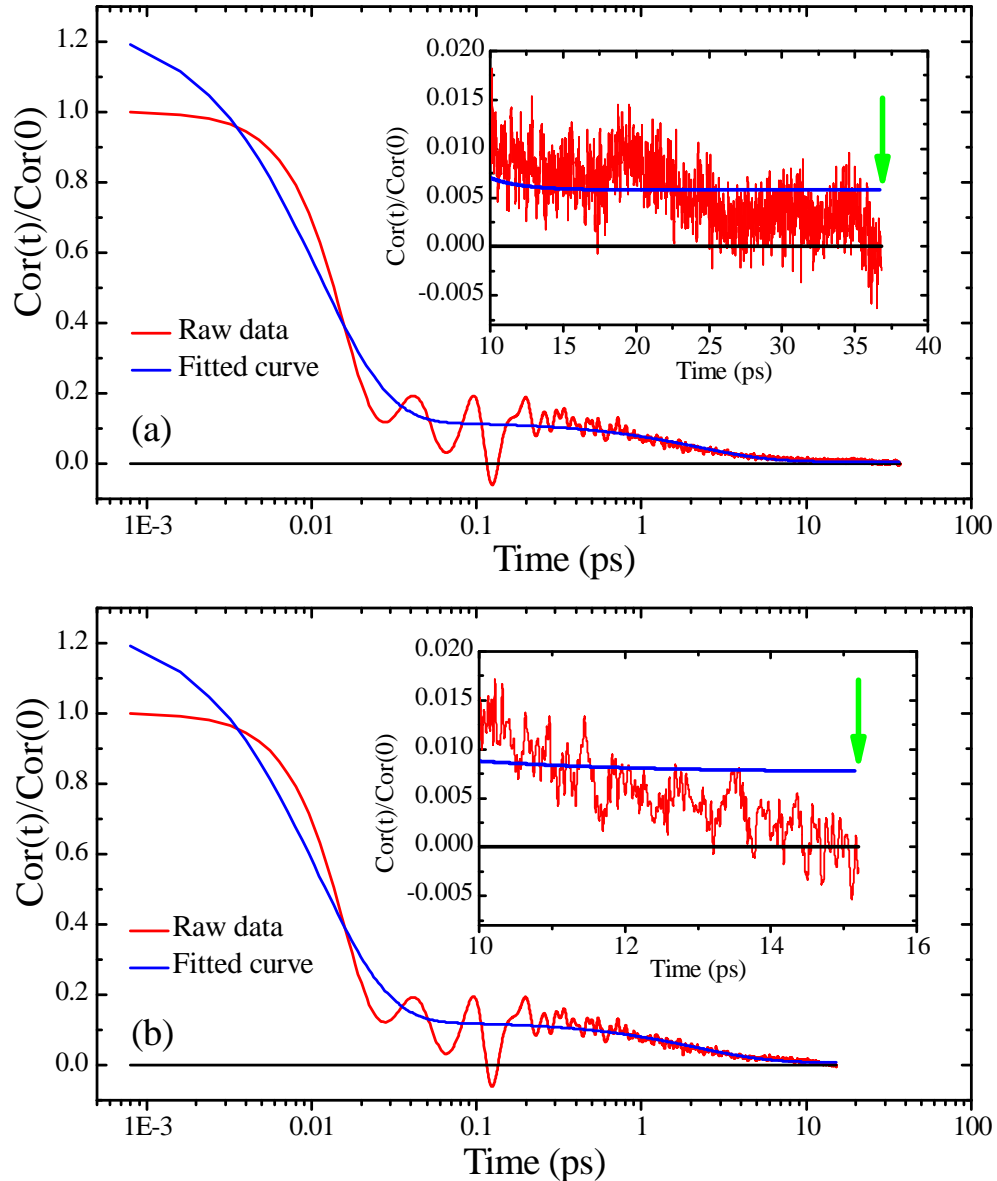


Figure 2.11: Raw data (red line) and the corresponding fitted curve according to double exponential fitting (blue line) of the normalized heat current autocorrelation function before the cut-off time (denoted by green arrow) in a $4 \times 4 \times 4$ super cell for the same two realizations shown in Fig. 2.9. The insets show the long time region near the cut-off time. The black line draws the zero-axis for reference.

term Y_0 . This term originates from the long wavelength phonons which have a longer relaxation time than the cut-off time. In bulk silicon, for acoustic phonons with frequency less than 2 THz, their relaxation times are longer than about 50 ps (generally greater than τ_c). Moreover, it has been demonstrated that phonons with frequency less than 2 THz contribute about 50% to the thermal conductivity of bulk silicon at 1000 K [126]. This is in good agreement with our calculations that excluding Y_0 , the calculated thermal conductivity is only about half of the experimental value. This is the physical origin of the tiny but nonzero Y_0 .

In order to further test the validity of our correction to double-exponential-fitting, we have also calculated the thermal conductivity of crystalline germanium (Debye temperature of Ge is 372 K [123]) at 1000 K. A finite time of cut-off is used in all the calculations according to first avalanche. As shown in Fig. 2.10b, the saturated values of thermal conductivity calculated from direct integration and double exponential fitting with Y_0 are both about 17 W/mK, which is in good agreement with experimental value of 17.1 W/mK at the same temperature from literature [124, 125]. However, excluding Y_0 in the double exponential fitting predicts an underestimated value of about 10 W/mK.

Now we turn to discuss the possible factors that may influence the accuracy of our proposed double-exponential-fitting method. As shown in Fig. 2.11, our method can fit the slow decay region of HCACF (relates to τ_2) very well, but cause deviation from the raw data in the fast decay region (relates to τ_1). However, the time constant τ_2 for long wavelength phonons is more than 100 times larger than τ_1 for short wavelength phonons. As a result, the contributions from short wavelength phonons only account for less than 2% of the overall thermal conductivity. Therefore, this deviation of fitted curve from raw data has little effect on

the accuracy of the calculated thermal conductivity.

The total simulation time is the crucial factor that limits the accuracy of our proposed method. An insufficient total simulation time will lead to the insufficient ensemble average in the calculation of HCACF. Moreover, HCACF may not be well relaxed if the intrinsic relaxation time is larger than the total simulation time. This can cause uncertainty in determining the time constant τ_1 and τ_2 among different realizations, which eventually may compromise the accuracy of calculated thermal conductivity based on double-exponential-fitting. However, as we have already demonstrated in the first part of this study, the total simulation time in our study is adequate enough to ensure the accuracy and relaxation of HCACF. As a result, for all the super cell size considered in this study, we obtain less than 9% deviation in τ_2 for long wavelength phonons, and less than 2% deviation in τ_1 for short wavelength phonons among different realizations.

Moreover, here we only carry out calculation at ambient temperature which is higher than Debye temperature because classical molecular dynamics is only valid in this regime, thus we can solely test the validity of our proposed method without considering quantum effect. To calculate thermal conductivity at ambient temperature which is lower than Debye temperature, quantum correction [74] to classical MD calculations must be considered. In addition, in the case where the mean free path is much longer than the box size, the tails of HCACF cannot be calculated. Thus a larger system size and longer simulation time are needed in order to get well relaxed HCACF. It deserves further investigation on how to combine quantum correction and our proposed approach to calculate thermal conductivity for larger mean free path cases.

2.5.4 Summary

In summary, we have examined different implementations of Green-Kubo formula in EMD simulations. Due to the finite number of ensemble average, HCACF is only reliable up to a cut-off time and thus thermal conductivity can only be calculated from the truncated HCACF. We have proposed an efficient quantitative method (first avalanche) to accurately estimate the cut-off time. Using the cut-off time, direct integration method can make a successful computation of thermal conductivity of crystalline silicon and germanium. In addition, we have demonstrated that because of the finite cut-off time, a small nonzero correction term can significantly improve the accuracy of EMD calculations based on the double-exponential-fitting of HCACF. Excluding this term in the calculation gives rise to an underestimated value of thermal conductivity due to the partial exclusion of contribution from low-frequency phonons, while including it one can make a correct prediction in good agreement with experimental value. Since the two-stage exponential decaying characteristic of HCACF has been found in various materials and has profound underlying physical mechanism, our method is quite general and can have wide applications in accurate thermal conductivity estimations of different materials and systems.

2.6 Brief Introduction to Lattice Dynamics

Lattice dynamics [127] is a widely used tool to study the dynamics of the crystal in terms of normal mode (eigenmode) for the equation of motion. The normal mode is the collective excitation of lattice vibration, and its quantization is known as phonon, which is a quasi-particle associated with energy $\hbar\omega$. In this

section, we briefly review the standard approach to determine the eigenmodes of a lattice structure, and introduce the computational platform to calculate them for realistic materials.

Consider a general three-dimensional crystal with N_1 unit cells and N_2 atoms per unit cell. Any atom in the crystal can be specified by two integer number l and b , where l is the index for unit cell ($1 \leq l \leq N_1$), and b is the index for atom within one unit cell ($1 \leq b \leq N_2$). The position of atom (lb) can be tracked through

$$\mathbf{R}(lb) = \mathbf{R}_l + \mathbf{R}_b, \quad (2.51)$$

where \mathbf{R}_l is the position of l th unit cell, \mathbf{R}_b is the position of b th atom within the unit cell. The displacement relative to equilibrium position can be expressed as

$$\mathbf{x}(lb) = \mathbf{R}(lb) - \mathbf{R}_0(lb), \quad (2.52)$$

where $\mathbf{R}_0(lb)$ denotes the equilibrium position of atom (lb). The potential energy of the crystal can be expanded in Taylor series of the displacement $\mathbf{x}(lb)$ as

$$\begin{aligned} V = & V_0 + \sum_{lb} \sum_{\alpha} \frac{\partial V}{\partial x_{\alpha}(lb)} \Big|_0 x_{\alpha}(lb) \\ & + \frac{1}{2} \sum_{lb, l'b'} \sum_{\alpha, \beta} \frac{\partial^2 V}{\partial x_{\alpha}(lb) \partial x_{\beta}(l'b')} \Big|_0 x_{\alpha}(lb) x_{\beta}(l'b') \\ & + \frac{1}{3!} \sum_{lb, l'b', l''b''} \sum_{\alpha, \beta, \gamma} \frac{\partial^3 V}{\partial x_{\alpha}(lb) \partial x_{\beta}(l'b') \partial x_{\gamma}(l''b'')} \Big|_0 \\ & \times x_{\alpha}(lb) x_{\beta}(l'b') x_{\gamma}(l''b'') \\ & + \dots \\ = & V_0 + V_1 + V_2 + V_3 + \dots, \end{aligned} \quad (2.53)$$

where V_0 is a constant (usually set to zero for simplicity), and α , β and γ are the indices for cartesian coordinate. The equilibrium state can be expressed as

$$\frac{\partial V}{\partial \mathbf{x}(lb)} \Big|_0 = 0. \quad (2.54)$$

As the deviation from equilibrium is small at low temperature, Taylor expansion to the second order gives the harmonic approximation of the potential energy as

$$V = V_2 = \frac{1}{2} \sum_{lb, l'b'} \sum_{\alpha, \beta} \Phi_{\alpha\beta}(lb, l'b') x_{\alpha}(lb) x_{\beta}(l'b'), \quad (2.55)$$

where Φ is the interatomic force constant matrix at equilibrium

$$\Phi_{\alpha\beta}(lb, l'b') = \left. \frac{\partial^2 V}{\partial x_{\alpha}(lb) \partial x_{\beta}(l'b')} \right|_0, \quad (2.56)$$

which has the property of translational invariance as

$$\Phi_{\alpha\beta}(lb, l'b') = \Phi_{\alpha\beta}(0b, (l' - l)b'). \quad (2.57)$$

Under the harmonic approximation, the equation of motion for atom (lb) can be written as

$$m_{lb} \ddot{x}_{\alpha}(lb) = - \sum_{l'b'} \sum_{\beta} \Phi_{\alpha\beta}(lb, l'b') x_{\beta}(l'b'). \quad (2.58)$$

The solution to Eq. (2.58) can be written in the general form as

$$\mathbf{x}(lb) = \sum_{\mathbf{k}, s} \mathbf{X}^b(\mathbf{k}, s) \exp(i[\mathbf{k} \cdot \mathbf{x}(lb) - \omega(\mathbf{k}, s)t]), \quad (2.59)$$

where \mathbf{k} is the wave-vector, s is the branch index, and ω is the frequency. The relation between ω and \mathbf{k} is known as the phonon dispersion relation. Substitute Eq. (2.59) into Eq. (2.58), the equation of motion reads

$$m_b \omega^2(\mathbf{k}, s) X_{\alpha}^b(\mathbf{k}, s) = \sum_{l'b'} \sum_{\beta} \Phi_{\alpha\beta}(0b, l'b') \exp(i\mathbf{k} \cdot [\mathbf{x}(l'b') - \mathbf{x}(0b)]) X_{\beta}^{b'}(\mathbf{k}, s). \quad (2.60)$$

If we further define the column vector $\mathbf{e}(\mathbf{k}, s)$ ($1 \times 3N_2$) as

$$\mathbf{e}(\mathbf{k}, s) = \begin{pmatrix} \sqrt{m_1} X_x^1(\mathbf{k}, s) \\ \sqrt{m_1} X_y^1(\mathbf{k}, s) \\ \sqrt{m_1} X_z^1(\mathbf{k}, s) \\ \vdots \\ \vdots \\ \sqrt{m_{N_2}} X_x^{N_2}(\mathbf{k}, s) \\ \sqrt{m_{N_2}} X_y^{N_2}(\mathbf{k}, s) \\ \sqrt{m_{N_2}} X_z^{N_2}(\mathbf{k}, s) \end{pmatrix}, \quad (2.61)$$

then Eq. (2.60) can be written in a neat form as

$$\omega^2(\mathbf{k}, s)\mathbf{e}(\mathbf{k}, s) = \mathbf{D}(\mathbf{k})\mathbf{e}(\mathbf{k}, s), \quad (2.62)$$

where \mathbf{D} is a $3N_2 \times 3N_2$ matrix known as the dynamical matrix with matrix element defined as

$$D_{\alpha\beta}(b, b', \mathbf{k}) = \frac{1}{\sqrt{m_b m_{b'}}} \sum_{l'} \Phi_{\alpha\beta}(0b, l'b') \exp(i\mathbf{k} \cdot [\mathbf{x}(l'b') - \mathbf{x}(0b)]). \quad (2.63)$$

To solve Eq. (2.62), it is now mathematically a standard eigenvalue problem for a $3N_2 \times 3N_2$ matrix, which in principle has $3N_2$ eigenvalues and corresponding eigenvectors. In physical systems, the dynamical matrix is Hermitian, i.e. $\mathbf{D}^T(\mathbf{k}) = \mathbf{D}^*(\mathbf{k})$, so that all the eigenvalues are real numbers.

To calculate the eigenmodes for realistic materials, we use the “General Utility Lattice Program” (GULP) developed by Gale [128]. GULP is a very useful computational platform to study the physical properties of many lattice structures. It is capable of treating systems of all dimensionalities. With GULP, it is possible

to model many different systems, such as cluster, embedded defects, polymers, surfaces and bulk materials, and a wide range of force fields are included. In addition, GULP is an open source computer program and available free of charge to the academics. More details about GULP can be found at its website [129].

To further characterize the eigenmode, here we introduce an important quantity known as participation ratio, which can quantitatively describe the phonon localization effect for each eigenmode λ as [130]

$$P_\lambda^{-1} = N \sum_i \left(\sum_\alpha e_{i\alpha,\lambda}^* e_{i\alpha,\lambda} \right)^2, \quad (2.64)$$

where N is the total number of atoms, and $e_{i\alpha,\lambda}$ is the α th eigenvector component of eigenmode λ for the i th atom. Each eigenmode λ is specified by the wave-vector \mathbf{k} and branch index s . The participation ratio measures the fraction of atoms participating in a given mode, and effectively indicates the localized modes with $O(1/N)$ and delocalized modes with $O(1)$.

Fig. 2.12 shows the calculated participation ratio in bulk Si (solid circle). Due to the perfect periodicity in all directions of bulk Si, all eigenmodes are delocalized (propagating) with participation ratio equal to 1. Also shown in Fig. 2.12 for comparison is the participation ratio for SiNWs in Γ L direction. Due to the surface dangling bond atoms in SiNWs which breaks the perfect periodicity of the diamond structure, most of the eigenmodes in SiNWs are less than 1, except for some modes near Γ point. This figure clearly demonstrates that participation ratio can effectively identify the localization effect of eigenmodes in a given lattice structure.

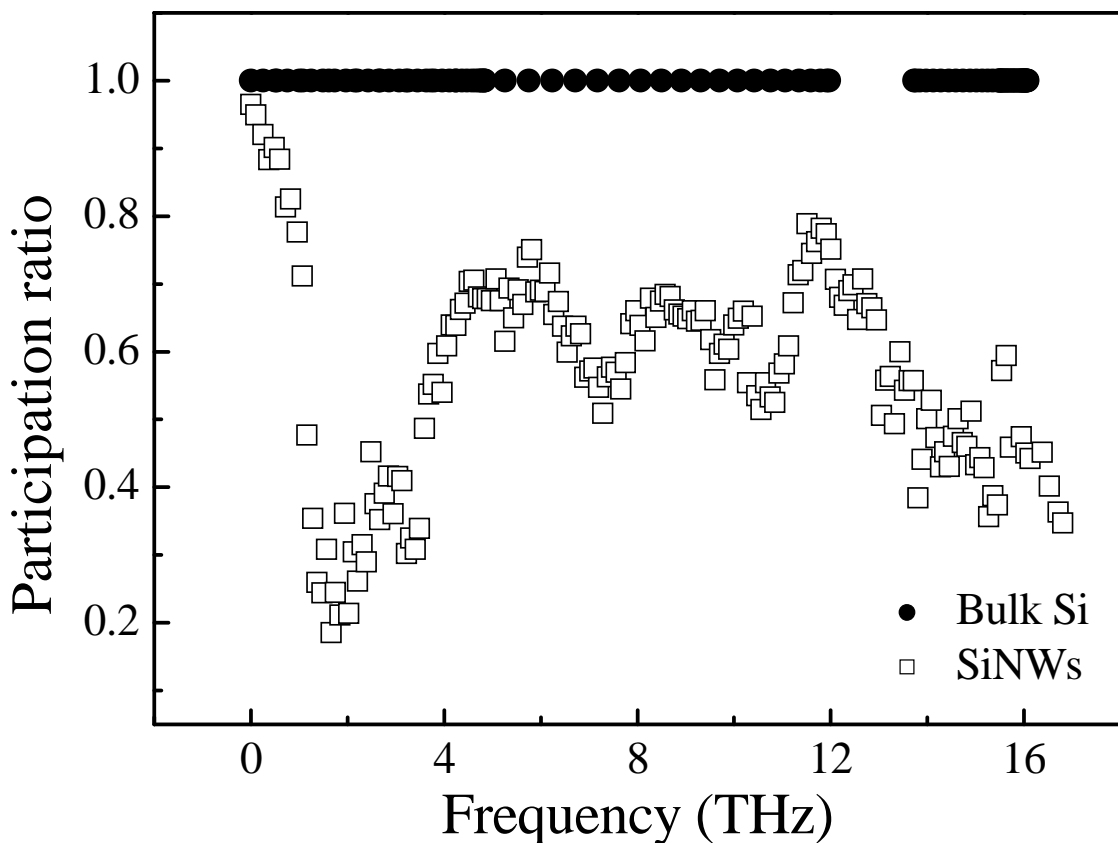


Figure 2.12: Typical participation ratio for bulk Si and SiNWs. Eigenmodes are computed in Γ L direction for both bulk Si and SiNWs.

Chapter 3

Tunable Thermal Conductivity of $\text{Si}_{1-x}\text{Ge}_x$ Nanowires

In this chapter, we demonstrate that thermal conductivity of Silicon/Germanium nanowires ($\text{Si}_{1-x}\text{Ge}_x$ NWs) depends on the composition remarkably. With 50% Ge content, thermal conductivity of $\text{Si}_{1-x}\text{Ge}_x$ NWs reaches the minimum, which is about 18% of that of pure SiNWs. More interesting, with only 5% doping of Ge atoms, thermal conductivity of SiNWs is reduced 50%. The reduction of thermal conductivity mainly comes from the localization of phonon modes due to random scattering. In addition, we also investigate the thermal conductivity of Si/Ge superlattice structured NWs with changeable period length. The dependence of thermal conductivity on the period length is explained by the overlap of phonon power spectrum. Our results demonstrate that $\text{Si}_{1-x}\text{Ge}_x$ NWs might have promising application in thermoelectrics.

3.1 Motivation

Silicon and Germanium can form a continuous series of substitutional solid, $\text{Si}_{1-x}\text{Ge}_x$. Single crystalline $\text{Si}_{1-x}\text{Ge}_x$ nanowires (NWs) have been grown and the electronic band gap modulation with composition has been reported [131]. Recently, the experimental synthesis of core-shell structures [12] provides intriguing opportunities for the development of nanowire based devices. One of the promising applications for nanowires is as thermoelectric cooler [44, 45]. In thermoelectric applications, low thermal conductivity is preferred to increase the figure of merit [54, 132, 133]. In SiNWs, there exhibits 100-fold reduction of thermal conductivity because of the strong boundary inelastic scattering of phonons [44, 45, 134]. However, it is still indispensable to reduce the thermal conductivity of SiNWs further in order to achieve high thermoelectric performance. One possible way to arrive this is by means of compound. In this case, $\text{Si}_{1-x}\text{Ge}_x$ NWs seem to be a promising candidate because both Si and Ge belong to the same group in the periodic table, have the same crystal structure, and display total solubility. In spite of an increasing number of works devoted to the electronic and optical properties [135–137], very little has been done for thermal conductivity of $\text{Si}_{1-x}\text{Ge}_x$ NWs.

In this chapter, we investigate the thermal conductivity of $\text{Si}_{1-x}\text{Ge}_x$ NWs with x (Ge content) changing from 0 to 1. The thermal conductivity calculated in this study is exclusively from the lattice vibration (phonon thermal conductivity), because phonons dominate the heat transport in SiNWs [138]. In our simulations, non-equilibrium molecular dynamics (NEMD) method is adapted to calculate the temperature distribution and thermal conductivity. To derive the force term, SW potential (Chap. 2.2) is used for Si and Ge.

3.2 Si/Ge Randomly Doped Nanowires

We study thermal conductivity of $\text{Si}_{1-x}\text{Ge}_x$ NWs along [100] direction with cross section of 3×3 unit cells (lattice constant is 0.543 nm) which corresponds to a cross section area of 2.65 nm^2 . The atomic structure is initially constructed from diamond structured bulk silicon. Then Si atoms are randomly substituted by Ge atoms in the nanowire. The resultant nanowire structure is relaxed to its closest minimum total energy. The two ends of nanowires are put into heat bathes with temperature T_L and T_R for the left and right end, respectively. Both Langevin and Nosé-Hoover heat bathes are used to ensure our results are independent of heat bath. All results given in this chapter are obtained by averaging about 1×10^8 time steps, with a time step of 0.8 fs. Free boundary condition is used to atoms on the outer surface of the nanowires. Thermal conductivity is calculated from the Fourier law, $\kappa = -J_L/\nabla T$, where J_L is the local heat current along the longitudinal direction, and ∇T is the temperature gradient.

The MD calculated temperature T_{MD} is corrected by taking into account the quantum effects of phonon occupation, using the relation [113]

$$3Nk_B T_{MD} = \int_0^{\omega_D} d\omega D(\omega) n(\omega, T) \hbar \omega, \quad (3.1)$$

where T is the real temperature and T_{MD} is the MD temperature, ω is the phonon frequency, $D(\omega)$ is the density of states, $n(\omega, T)$ is the phonon occupation number given by the Bose-Einstein distribution, and ω_D is the Debye frequency (Debye temperature of Si is 658 K [123]). Correspondingly, according to the Fourier Law, the final effective thermal conductivity is rescaled by

$$\kappa = \kappa_{MD} \frac{|\nabla T_{MD}|}{|\nabla T|} = \kappa_{MD} \frac{\partial T_{MD}}{\partial T}. \quad (3.2)$$

Using this approach, we perform a quantum correction to temperature and calculate the rescale rate $\alpha = \partial T_{MD} / \partial T$ for SiNWs. When T_{MD} is at room temperature, the rescale rate $\alpha = 0.91$ for silicon, which gives a quite small quantum correction effect on thermal conductivity. Moreover, in our following study, we fix the simulation temperature at room temperature, and mainly focus on the compositional dependence of thermal conductivity. Therefore, in the following part, we will no longer consider the quantum correction to MD temperature and thermal conductivity.

We study thermal conductivity of $\text{Si}_{1-x}\text{Ge}_x$ NWs with Ge atoms randomly distributed ($0 \leq x \leq 1$). In our simulations, the nanowire has a length of 20 unit cells which corresponds to 10.86 nm. For each Ge content x , in order to reduce the fluctuation, the results are averaged over 20 realizations. In Fig. 3.1 we plot κ/κ_0 versus Ge content x at room temperature. Here κ is the thermal conductivity of $\text{Si}_{1-x}\text{Ge}_x$ NWs, and κ_0 is the corresponding thermal conductivity of pure SiNWs. The lowest κ is only 18% (Langevin) and 15% (Nosé-Hoover) of that of pure SiNWs. We also did the calculation with nanowire length of 10 unit cells in the longitudinal direction. The lowest thermal conductivity is 17% of that pure SiNWs, which demonstrates that the composition dependence of thermal conductivity is a general characteristic for $\text{Si}_{1-x}\text{Ge}_x$ NWs. It is quite interesting that with only 5% Ge atoms ($\text{Si}_{0.95}\text{Ge}_{0.05}$ NWs), thermal conductivity of SiNWs can be reduced 50%. The best fitting gives rise to

$$\kappa = A_1 e^{-x/B_1} + A_2 e^{-(1-x)/B_2} + C, \quad (3.3)$$

where A_1 , B_1 , A_2 , B_2 and C are fitting parameters. As shown in Tab. 3.1, the decaying rates B_1 and B_2 by Nosé-Hoover heat bath coincide with those by

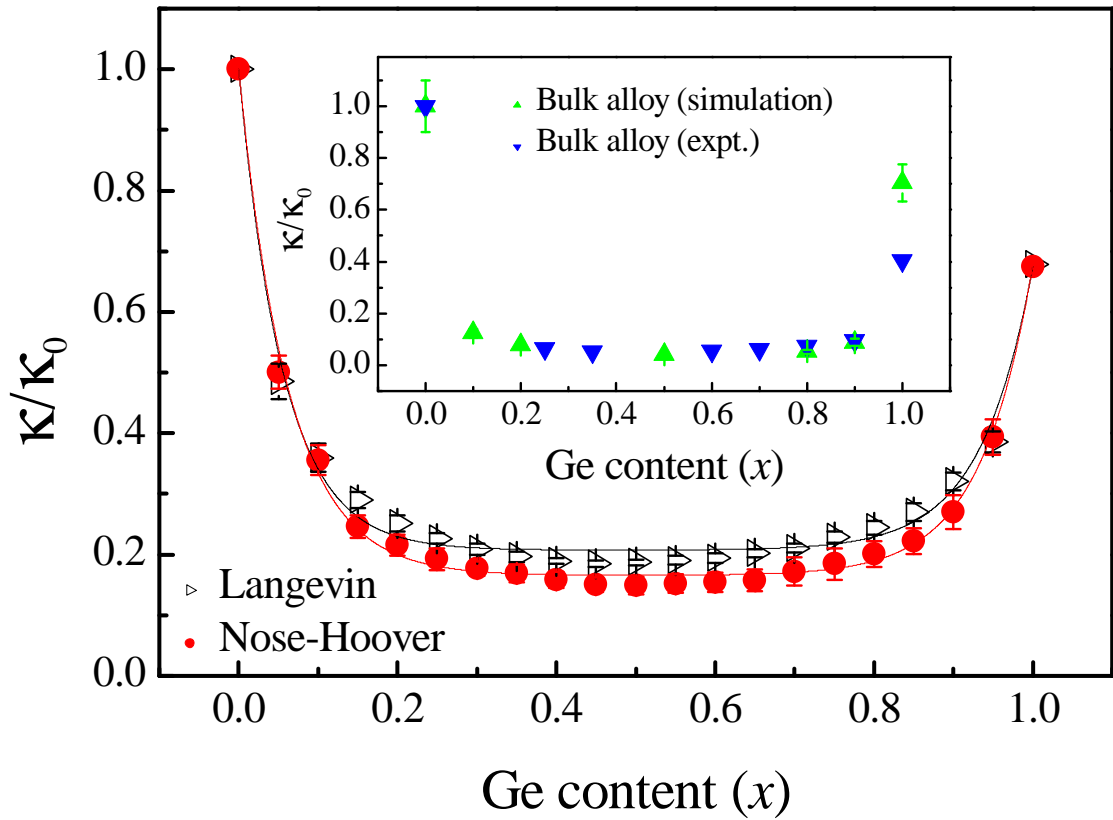


Figure 3.1: Normalized thermal conductivity of $\text{Si}_{1-x}\text{Ge}_x$ NWs versus Ge content x at 300 K. Thermal conductivity of SiNWs at the same temperature is used as the normalization reference. The inset shows simulation results from Ref. [139] and experimental results from Ref. [140] for Si-Ge bulk alloy.

Table 3.1: The fitting parameters of thermal conductivity for both Langevin and Nosé-Hoover heat bathes. The best fitting formula is $\kappa = A_1 e^{-x/B_1} + A_2 e^{-(1-x)/B_2} + C$.

Heat bath	A_1	B_1	A_2	B_2	C
Langevin	2.50	0.056	1.47	0.065	0.65
Nosé-Hoover	2.01	0.063	1.23	0.066	0.40

Langevin heat bath, meaning that the low thermal conductivity of $\text{Si}_{0.95}\text{Ge}_{0.05}$ NWs is independent of the heat bath used. We also show the simulation [139] and experimental [140] results for bulk $\text{Si}_{1-x}\text{Ge}_x$ alloy in the inset of Fig. 3.1. Although thermal conductivity of SiNWs is about two orders of magnitude smaller than that of bulk Si, the dependence of κ on the Ge atom content is similar.

In order to study the physical mechanism for the reduction of thermal conductivity, we have calculated the participation ratio defined in Eq. (2.64), which is an important measure for the fraction of phonons participating in thermal transport. It can effectively indicate the localization of phonon modes with $O(1)$ for delocalized modes and $O(1/N)$ for localized modes. To study the overall phonon localization effect in a given structure, we have further calculated the averaged phonon participation ratio (P_{ave}) defined as

$$P_{ave} = \sum_{\omega} P(\omega) DOS(\omega), \quad (3.4)$$

where $DOS(\omega)$ is the density of states of phonons. Fig. 3.2 shows the averaged phonon participation ratio versus Ge content x , which shows a consistent trend with the variation of thermal conductivity in Fig. 3.1. In both SiNWs and GeNWs,

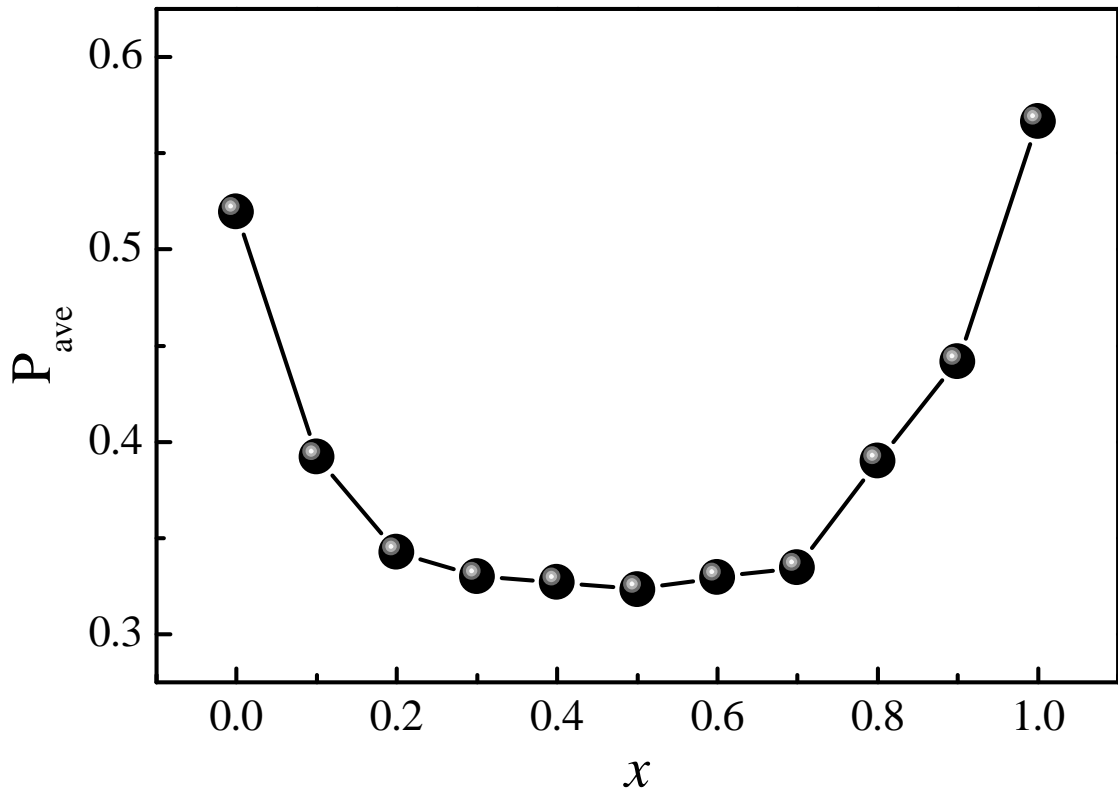


Figure 3.2: Averaged phonon participation ratio P_{ave} versus Ge content x in $\text{Si}_{1-x}\text{Ge}_x$ NWs.

a relatively high P_{ave} appears, which indicates the delocalized characteristics of phonon modes and corresponds to high thermal conductivity. However, in $\text{Si}_{1-x}\text{Ge}_x$ NWs ($0 \leq x \leq 1$), with the impurity concentration increasing, P_{ave} decreases significantly, which indicates the strong localization effect induced by the impurity scattering and corresponds to low thermal conductivity.

3.3 Si/Ge Superlattice Nanowires

We now turn to the reduction of thermal conductivity by using superlattice structure. Some experimental and theoretical works [141–143] have been carried out to study the effects of interface and superlattice (SL) period on thermal conductivity of various kinds of superlattice structures. Here we study the thermal conductivity of SL structured Si/Ge NWs. Fig. 3.3 shows the schematic picture for Si/Ge superlattice nanowires. In our simulations, the SL NWs consist of alternating Si and Ge layers with changeable period length in the longitudinal direction. It has a fixed cross section of 3×3 unit cells and a fixed length of 10 unit cells in the longitudinal direction. Si/Ge SL structured NWs may have three different contacts with heat bathes: both heat bathes are chosen to be Si; both are Ge; and one is Si, the other one is Ge, as the same material adjacent to the heat bath, respectively.

Fig. 3.4 shows the thermal conductivity κ of the SL NWs versus the period length for these three contacts. Langevin heat bath is used here. Thermal conductivity calculated from different NW-heat bath contacts has a good agreement with each other, suggesting that κ has weak dependence on the detailed heat bath contact. As shown in Fig. 3.4, κ of Si/Ge SL NWs decreases monotonically with the period length decreasing from 4.43 nm (32 layers), until period length reaches a critical value of 1.11 nm (8 layers). At this critical period length, κ of Si/Ge SL NWs is only one sixth of that of pure SiNWs. This reduction of thermal conductivity is due to the fact that when decreasing the period length of SL structured NWs with a fixed total length, the increasing number of interface will lead to an

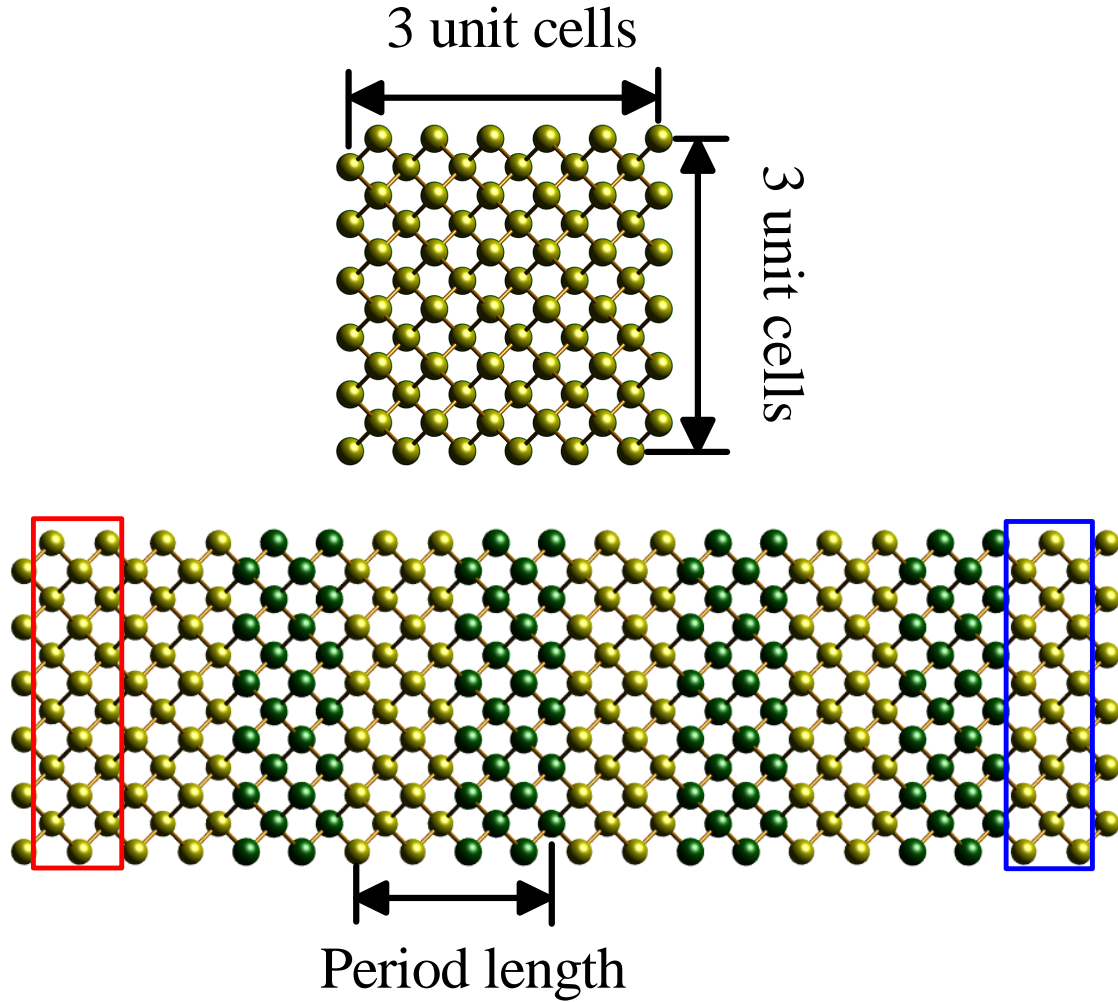


Figure 3.3: **Schematic picture for Si/Ge superlattice nanowires.** The yellow and green circles denote Si and Ge atoms, respectively. The top panel shows the cross sectional view of the superlattice nanowires (3×3 unit cells). The bottom panel shows the side view of the superlattice nanowires with a period length of 8 atomic layers. The total length of the superlattice nanowire is 10 unit cells. The red and blue boxes draw the heat bath regions with high and low temperature, respectively.

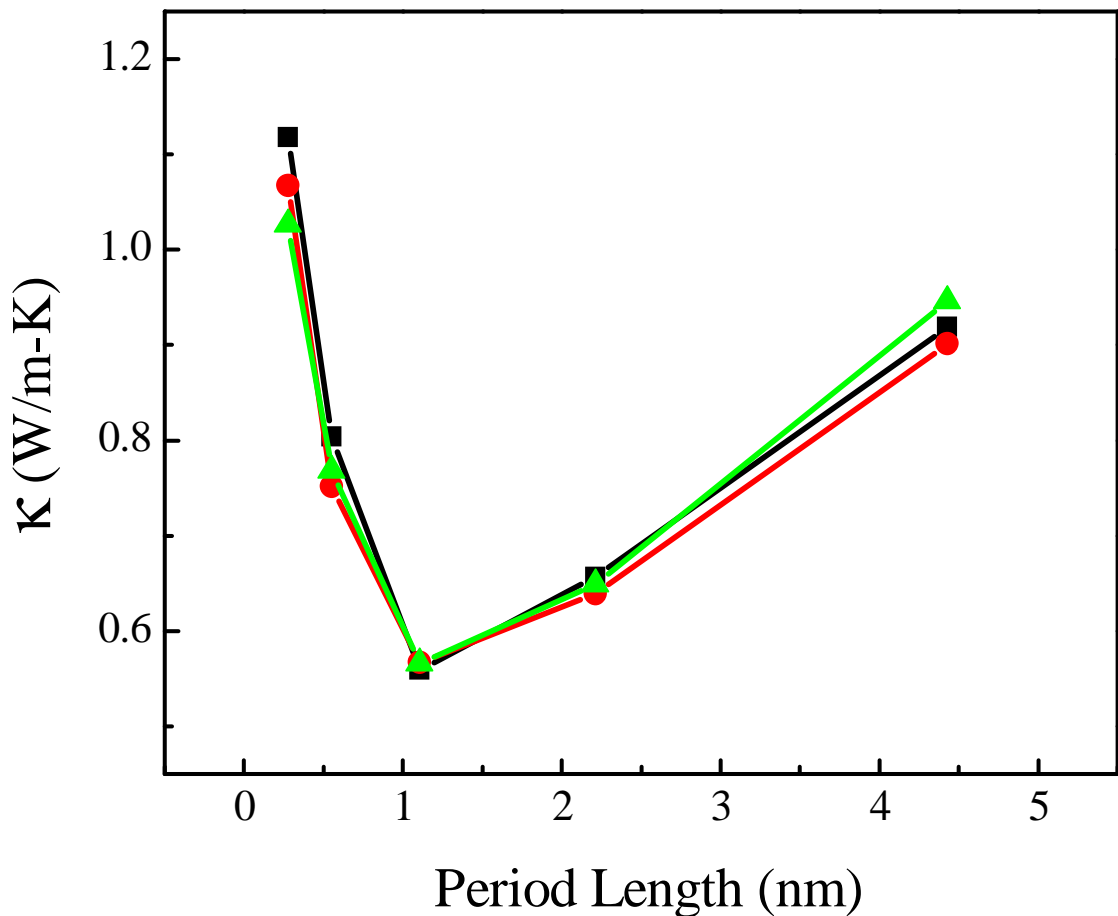


Figure 3.4: **Thermal conductivity κ of Si/Ge superlattice NWs versus period length at 300 K.** Here the atoms in heat baths are: both are Si (black squares), both are Ge (red circles), and atom in one heat bath is Si, in the other one is Ge, as the same material adjacent to the heat bath (green triangles).

enhanced interface scattering, which is responsible for the reduction of κ . As period length decreases further from the critical value, there exists a rapid increase in κ . At room temperature, the dominant phonon wavelength of SiNWs is about 1~2 nm [144], which is quite close to the critical value of 1.11 nm in the present study. When period length is smaller than the dominant phonon wavelength, ballistic transport dominates as phonons can propagate ballistically, which gives rise to a rapid increase in thermal conductivity [145, 146].

In order to get a better understanding of the underlying mechanism of the period length dependence of thermal conductivity, we calculate the power spectrum of both Si and Ge layers of SL structured NWs with different period length. The power spectrum is calculated by the Fourier transform of the atom's velocity autocorrelation function. Fig. 3.5a and 3.5b show the normalized power spectrum in two typical cases: SL structured NWs with period length of 1.11 nm (8 layers), and SL structured NWs with period length of 0.28 nm (2 layers). It is clearly that there exists a larger overlap of power spectrum in the case which has a larger thermal conductivity. It is well understood that in low dimensional systems, a large overlap of power spectrum means that heat current can easily go through the system and, therefore, results in a high thermal conductivity [147, 148]. In order to quantify the above power spectrum analysis, the overlap of the power spectra (S) are calculated as [148]

$$S = \frac{\int_0^\infty d\omega P_{Si}(\omega)P_{Ge}(\omega)}{\int_0^\infty d\omega P_{Si}(\omega) \int_0^\infty d\omega P_{Ge}(\omega)}, \quad (3.5)$$

where $P_{Si}(\omega)$ and $P_{Ge}(\omega)$ denote the power spectrum of Si and Ge atom, respectively. In Fig. 3.6, we plot the overlap ratio S versus period length. A comparison between Fig. 3.4 and 3.6 reveals that a larger overlap S corresponds to a higher κ .

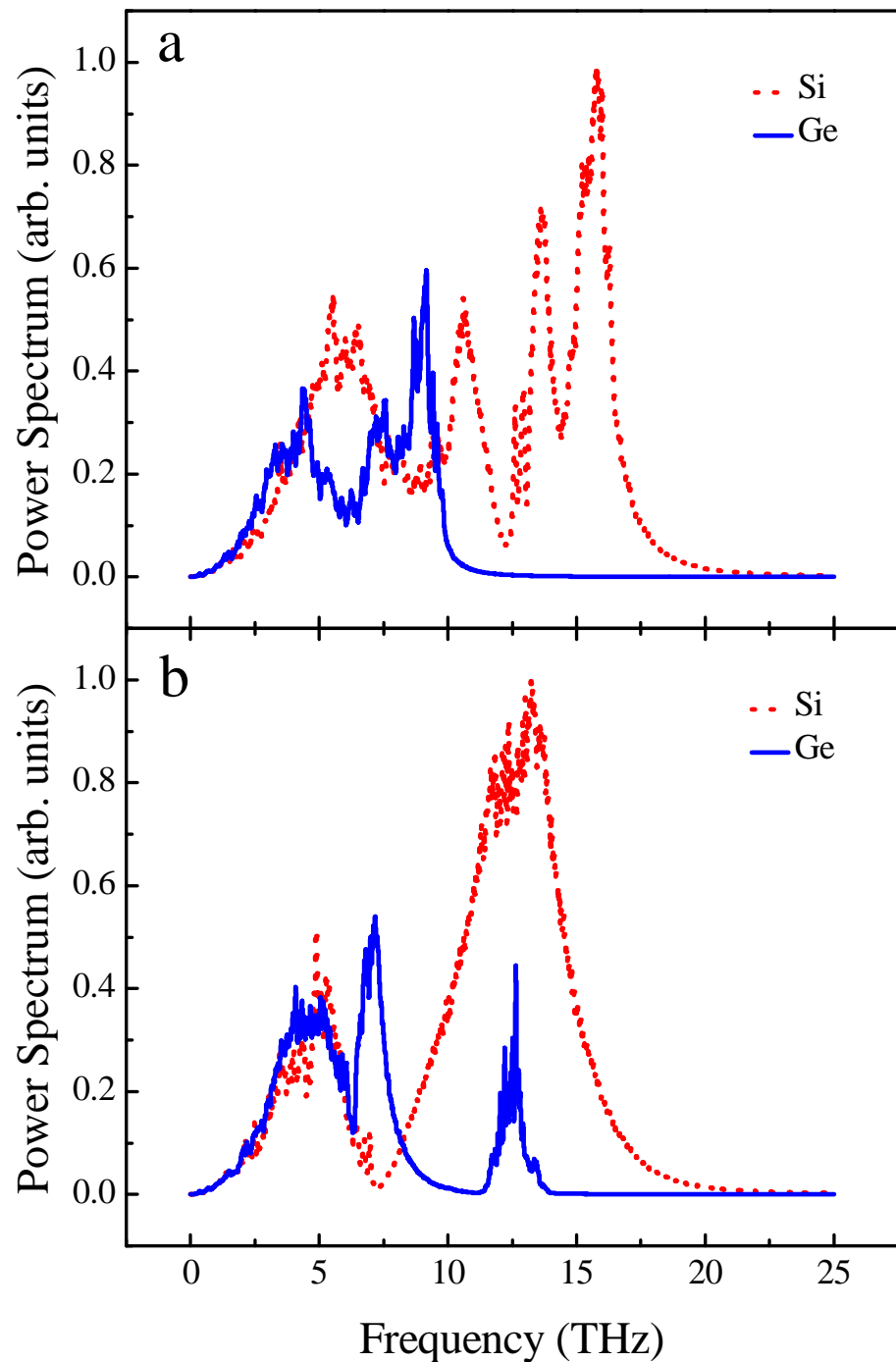


Figure 3.5: **Normalized power spectrum of different atoms in Si/Ge superlattice NWs.** a Period length is 1.11 nm (8 layers). b Period length is 0.28 nm (2 layers).

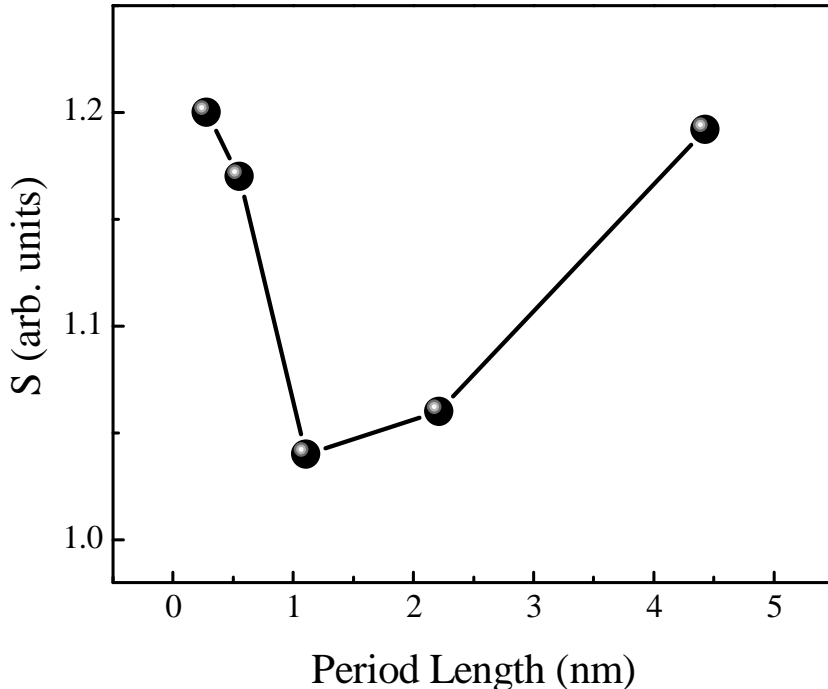


Figure 3.6: Overlap ratio of power spectrum S versus period length.

3.4 Summary

In this chapter, we have investigated the composition dependence of thermal conductivity of $\text{Si}_{1-x}\text{Ge}_x$ NWs with x changing from 0 to 1. A remarkable composition effect on thermal conductivity is observed. With only 5% Ge atoms, thermal conductivity of SiNWs can be reduced 50%. This composition dependence of thermal conductivity is explained by phonon participation ratio. In addition, we have also investigated the thermal conductivity of Si/Ge superlattice NWs. The dependence of thermal conductivity on the period length is explained by the overlap of phonon power spectrum. The low thermal conductivity of $\text{Si}_{1-x}\text{Ge}_x$ NW can significantly enhance its thermoelectric figure of merit and has raised the exciting prospect for application in on-chip cooler.

Chapter 4

Remarkable Reduction of Thermal Conductivity in Si Nanotubes

In this chapter, we propose to reduce thermal conductivity of silicon nanowires (SiNWs) by introducing small hole at the center, i.e., construct silicon nanotube (SiNT) structures. Our numerical results demonstrate that a very small hole (only 1% reduction of cross section area) can induce a 35% reduction of room temperature thermal conductivity. Moreover, with the same cross sectional area, thermal conductivity of SiNT is only about 33% of that of SiNW at room temperature. The spatial distribution of vibrational energy reveals that localization modes are concentrated on the inner- and outer-surface of SiNTs. The enhanced surface-to-volume ratio in SiNTs reduces the percentage of delocalized modes, which is believed to be responsible for the reduction of thermal conductivity. Our study suggests SiNT is a promising thermoelectric material with low thermal conductivity.

4.1 Motivation

Thermoelectric (TE) materials can provide electricity when subjected to a temperature gradient, or provide cooling performance when electrical current passing through it. They have the advantages of lightweight, environmentally benign and without moving parts. The efficiency of TE materials can be characterized by the dimensionless thermoelectric figure of merit ZT given by Eq. (1.5). As a result, materials with low thermal conductivity are highly desirable in order to achieve high ZT . Recently, experimental [44, 45] and theoretical [134, 149, 150] efforts have demonstrated high thermoelectric performance of silicon nanowires (SiNWs), due to the low thermal conductivity observed in this low-dimensional material [55].

Thermal conductivity of nanoscale materials is quite different from that of bulk materials. For instance, due to the high surface-to-volume ratio (SVR) and the boundary scattering, thermal conductivity of SiNWs is about 2 orders of magnitude smaller than that of bulk crystal [55, 151]. The low thermal conductivity of SiNWs is of particular interest for thermoelectric application. To further reduce the thermal conductivity, it has been suggested that random scattering of phonon is an efficient approach to reduce thermal conductivity [81, 146] and increase thermoelectric ZT correspondingly [138]. In addition to the random scattering of phonon, the surface scattering is another way to reduce thermal conductivity. It has been shown that surface roughness can decrease the phonon mean free path and consequently reduce thermal conductivity [152].

In this chapter, we propose to further reduce thermal conductivity of SiNWs obviously by introducing more surface scattering: make SiNWs hollow to create inner surface, i.e., construct silicon nanotubes (SiNTs).

4.2 Thermal Conductivity of Si Nanotubes

Equilibrium molecular dynamics (EMD) simulations have the advantage over non-equilibrium molecular dynamics simulations that an infinitely long system can be studied with periodic boundary condition when the simulation domain is long enough. In addition, no temperature gradient is involved in EMD simulations. In this chapter, we use EMD simulations to study thermal conductivity of SiNTs and SiNWs along [100] with different cross sectional area.

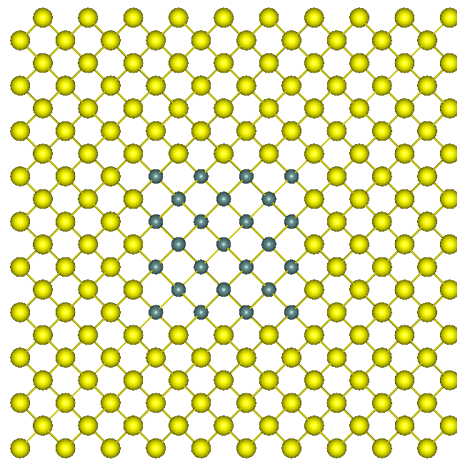


Figure 4.1: **A typical cross sectional view of SiNTs with $L_y = L_z = 3$ and $N_Y = N_Z = 5$.** The central atoms in green denote the removed atoms.

We set longitudinal direction along x axis, and atoms in the same layers means they have the same x coordinate. The atomic structure of the nanowire is initially constructed from diamond structured bulk silicon, with N_X , N_Y , N_Z unit cells in x , y and z direction, respectively. Then some central atoms in SiNWs are removed to create the SiNTs structures. The cross section of the hollow region is rectangular. The center of the rectangle is located near the geometric center of the nanowire and the size is controlled by two parameters L_y and L_z , which means

there are $(2L_y+1)$ and $(2L_z+1)$ layers of silicon atoms are removed away in y and z direction, respectively.

Fig. 4.1 shows a typical cross sectional view of SiNTs with $L_y=L_z=3$ and $N_Y=N_Z=5$. Here the SiNWs used to construct the SiNTs have a cross section area of 7.37 nm^2 ($N_Y=N_Z=5$). The cross section area of SiNTs is defined as the cross section area of SiNWs minus the cross section area of the removed central region. With adjustable L_y and L_z (from 1 to 6), the cross section area of SiNTs varies from 4.72 nm^2 to 7.30 nm^2 .

In our simulations, SW potential (Chap. 2.2) is used to derive the force term. Numerically, velocity Verlet algorithm (Chap. 2.3) is employed to integrate Newton's equations of motion, and each MD step is set as 0.8 fs. Since quantum effect on thermal conductivity of SiNWs is quite small at room temperature [81], we do not adapt quantum correction in our study as we mainly concentrate on the geometric effect on thermal conductivity above room temperature.

In EMD simulations, thermal conductivity in longitudinal direction (along x axis) is calculated from Green-Kubo formula given by Eq. (2.31), and heat current is defined in Eq. (2.45). A cubic super cell of $N_X \times N_Y \times N_Z$ unit cells is used in our simulation. Periodic boundary condition is applied in x (longitudinal) direction. Free boundary condition is applied in other two directions, and to the atoms on the inner- and outer- surfaces of SiNTs and SiNWs. For each realization, all the atoms are initially placed at their equilibrium positions but have a random velocity according to Gaussian distribution. Canonical ensemble MD with Langevin heat reservoir first runs for 10^5 steps to equilibrate the whole system at a given temperature. Then micro-canonical ensemble MD runs for another 3×10^6 steps (2.4 ns) and heat current is recorded at each step. After that, thermal conductivity is

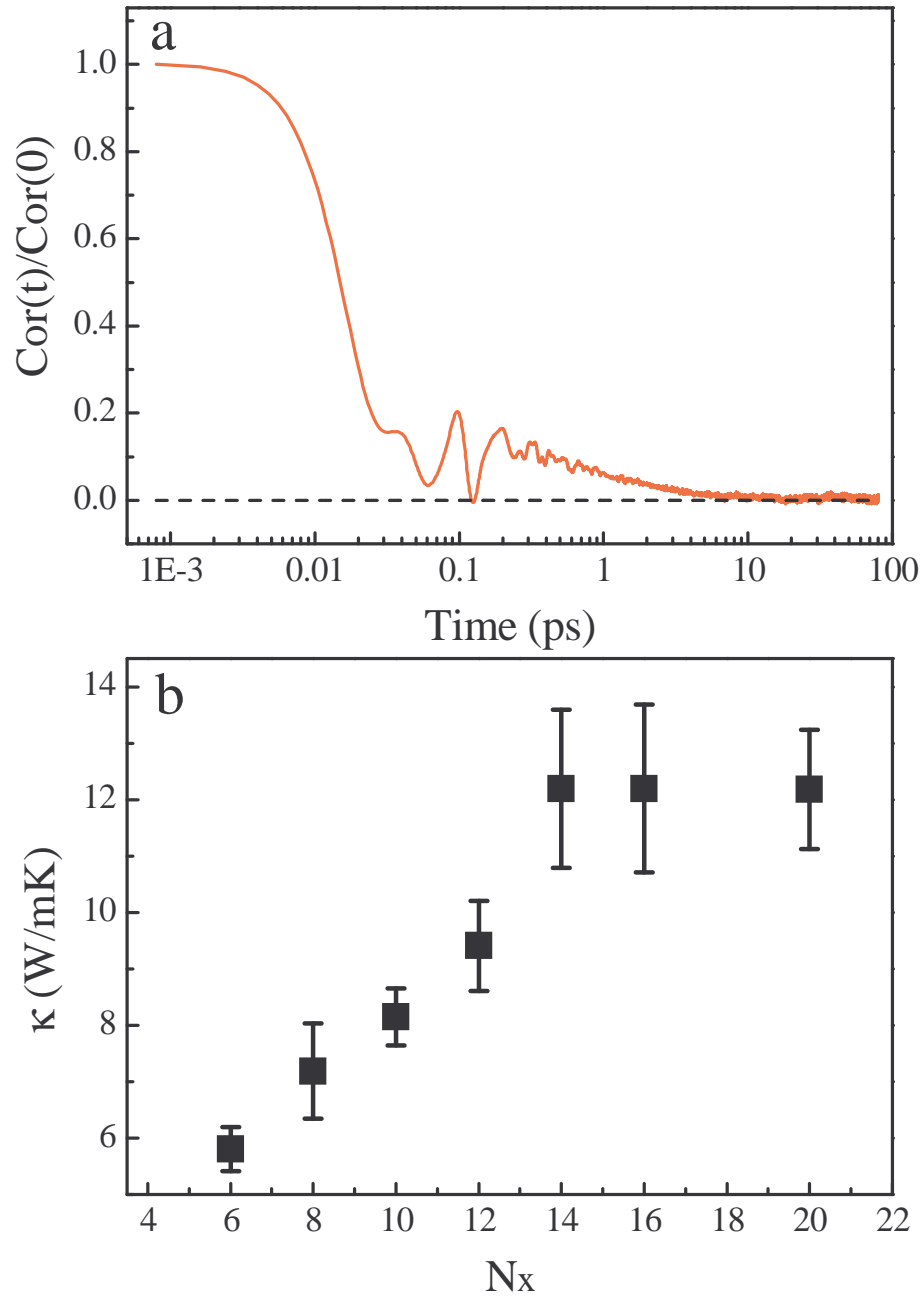


Figure 4.2: **Heat current autocorrelation function (HCACF) and thermal conductivity of SiNWs.** a Time dependence of normalized HCACF $Cor(t)/Cor(0)$ (solid line) for a typical realization in a $16 \times 5 \times 5$ super cell at 300 K. The dashed line draws the zero-axis for reference. b Thermal conductivity of SiNWs at 300 K versus super cell size N_x ($N_x \times 5 \times 5$ unit cells).

calculated according to Eq. (2.31). The final result is averaged over 6 realizations with different initial conditions.

Fig. 4.2a shows the time dependence of normalized heat current autocorrelation function (HCACF) for a typical realization in a $16 \times 5 \times 5$ super cell at 300 K (other realizations are similar). It shows a very rapid decay of HCACF at the beginning, followed by a long tail which has a much slower decay. This two-stage decaying characteristic of HCACF has been found in the study of various materials [111, 118, 121]. The rapid decay corresponds to the contribution from short wavelength phonons to thermal conductivity, while the slower decay corresponds to the contribution from long wavelength phonons [111, 121]. Furthermore, it is shown in Fig. 4.2a that HCACF decays to approximately zero within 100 ps, much shorter than the total simulation time of 2.4 ns. It has been checked that this is also true for the largest super cell size $N_X = 20$ considered in our study. Therefore, the total simulation time of 2.4 ns is adequate for the present study.

Using the direct integration method (Chap. 2.5) up to the cut-off time in EMD simulation, we calculate the thermal conductivity of SiNWs according to Eq. (2.34). Fig. 4.2b shows the calculated thermal conductivity of SiNWs with a fixed cross section of 5×5 unit cells versus super cell length N_X at 300 K. Due to the periodic boundary condition, finite size effect exists in the calculated thermal conductivity when simulation domain is small [111, 118]. In our simulations, the thermal conductivity of SiNWs saturates to a constant when the super cell size $N_X \geq 16$ unit cells, in agreement with the previous study [151]. Therefore, in the following part, we set $N_X = 16$ in the longitudinal direction and study the thermal conductivity of SiNWs and SiNTs with different cross section area.

Fig. 4.3 shows thermal conductivity of SiNWs and SiNTs versus cross section

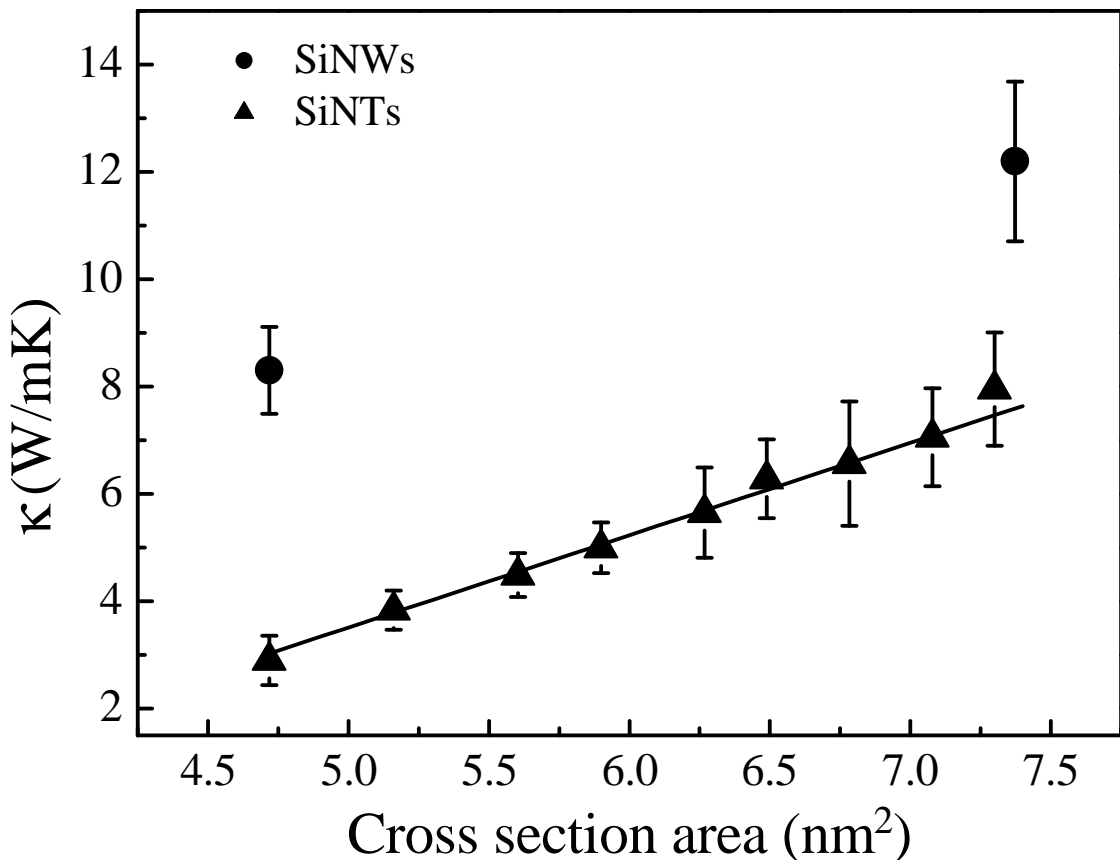


Figure 4.3: **Thermal conductivity of SiNWs and SiNTs versus cross section area at 300 K.** The circle and triangle denote SiNWs and SiNTs, respectively. The cross section areas for these two SiNWs are 7.37 nm^2 and 4.72 nm^2 , respectively. The solid line is drawn to guide the eyes.

area at 300 K. Here the cross section area of SiNT is defined as the area of corresponding SiNW minus the removed part. Even with a very small hole, $L_y = L_z = 1$, the thermal conductivity decreases obviously, from $\kappa_{NW} = 12.2 \pm 1.4$ W/mK to $\kappa_{NT} = 8.0 \pm 1.1$ W/mK. In this case, only a 1% reduction of cross section area (from 7.37 nm^2 to 7.30 nm^2) induces 35% reduction of thermal conductivity. Fig. 4.4 shows thermal conductivity of SiNWs (cross section area 7.37 nm^2) and SiNTs (cross section area 7.30 nm^2) at different temperature. Thermal conductivity of both SiNWs and SiNTs decreases with the increase of temperature, which is in general a consequence of the stronger anharmonic phonon-phonon scattering at higher temperature. Our results are in agreement with a recent study on the temperature dependent thermal conductivity of thin SiNWs [153]. In addition, when temperature increases, thermal conductivity of SiNWs decreases slightly faster than that of SiNTs does. This is because the creation of the hollow center results in more localized phonon modes in SiNTs. It has been demonstrated that the introduction of localization modes can weaken the temperature dependence of thermal conductivity [154], which is also recently observed in the crystalline-core/amorphous-shell SiNWs [153]. So the reduction percentage of thermal conductivity slightly decreases from 35% at 300 K to 29% at 1000 K. However, even at high temperature as 1000 K, the impact of small hole on thermal conductivity is still obvious, only 1% reduction of cross section area can induce 29% reduction of thermal conductivity.

In addition, with the increase of L_y and L_z , the cross sectional area decreases further, and a linear dependence of thermal conductivity on cross section area is observed, as shown in Fig. 4.3. We also show thermal conductivity of SiNWs with $N_Y = N_Z = 4$. It has the same cross section area (4.72 nm^2) as the SiNTs with $N_Y = N_Z = 5$ and $L_y = L_z = 6$. It is clear that for SiNWs, thermal conductivity

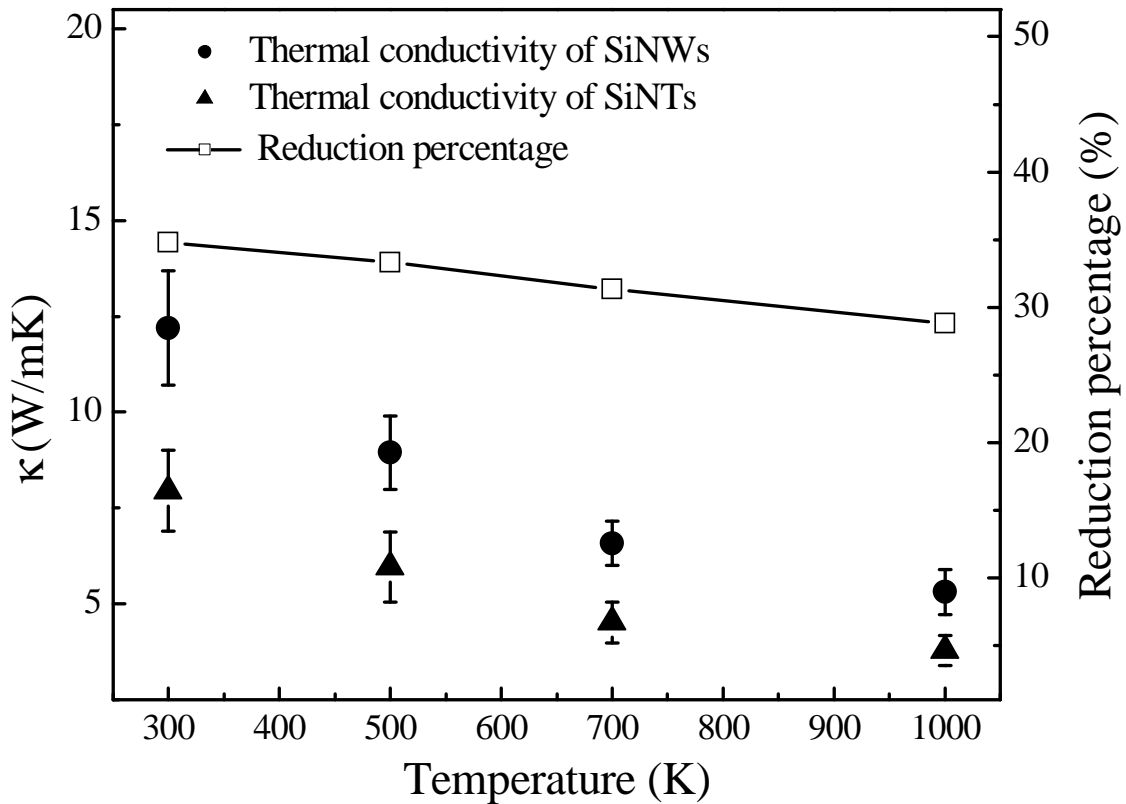


Figure 4.4: **Thermal conductivity of SiNWs and SiNTs versus temperature.** The circle and triangle denote SiNWs and SiNTs, respectively. The cross section areas for SiNWs and SiNTs are 7.37 nm^2 and 7.30 nm^2 , respectively. The square draws the reduction percentage of thermal conductivity from SiNWs to SiNTs.

increases with cross section area increases. This is because with the increase of size, more and more phonons are excited, which results in the increase of thermal conductivity. So the decrease of cross section area is one origin for the low thermal conductivity of SiNTs. However, it is not the sole one. We can see that with the same cross section area, thermal conductivity of SiNTs is only about 33% of that of SiNWs ($\kappa_{NW} = 8.8 \pm 1.1$ W/mK and $\kappa_{NT} = 2.9 \pm 0.5$ W/mK). In the following section, we will demonstrate this additional reduction is due to the localization of phonon modes on the surface.

4.3 Phonon Mode Analysis

Due to the inner surface in SiNTs which partially destroys the original periodicity of SiNWs, phonon localization takes place on the surface in general. To understand the underlying physical mechanism of thermal conductivity reduction in SiNTs, we carry out a vibrational eigen-mode analysis on SiNWs and SiNTs. Mode localization can be quantitatively characterized by the participation ratio defined in Eq. (2.64). Fig. 4.5 compares the participation ratio (p-ratio) of each eigen-mode for SiNWs and SiNTs with the same cross section area (4.72 nm^2). It shows a reduction of p-ratio in SiNTs for both low frequency phonons and high frequency phonons, compared with SiNWs. Most of the eigen-modes in SiNWs have p-ratio greater than 0.5, showing characteristic of delocalized mode, while majority of the eigen-modes in SiNTs have p-ratio less than 0.5, showing characteristic of localized mode.

Although participation ratio can effectively describe mode localization in a quantitative manner, it does not provide information about the spatial distribution

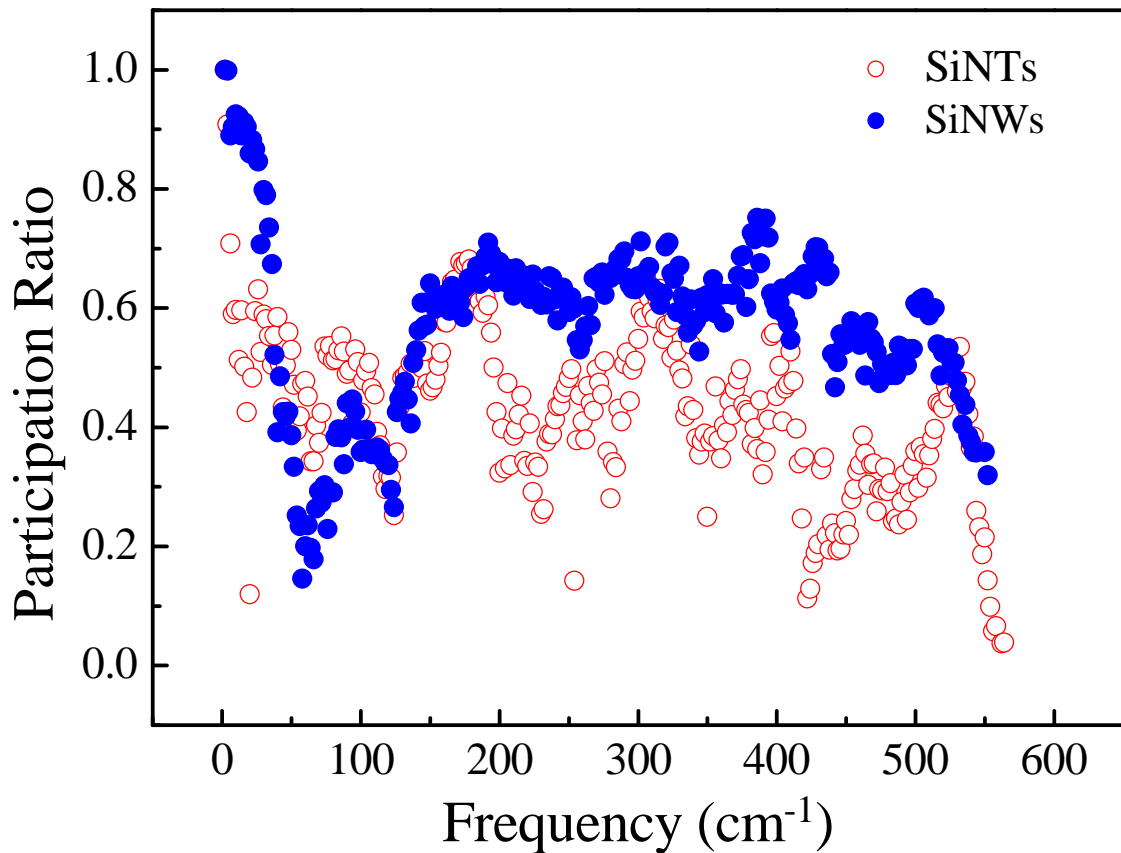


Figure 4.5: **Participation ratio of each eigen-mode for SiNTs and SiNWs with the same cross section area of 4.72 nm².** The hollow red circle and solid blue circle denote SiNTs and SiNWs, respectively.

of a specific mode. To get a better physical picture about the localization modes, we also provide the local vibrational density of states (LVDOS) which is defined as [130, 155]

$$D_i(\omega) = \sum_{\lambda} \sum_{\alpha} e_{i\alpha,\lambda}^* e_{i\alpha,\lambda} \delta(\omega - \omega_{\lambda}), \quad (4.1)$$

where i denotes the i th atom that corresponds to a specific spatial location. Based on LVDOS, we define the spatial distribution of energy as

$$\begin{aligned} E_i &= \sum_{\omega} \left(n + \frac{1}{2} \right) \hbar \omega D_i(\omega) \\ &= \sum_{\omega} \sum_{\lambda} \sum_{\alpha} \left(n + \frac{1}{2} \right) \hbar \omega e_{i\alpha,\lambda}^* e_{i\alpha,\lambda} \delta(\omega - \omega_{\lambda}) \end{aligned} \quad (4.2)$$

where n is the phonon occupation number given by the Bose-Einstein distribution.

Instead of looking at energy distribution for each mode, here we can obtain the total energy spatial distribution for specified phonon modes.

In order to observe the spatial localization which is caused by the localized modes, the summation of ω in Eq. (4.2) only includes those modes with a relatively small p-ratio (e.g., less than 0.2). Fig. 4.6 shows the normalized energy distribution on the cross section (YZ) plane of SiNWs and SiNTs at 300 K. The positions of the circles denote different locations on YZ plane. For those localized modes with p-ratio less than 0.2, it is clearly shown in Fig. 4.6a that the intensity of localized modes is almost zero in the center of the NW, while with finite value at the boundary. This demonstrates that the localization modes in SiNWs are distributed on the boundary (especially at the corner) of cross section plane, which corresponds to the outer surface of SiNWs. In addition, due to inner-surface introduced in SiNTs, energy localization also shows up around the hollow region as shown in Fig. 4.6b. These results provide direct numerical evidence that localization takes place on the surface region. Alternatively, we also study the energy distribution of

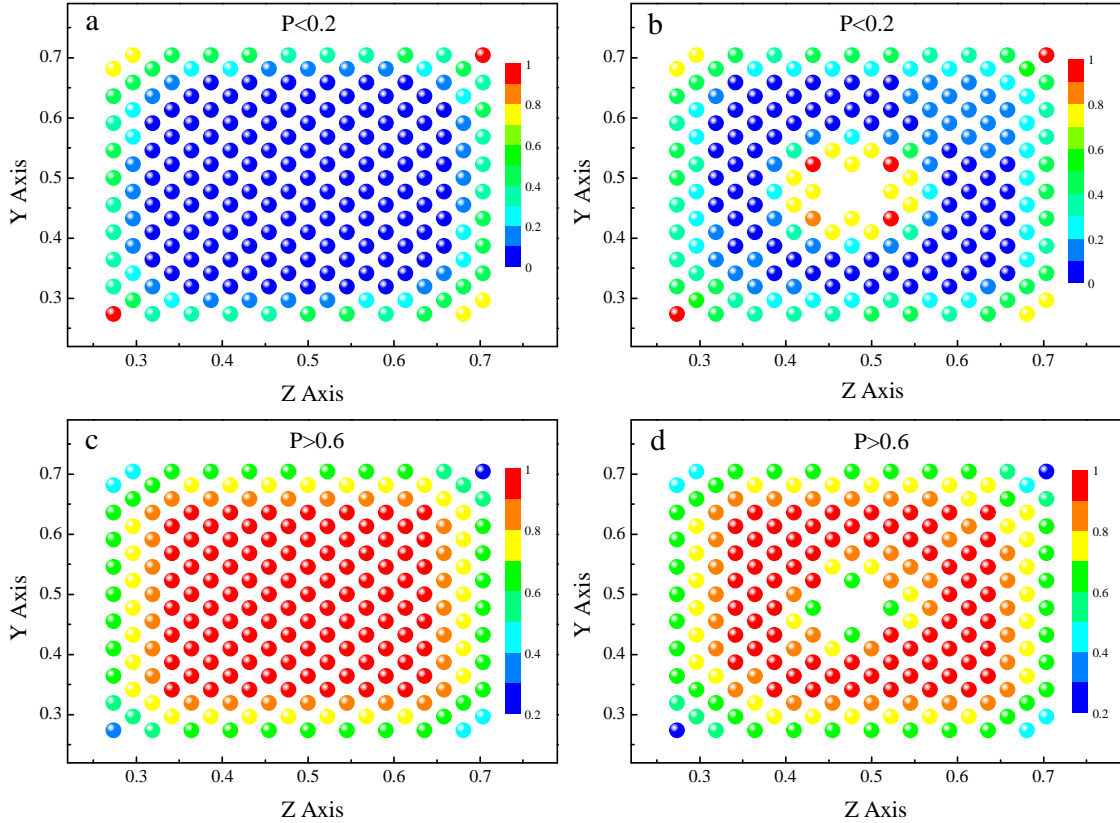


Figure 4.6: **Normalized energy distribution on the cross section (YZ) plane of SiNWs and SiNTs at 300 K.** Positions of the circles denote the different locations on YZ plane, and intensity of the energy is depicted according to the color bar. P in the figure denotes participation ratio. a Energy distribution for modes with $P < 0.2$ in SiNWs. b Energy distribution for modes with $P < 0.2$ in SiNTs. c Energy distribution for modes with $P > 0.6$ in SiNWs. d Energy distribution for modes with $P > 0.6$ in SiNTs.

delocalized modes with a relatively large p-ratio (e.g., greater than 0.6). For those delocalized modes with p-ratio greater than 0.6, majority of energy is distributed inside SiNWs and SiNTs as shown in Fig. 4.6c and 4.6d, except for the hollow region in SiNTs. Therefore, from the spatial distribution of delocalized modes, we can conclude that the localized modes reside on the boundary (surface) region.

Since SiNTs in our simulation are constructed from SiNWs but have hollow interior, the density is approximately the same for these two structures. For SiNWs and SiNTs with the same cross section area and same length, the volume is the same. Therefore, the total number of atoms, thus the total number of eigen-modes, is the same for SiNTs and SiNWs under this condition. Compared with SiNWs, SiNTs have a larger surface area, which corresponds to a higher SVR. As a result, there are more modes localized on the surface, which increases the percentage of the localized modes to the total number of modes. This explains the overall reduction of p-ratio in SiNTs compared with SiNWs as shown in Fig. 4.5. In heat transport, the contribution to thermal conductivity mainly comes from the delocalized modes rather than the localized modes. Due to the enhanced SVR in SiNTs which induces more localized modes, the percentage of delocalized modes decreases, leading to a reduction of thermal conductivity in SiNTs compared with SiNWs.

4.4 Summary

In this chapter, we have proposed to reduce thermal conductivity of SiNWs by introducing hollow interior at the center, i.e., construct SiNT structures. Molecular dynamics simulations results demonstrate that at room temperature with only a small hole of 0.07 nm^2 , (cross section area from 7.37 nm^2 to 7.30 nm^2), it can

reduce thermal conductivity from $\kappa_{NW} = 12.2 \text{ W/mK}$ to $\kappa_{NT} = 8.0 \text{ W/mK}$, which means a 1% reduction of cross section area induces a 35% reduction of thermal conductivity. Moreover, with the same cross sectional area, thermal conductivity of SiNTs is only about 33% of that of SiNWs at room temperature. Compared to SiNWs with the same cross sectional area, participation ratio in SiNTs decreases for both low frequency and high frequency phonons. The spatial distribution of energy reveals that localization takes place on the surface region in both SiNWs and SiNTs. The enhanced surface-to-volume ratio in SiNTs reduces the percentage of delocalized modes, and thus lowers the thermal conductivity. Very recently, the similar SiNT structures have been fabricated experimentally by reductive decomposition of a silicon precursor in an alumina template and etching [156]. Our results suggest that SiNT is a promising thermoelectric material by using reliable fabrication technology.

Chapter 5

Phonon Coherent Resonance in Core-Shell Nanowires

In this chapter, we study heat current autocorrelation function and thermal conductivity in core-shell nanowires by using molecular dynamics simulations. Interestingly, a remarkable oscillation effect in heat current autocorrelation function is observed in core-shell nanowires, while the same effect is absent in pure silicon nanowires, nanotube structures and randomly doped nanowires. Detailed characterizations of the oscillation signal reveal that this intriguing oscillation is caused by the coherent resonance effect of the transverse and longitudinal phonon modes. This phonon resonance results in the localization of the longitudinal modes, which leads to the reduction of thermal conductivity in core-shell nanowires. Our study reveals a coherent mechanism to tune thermal conductivity in core-shell nanowires by engineering phonon resonance.

5.1 Motivation

Thermoelectric materials with low thermal conductivity are favorable for high-efficiency thermoelectric applications in both power generation and refrigeration. In the past few years, there have been some significant progresses achieved [44, 45] to enhance thermoelectric performance of silicon, which is abundant in nature, well-engineered in semiconductor industry and friendly to the environment [157]. For example, by etching the surface of silicon nanowires (SiNWs), it has been demonstrated that thermal conductivity of bulk silicon can be reduced more than two orders of magnitude without affecting the electric power factor too much, resulting in a dramatically enhanced figure of merit (ZT) at room temperature [44]. Most of the conventional approaches to reduce thermal conductivity, such as introduction of rough surface [44, 45, 158] and impurity [81, 146] scatterings, are based mainly on incoherent mechanisms, which cause phonons to lose coherence and also deteriorate the electronic transport properties [44].

Recent experimental works [58, 59] have demonstrated that, by altering phonon band structure in periodic nanomesh structures, a remarkable enhancement in ZT can be achieved by significantly reducing thermal conductivity of silicon while preserving its electrical conductivity. These studies have offered new perspective to improve ZT based on coherent mechanisms. In this chapter, by using molecular dynamics simulations, we demonstrate in Ge/Si core-shell NWs an intriguing phonon coherent resonance phenomenon, which offers a coherent mechanism to tune thermal conductivity in core-shell NWs. As the Ge/Si core-shell NWs can be synthesized experimentally [159–161], our study suggests novel insights to the thermal management at nanoscale based on reliable fabrication technology.

5.2 Oscillation in Heat Current Autocorrelation Function

The configuration of [100] Ge/Si core-shell NWs is shown in Fig. 5.1. The cross sections of both core and shell regions are square, with L_c and L denoting the side length of core and shell regions, respectively. The longitudinal direction is set along x axis, with N_X , N_Y , N_Z unit cells (8 atoms per unit cell) in x , y and z direction, respectively. SW potential (Chap. 2.2) is used in our simulations to derive the force term. The velocity Verlet algorithm (Chap. 2.3) is employed to integrate Newton's equations of motion numerically, and time step is set as 0.8 fs.

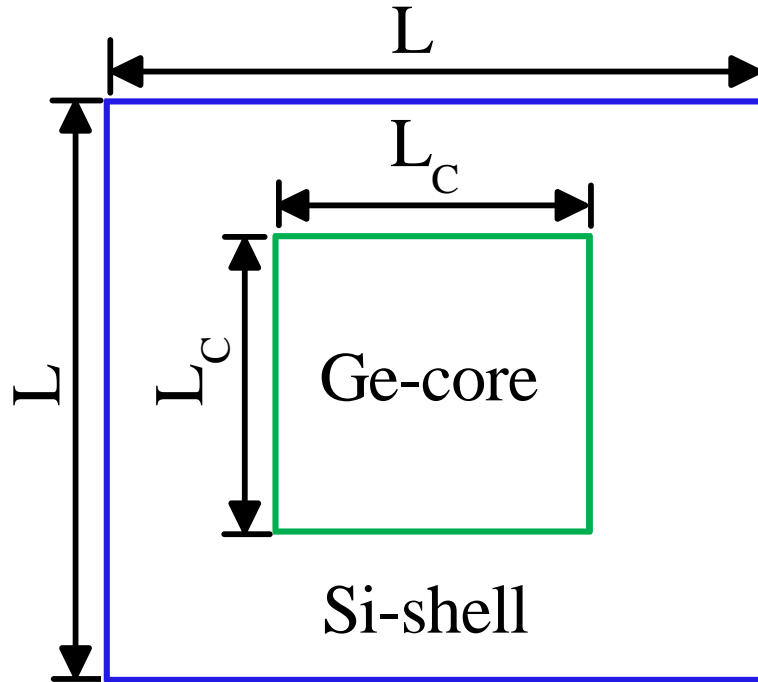


Figure 5.1: **Cross sectional view of [100] Ge/Si core-shell NWs.** The cross sections of both core and shell regions are square, with L_c and L denoting the side length of core and shell regions, respectively.

The coherence of phonons can be probed by the heat current autocorrelation function (HCACF) in equilibrium molecular dynamics (EMD) simulations. The canonical ensemble molecular dynamics simulations with Langevin heat reservoir first runs for 10^5 steps to equilibrate the heterostructure NWs at a given temperature, during which the free boundary condition is applied to all the atoms on the surface. The quality of this relaxation process is highlighted by the monotonic increase of the lattice constant of Ge/Si core-shell NWs when the core-shell ratio increases (Fig. 5.2).

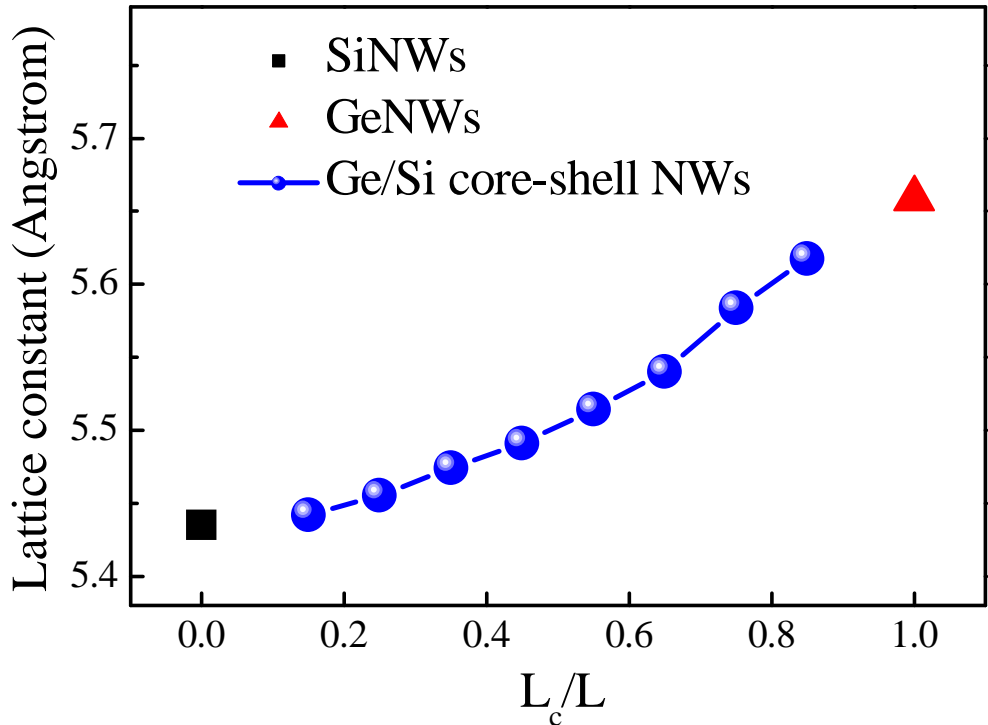


Figure 5.2: **Lattice constant of Ge/Si core-shell NWs (circle) versus core-shell ratio calculated after structure relaxation.** The lattice constant of SiNWs (square) and GeNWs (triangle) are also plotted for reference.

After structure relaxation, all atoms are assigned with a random velocity according to Gaussian distribution. The periodic boundary condition is applied in the x (longitudinal) direction, and the free boundary condition is applied in the other two directions. Then microcanonical ensemble EMD runs for 3×10^6 time steps (2.4 ns), and heat current given by Eq. (2.45) is recorded at each step. Finally, the heat current (in x direction) autocorrelation function is calculated according to Eq. (2.33). The whole procedure is repeated six times with different initial conditions of the velocity distribution.

Fig. 5.3a shows the typical time dependence of normalized HCACF in a $16 \times 5 \times 5$ super cell at 300 K for Ge/Si core-shell NWs with a given core-shell ratio ($L_c/L=0.65$). For comparison, the HCACF for SiNWs and silicon nanotubes (SiNTs) [158] are also shown in Fig. 5.3. For both SiNWs and SiNTs, there is a very rapid decay of HCACF at the beginning, followed by a long-time tail with a much slower decay. This two-stage decaying characteristic of HCACF has been reported in the studies of various single-component materials [111, 121, 162]. When time is long enough, the long-time tail of HCACF decays to approximately zero.

However, an obvious oscillation up to a very long time appears in HCACF for core-shell NWs (Fig. 5.3a). The long-time region of HCACF reveals that this oscillation is not random but shows a periodic manner (Fig. 5.3b). This has been further checked by extending the total number of time steps in microcanonical ensemble EMD simulations, from $N = 3 \times 10^6$ to $N = 5 \times 10^6$. We find that EMD simulations with even longer simulation time give almost identical result to that shown in Fig. 5.3, and the periodic oscillation feature is not affected at all. By using the same EMD simulation procedure, we have also calculated HCACF for $\text{Si}_{1-x}\text{Ge}_x$ randomly doped NWs with different doping concentration x . As shown

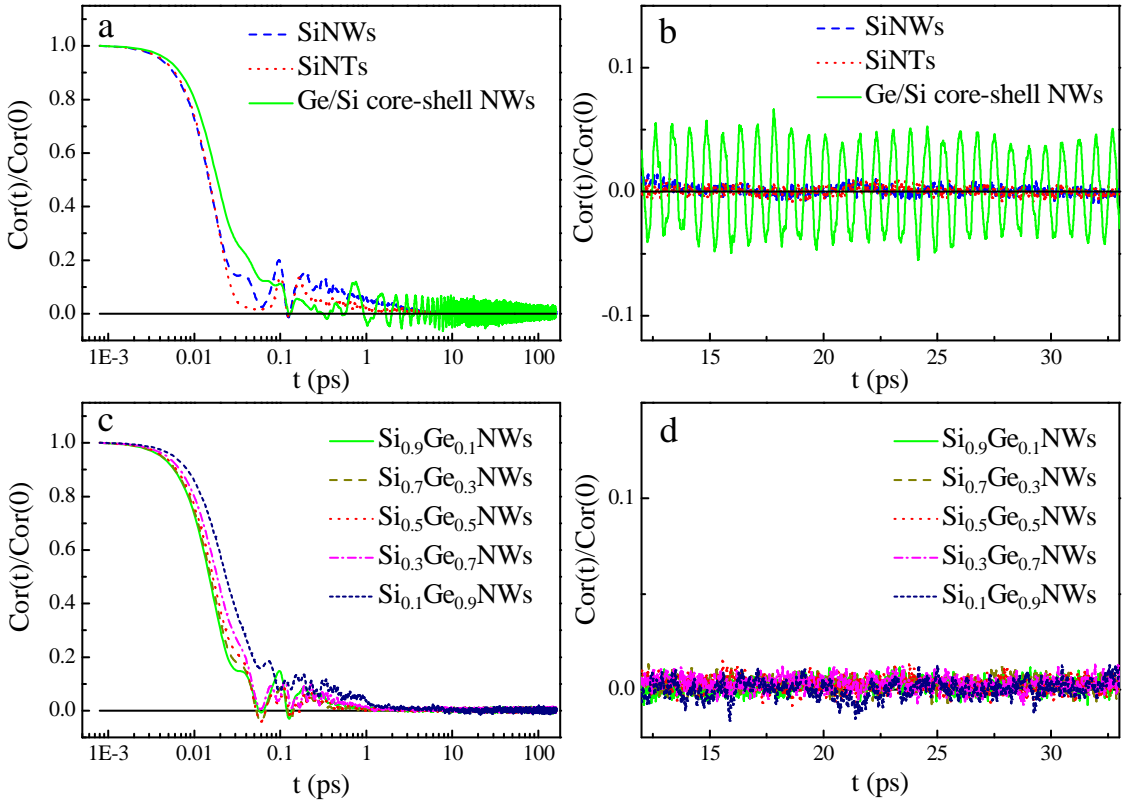


Figure 5.3: **Time dependence of normalized heat current autocorrelation function (HCACF).** a HCACF for SiNWs (blue dash line), SiNTs (red dot line) and Ge/Si core-shell NWs with $L_c/L=0.65$ (green solid line). b Long-time region of HCACF shown in a. c HCACF for $\text{Si}_{1-x}\text{Ge}_x$ NWs with different doping concentration x . d Long-time region of HCACF shown in c. The black lines in all figures draw the zero axis for reference. Here the super cell size is $16 \times 5 \times 5$ and temperature is 300 K.

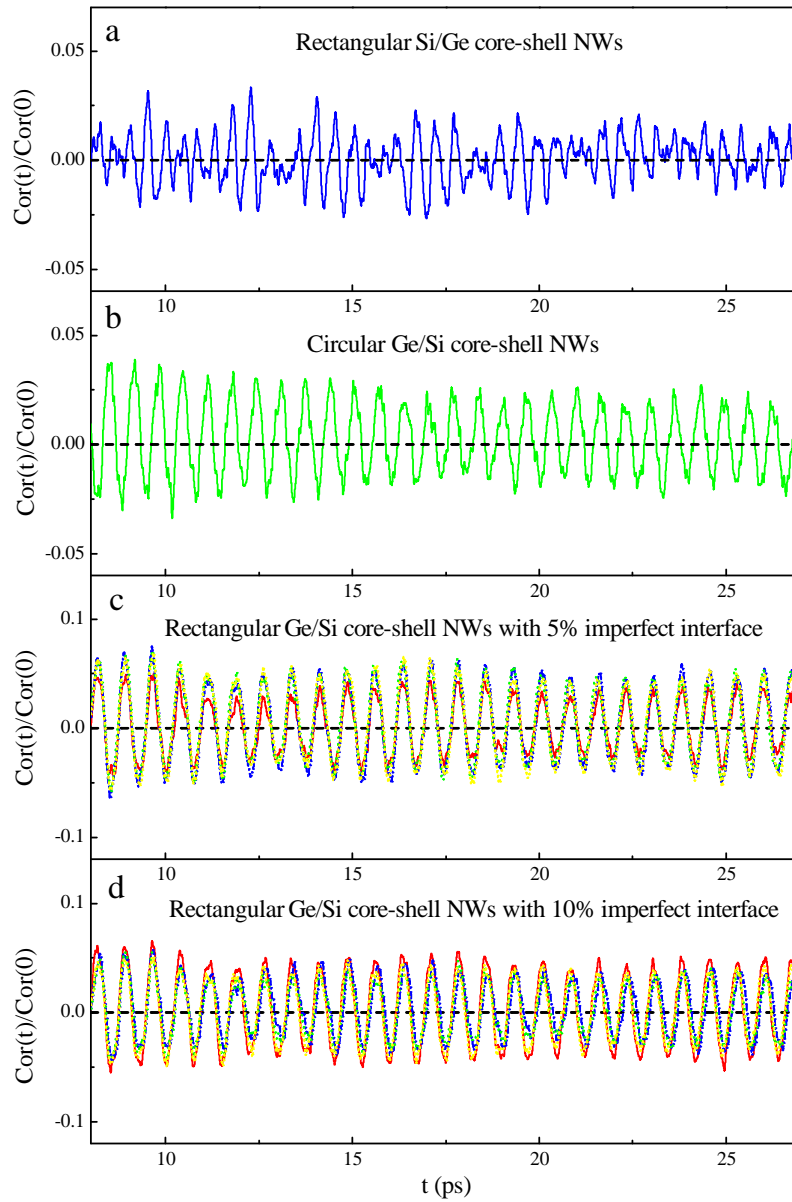


Figure 5.4: Long-time region of normalized HCACF for different core-shell NWs. a Rectangular Si/Ge core-shell NWs (blue line). b Circular Ge/Si core-shell NWs (green line). c Rectangular Ge/Si core-shell NWs with 5% of the atoms at the interface randomly switched. d Rectangular Ge/Si core-shell NWs with 10% of the atoms at the interface randomly switched. Different colors in c and d denote different realizations for the random switch. The black dashed lines in all figures draw the zero axis for reference.

in Fig. 5.3c and 5.3d, none of the $\text{Si}_{1-x}\text{Ge}_x$ NWs exhibit any oscillation in HCACF, consistent with the theoretical idea that the periodic oscillation is a coherent wave effect that requires long-time correlation, which should not take place in a randomly doped heterostructure.

It is worth pointing out that oscillation in HCACF has been reported by Landry et al. [163] in the study of superlattice structures. They found the oscillation in their work is caused by specific zero-wave-vector optical phonon modes and can be removed when a different definition of the heat current based on the equilibrium atom positions is used [163]. In this work, we have also calculated the heat current according to the definition based on equilibrium atom positions. In contrast, we found the oscillation in HCACF still exists. Furthermore, to verify the generality of this oscillation feature of HCACF in core-shell structure, we have also considered the following cases: rectangular Si/Ge core-shell NWs, circular Ge/Si core-shell NWs (both core and shell regions are circular), and rectangular Ge/Si core-shell with imperfect interface (e.g., 5% and 10% of the atoms at the interface are randomly switched). As shown in Fig. 5.4, oscillations in HCACF still exist in these cases, suggesting that it is a generic characteristic in core-shell structures. For the sake of simplicity for theoretical modeling and analysis, all the Ge/Si core-shell NWs considered in the rest of this study are rectangular cross sections as depicted in Fig. 5.1.

Fig. 5.5a and 5.5b shows the long-time region of normalized HCACF for Ge/Si core-shell NWs with different core-shell ratio at 300 K. This oscillation effect exhibits an obvious structure dependence: when the core-shell ratio increases, it becomes stronger, reaches its maximum amplitude at $L_c/L=0.65$, and then decreases. Moreover, for a given core-shell structure, the oscillation amplitude is

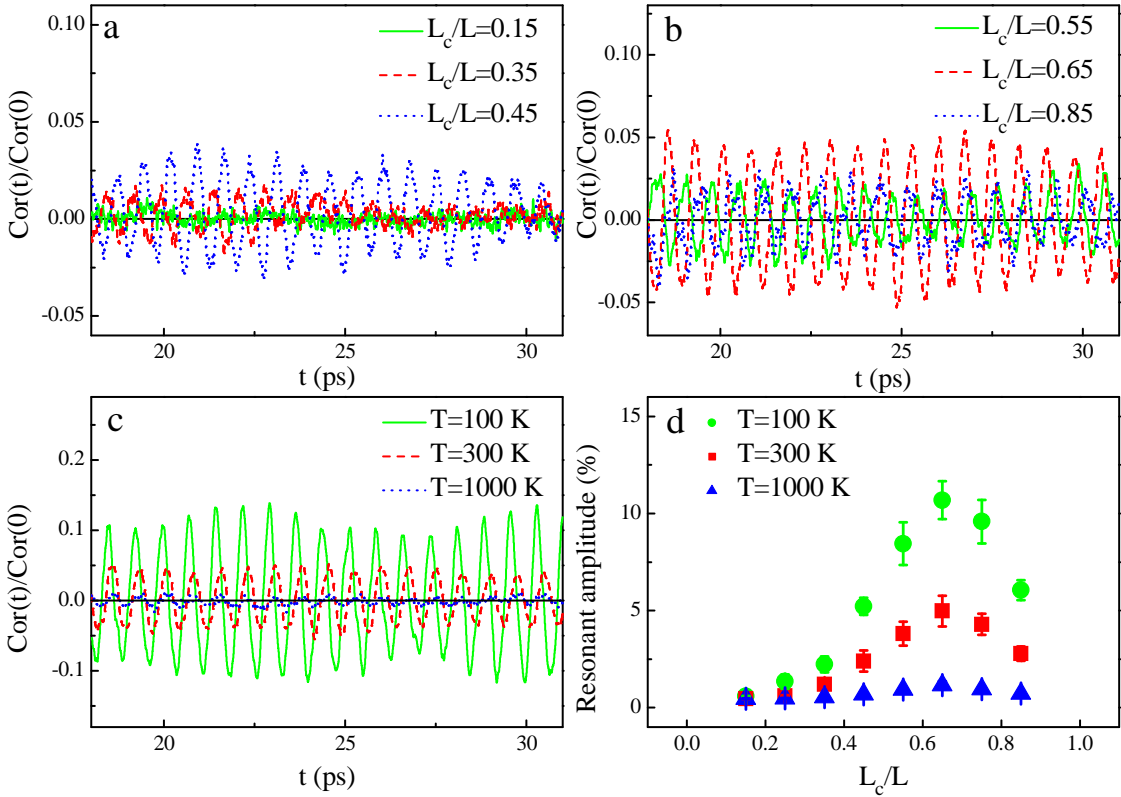


Figure 5.5: Structure and temperature dependence of the oscillation effect in Ge/Si core-shell NWs. Here we show the long-time region of normalized HCACF in a $16 \times 5 \times 5$ super cell. The black lines draw the zero axis for reference. a $L_c/L=0.15$ (green solid line), $L_c/L=0.35$ (red dash line) and $L_c/L=0.45$ (blue dot line) at 300 K. b $L_c/L=0.55$ (green solid line), $L_c/L=0.65$ (red dash line) and $L_c/L=0.85$ (blue dot line) at 300 K. c $L_c/L=0.65$ at 100 K (green solid line), 300 K (red dash line) and 1000 K (blue dot line). d Oscillation amplitude versus core-shell ratio L_c/L at 100 K (green circle), 300 K (red square) and 1000 K (blue triangle).

temperature-dependent and becomes larger at lower temperature (Fig. 5.5c). The structure and temperature dependence of the oscillation in HCACF suggests that there exists a coherent mechanism in core-shell NWs which can cause phonons to have the long-lasting correlation in such heterostructure.

To quantitatively characterize the oscillation effect in core-shell NW, we numerically measure the oscillation amplitude. Consider a perfect cosine oscillation function described by $u = A \cos(\omega t + \varphi)$, the standard deviation (σ) of this cosine function in the time interval $(t_1, t_1 + \Delta t)$ is given by

$$\sigma^2 = \frac{1}{\Delta t} \int_{t_1}^{t_1 + \Delta t} A^2 \cos^2(\omega t + \varphi) dt = \frac{A^2}{2}, \quad (5.1)$$

provided that Δt is integer times of the period. So the amplitude of a periodic oscillation can be measured by calculating the standard deviation ($A = \sqrt{2}\sigma$). For the random noise, the standard deviation is indeed a good quantity to gauge the noise level. Here we calculate the standard deviation of the long-time region of HCACF from t_d to $t_d + \Delta t$, where t_d is the time after HCACF (or the envelope of HCACF for oscillation case) decays to approximately zero (e.g., $t_d=15$ ps in Fig. 5.3b), and Δt is set as 15 ps during which the oscillation amplitude is almost constant. For each core-shell structure, the final results are averaged over six measurements of different realizations of HCACF.

For example, for those realizations of HCACF shown in Fig. 5.3b, the standard deviation of HCACF for Ge/Si core-shell NWs calculated from 15 ps to 30 ps is $\sigma=0.031$, and the calculated amplitude is $A = \sqrt{2}\sigma=0.044$, consistent with the oscillation amplitude shown in Fig. 5.3b. For SiNWs, the calculated standard deviation is about $\sigma=0.003$, and its corresponding amplitude is $A=0.0042$, which gives an estimation of the noise level and is one order of magnitude smaller

than the amplitude of the nontrivial oscillation in Ge/Si core-shell NWs. This method to measure oscillation amplitude can give distinct estimations of the non-trivial oscillation and the noise level. Fig. 5.5d shows the calculation results of the structure- and temperature-dependent oscillation amplitude. With core-shell ratio increases, the oscillation amplitude first increases, reaches a peak value at $L_c/L=0.65$ and then decreases. More interestingly, the oscillation amplitude at different temperature shows the same structure dependence, with larger amplitude at low temperature and vanishing amplitude (comparable to noise level) at high temperature.

To better understand the underlying mechanism, we have carried out extensive spectrum analysis by using the fast Fourier transform (FFT). We calculate the FFT of the long-time region of normalized HCACF from time t_d to $t_d + \Delta t$, with Δt set as 15 ps. It has been further checked that our FFT analysis is robust with the particular choice of t_d . Fig. 5.6 shows the FFT of normalized HCACF for different structures shown in Fig. 5.3b. The FFT amplitude for Ge/Si core-shell NWs exhibits a dominant peak at low frequency, which is denoted as f_0 in Fig. 5.6a. All the FFT amplitudes shown in Fig. 5.6 are normalized by the amplitude of the dominant resonant peak f_0 . Moreover, there exist multiple high frequency peaks shown in Fig. 5.6b, with much smaller amplitude compared to that of the dominant peak. The FFT spectrum of SiNWs (Fig. 5.6c) and SiNTs (Fig. 5.6d) looks completely different from that of Ge/Si core-shell NWs: there is no dominant peak over the entire frequency regime, and the FFT amplitude is more than two orders of magnitude smaller than the dominant peak amplitude for Ge/Si core-shell NWs. These two aspects are the typical characteristics of the noise spectrum. This spectrum analysis verifies that there is no significant oscillation in HCACF

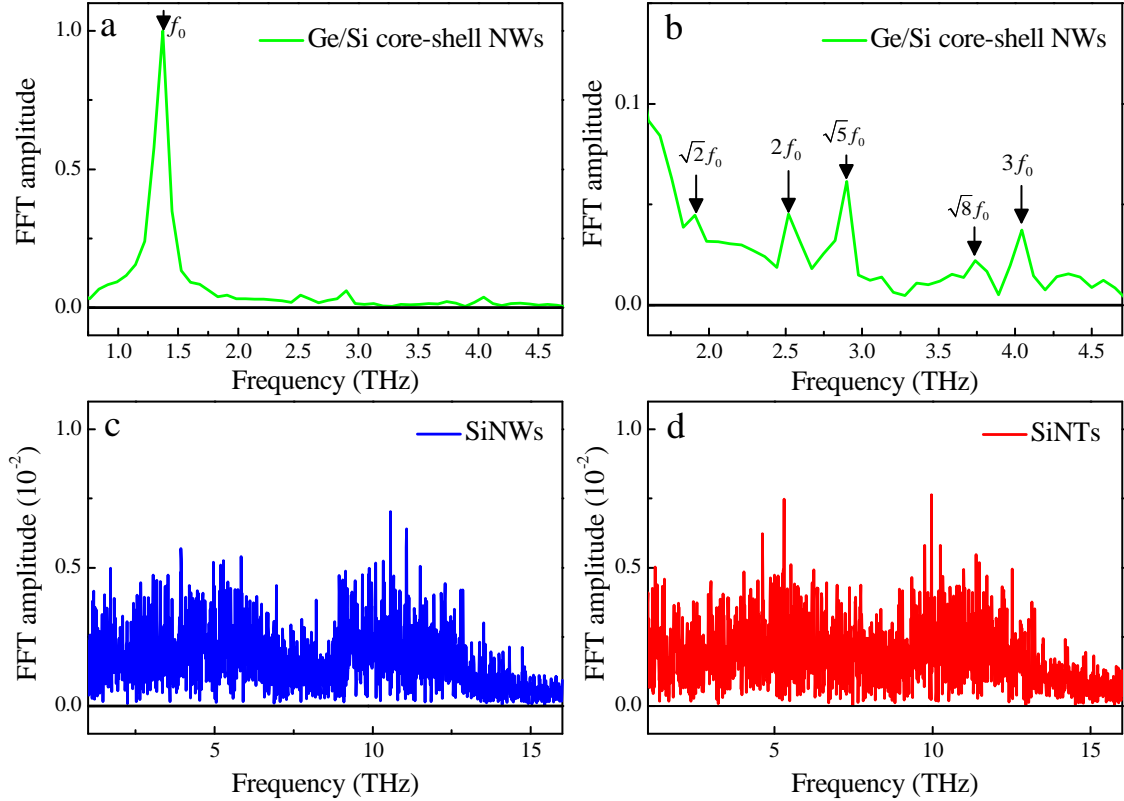


Figure 5.6: Amplitude of the fast Fourier transform (FFT) of the long-time region of normalized HCACF. The black lines in all figures draw the zero axis for reference. a Ge/Si core-shell NWs. b The high frequency oscillation peaks for Ge/Si core-shell NWs. The black arrows pinpoint the different oscillation frequencies. c and d are amplitudes of the FFT of the long-time region of normalized HCACF for SiNWs and SiNTs, respectively.

for SiNWs and SiNTs, and the fluctuation of HCACF in the long-time region for SiNWs and SiNTs is mainly due to the computational noise.

The multiple oscillation peaks observed in frequency domain for core-shell NWs are very similar to the confinement effect of the acoustic wave (coherent long wavelength phonon) in a confined structure. For a wire with the square cross section and side length L , the eigen-frequency of the transverse modes in such confined structure calculated from the elastic medium theory is given by:

$$f_{mn} = \frac{\omega_{mn}}{2\pi} = \frac{k_{mn}C}{2\pi} = \frac{C}{2\pi} \sqrt{\left(\frac{m\pi}{L}\right)^2 + \left(\frac{n\pi}{L}\right)^2} = \frac{C}{2L} \sqrt{m^2 + n^2} = \sqrt{m^2 + n^2} f_0, \quad (5.2)$$

where f_{mn} is the eigen-frequency specified by two integer number m and n , C is the speed of sound, and $f_0 = C/2L$ is the lowest eigen-frequency. We record the high frequency peaks marked by the black arrows in Fig. 5.6b, and compare them with the frequency of the dominant peak f_0 in Fig. 5.6a. We find the relation between the high frequency peaks and the dominant peak f_0 is very close to that given by Eq. (5.2). This good agreement of oscillation frequency suggests that the intriguing oscillation effect results from the frequency quantization of the transverse modes as a consequence of structure confinement in the transverse direction.

5.3 Coupling Picture

In single-component homogeneous NWs, atoms on the same cross section plane have the same sound velocity, so that the transverse motion is decoupled with the longitudinal motion. This is the reason that the oscillation signal is not probed by HCACF along the longitudinal direction in SiNWs. In core-shell NWs, atoms on the same cross section plane have different sound velocity in the longitudinal

direction. As a result, atoms near the core-shell interface are stretched due to the different sound velocity. This induces a strong coupling/interaction between the transverse and longitudinal motions. It is well known that when there is interaction between two modes, the oscillation amplitude will be maximized when the frequencies of these two modes are close to each other (resonance). Due to the frequency quantization of the transverse modes, resonance will take place when the frequency of the longitudinal mode is close to the eigen-frequency of the transverse mode, giving rise to the enhanced oscillation amplitude. This coupling picture explains that frequency quantization of the transverse modes can indeed manifest itself in HCACF along the longitudinal direction in Ge/Si core-shell NWs, while the same effect is absent in SiNWs, NTs and randomly doped NWs. Moreover, as the resonance effect of acoustic wave is a coherent process that requires long-time correlation, the stronger anharmonic phonon-phonon scattering at high temperature causes phonon to lose coherence, and leads to the vanishing of the oscillation effect at high temperature.

To quantitatively characterize the coupling between the transverse and longitudinal modes in core-shell structure, we consider the following two scenarios. For a core-shell structure consists of two homogeneous mediums A (core) and B (shell), if there is no coupling between A and B at the interface, the speed of sound C in this inhomogeneous medium (A/B core-shell) is either $C_{core} = C_A$ in medium A, or $C_{shell} = C_B$ in medium B, depending on the position. This is the scenario without the interface coupling. However, due to the coupling at the interface between A and B, the speed of sound in this inhomogeneous medium is different from that of its pure element, and can be effectively described by another homogeneous medium

E with the same elastic properties. This is the spirit of the effective medium approximation (EMA) and the actual case (with coupling). Since the mode coupling in core-shell structure is induced by the mismatch of sound velocity, we propose to define the coupling strength S in core-shell structure to be the difference between these two scenarios (with and without coupling) as:

$$S = \frac{N_{core} (C_{core} - C_{eff})^2 + N_{shell} (C_{shell} - C_{eff})^2}{N}, \quad (5.3)$$

where N is the total number of atoms in core-shell structure, N_{core}/N_{shell} is the number of atoms in the core/shell region, C_{eff} is the effective speed of sound in core-shell structure, and C_{core}/C_{shell} denotes the speed of sound in pure core/shell medium. According to this definition, the coupling strength is zero for pure SiNWs, consistent with the result that there is no resonance effect in SiNWs.

The speed of sound in pure Si and Ge NWs, and effective speed of sound in Ge/Si core-shell NWs are calculated by using GULP [128]. Bulk modulus K , Shear modulus G and mass density ρ of each structure are calculated by GULP after structure relaxation. Then the speed of sound is calculated according to $C = \sqrt{(K + \frac{4}{3}G)/\rho}$. As shown in Fig. 5.7, the dependence of coupling strength on core-shell ratio agrees qualitatively well with the variation of the measured oscillation amplitude shown in Fig. 5.5d. This good agreement reveals that the structure dependence of the oscillation amplitude is caused by the structure-dependent coupling strength.

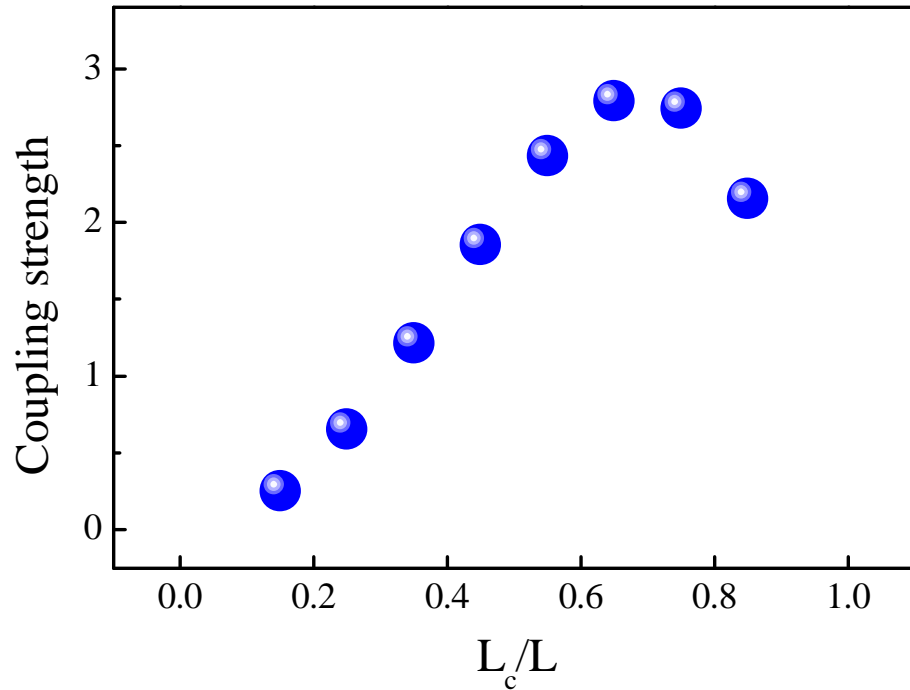


Figure 5.7: Coupling strength versus core-shell ratio in Ge/Si core-shell NWs.

5.4 Coherent Mechanism to Tune Thermal Conductivity

Due to the nonpropagating nature of the transverse modes, the resonance effect induced by coupling between the transverse and longitudinal modes can hinder the longitudinal transport [164], thus offering a coherent mechanism to tune thermal conductivity in core-shell structure based on resonance. To illustrate this coherent mechanism in more details, we study the localization effect of the longitudinal phonon modes in SiNWs and Ge/Si core-shell NWs. All phonon modes are computed by using GULP with a cross section of 5×5 unit cells. Mode localization can be quantitatively characterized by the phonon participation ratio

defined in Eq. (2.64) for each phonon mode.

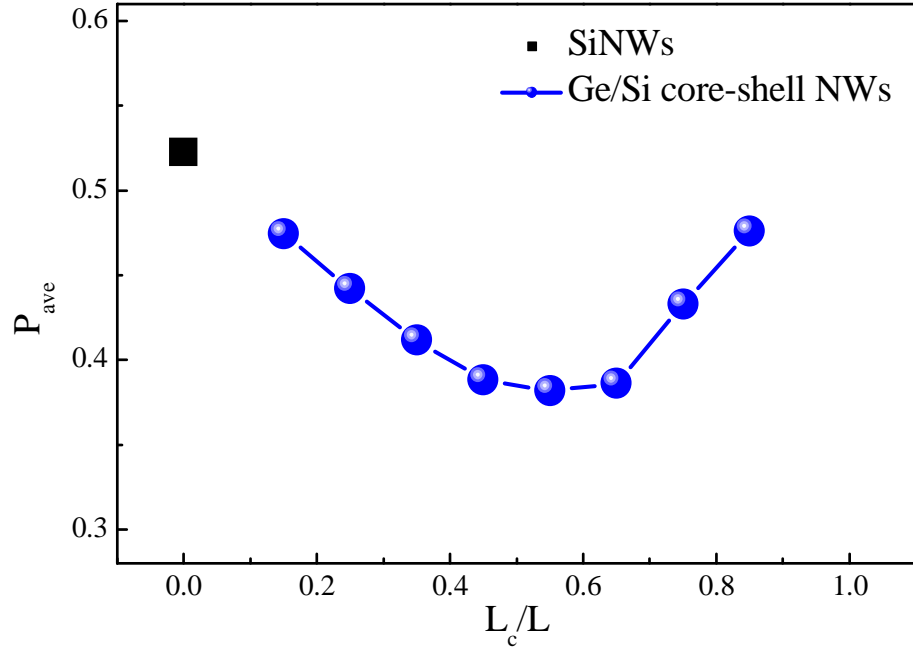


Figure 5.8: **Averaged phonon participation ratio P_{ave} versus core-shell ratio in Ge/Si core-shell NWs (circle).** The square plots P_{ave} in SiNWs with the same cross section area for comparison. All phonon modes are computed with a cross section of 5×5 unit cells.

When considering the overall influence of structure change on localization effect, averaged phonon participation ratio P_{ave} defined in Eq. (3.4) is a very useful quantity to characterize the overall localization effect, with a smaller P_{ave} indicating a stronger phonon localization effect [81]. Compared to SiNWs, P_{ave} in Ge/Si core-shell NWs shows an overall reduction (Fig. 5.8). More interestingly, P_{ave} in Ge/Si core-shell NWs shows a non-monotonic variation with the increase of core-shell ratio. This is difficult to be understood from the conventional diffusive phonon picture, which suggests that the interface scattering becomes stronger with

the increase of interface [165]. Our coupling picture can give a qualitatively good understanding of such non-monotonic variation: the resonance effect induced by coupling between the transverse and longitudinal phonon modes causes localization effect of the longitudinal phonon modes, and the strength of the localization effect P_{ave} is controlled by the coupling strength S , with a smaller P_{ave} at larger S .

To know how much the phonon localization effect can affect the thermal transport, we further study thermal conductivity κ of Ge/Si core-shell NWs. We should point out that when applying the Green-Kubo method to calculate thermal conductivity, it is a challenge to accurately specify the converged values of HCACF integral [166]. Because of the oscillation in HCACF observed in our calculations, it is even more challenging to specify the converged value of the HCACF integral for core-shell NWs. Thus we use non-equilibrium molecular dynamics (NEMD) simulations with Langevin heat reservoir to predict the thermal conductivity. In NEMD calculation of thermal conductivity of bulk material, the calculation results will depend on the size of the simulation cell if there are not enough phonon modes to accurately describe the phonon transport process. In this situation, extrapolation procedure must be applied to NEMD results with multiple system sizes. However, as demonstrated by Sellan *et al.* [166], the commonly used linear extrapolation procedure is not always accurate in Stillinger-Weber silicon. Moreover, in this chapter, our concern is the relative reduction of thermal conductivity in core-shell NWs, rather than its absolute value. Thus thermal conductivity of the single-component NWs with the same cross section area and length is used as the reference.

NEMD simulations are performed long enough (4×10^7 time steps) to ensure the non-equilibrium steady state. Fig. 5.9 shows the structure dependence of

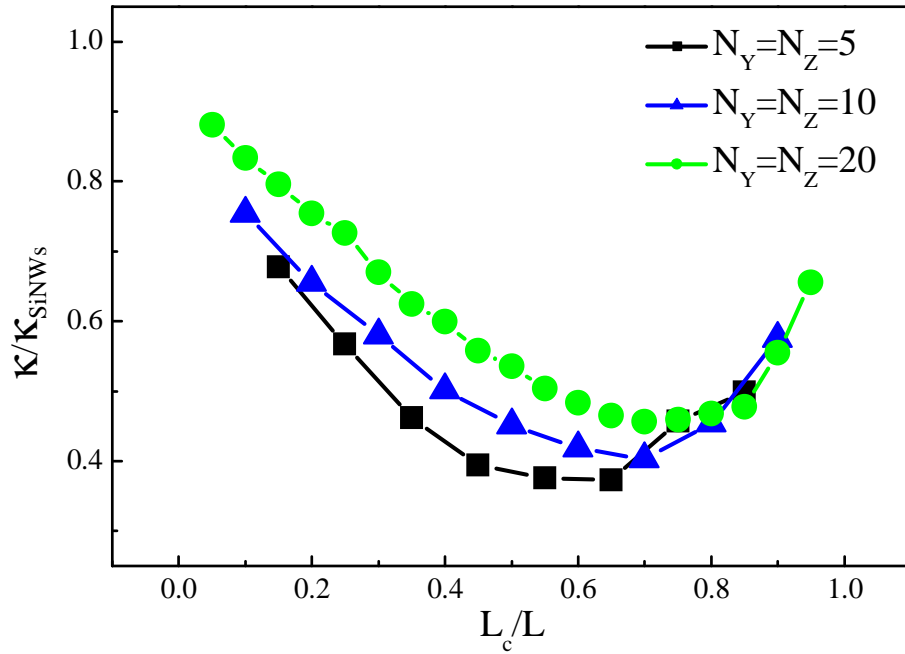


Figure 5.9: **Structure dependence of thermal conductivity in Ge/Si core-shell NWs with different cross section areas ($N_Y \times N_Z$ unit cells) at 300 K.** Thermal conductivity of SiNWs with the same cross section area is used as the reference. The length of the nanowire is 16 unit cells.

thermal conductivity in Ge/Si core-shell NWs with different cross section areas at 300 K. Thermal conductivity of SiNWs with the same cross section area is used as the reference. For all cross section areas, thermal conductivity can be reduced compared to that of SiNWs after introducing the core-shell structure. For the cross section of 5×5 unit cells, the trend of the structure-dependent thermal conductivity in Ge/Si core-shell NWs agrees quite well with that of P_{ave} with the same cross section shown in Fig. 5.8. With larger cross section areas, the structure dependence of thermal conductivity is qualitatively the same, with quantitative difference presumably due to the surface and diameter effect. These

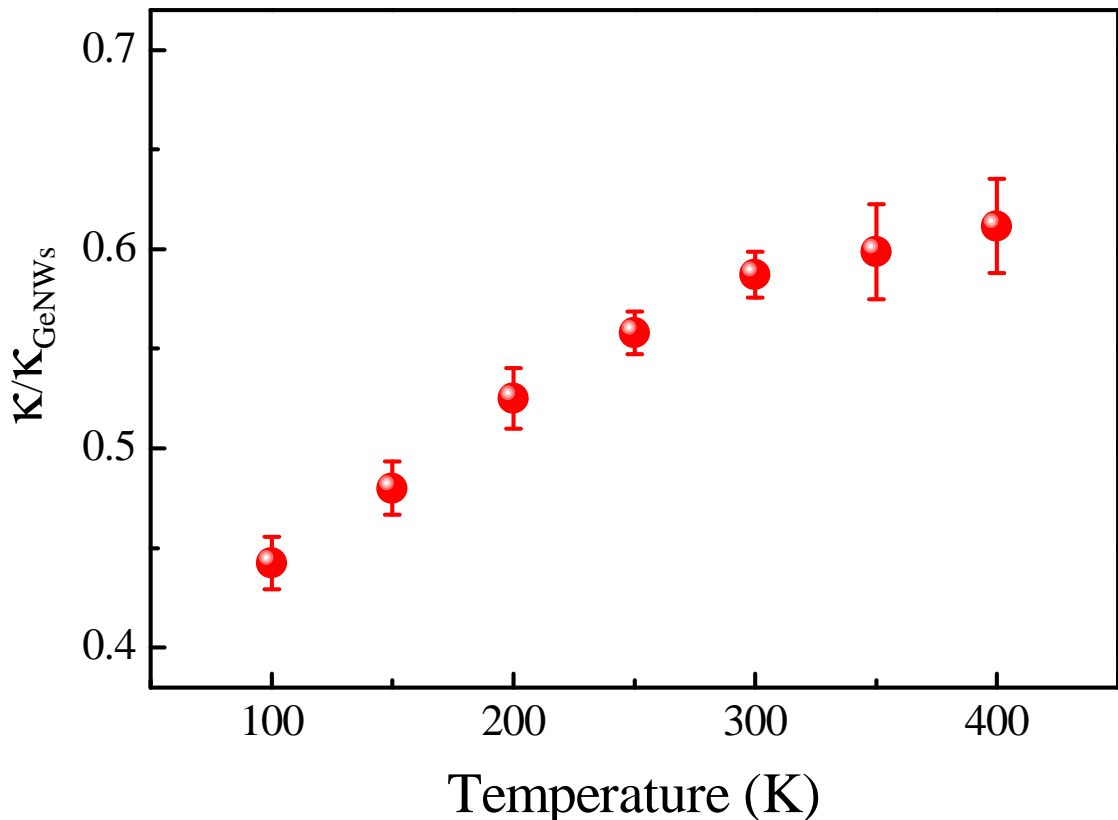


Figure 5.10: **Temperature dependence of thermal conductivity reduction in Ge/Si core-shell NWs.** Here thermal conductivity of Ge/Si core-shell NWs with a cross section of 5×5 unit cells and core-shell ratio $L_c/L=0.65$ is compared with that of GeNWs with the same cross section area at each temperature. The length of the nanowire is 16 unit cells.

results suggest that coherent resonance effect induced phonon localization effect is responsible for the structure-dependent reduction of thermal conductivity in Ge/Si core-shell NWs. However, as the surface effect is inherently considered in molecular dynamics simulations, the quantitative contribution from coherent resonance effect to the reduction of thermal conductivity in core-shell NWs is still an open question and needs further study.

As demonstrated in Fig. 5.5d, the stronger anharmonic phonon-phonon scattering at high temperature causes phonon to lose coherence, and leads to the vanishing of the resonance effect at high temperature. To further investigate the effect of coherent resonance on the reduction of thermal conductivity in core-shell NWs, we finally calculate the temperature dependence of thermal conductivity reduction in Ge/Si core-shell NWs. Thermal conductivity of Ge/Si core-shell NWs with a cross section of 5×5 unit cells and core-shell ratio $L_c/L=0.65$ is calculated and compared with that of GeNWs with the same cross section area at each temperature, taking into account the quantum correction [113]. Fig. 5.10 shows that the reduction of thermal conductivity is more significant at lower temperature. In addition, our simulation results show that it is possible to further reduce κ of low thermal conductivity material (Ge) by replacing the outer layers with high thermal conductivity material (Si) to form the core-shell structure.

5.5 Summary

In summary, we have systematically studied the phonon coherent resonance effect and thermal conductivity in core-shell NWs. We found in Ge/Si core-shell NWs an intriguing oscillation in HCACF, which is robust with the shape and detailed

structure of the interface. This oscillation is absent in pure silicon NWs, nanotube structures and randomly doped NWs. Detailed characterizations of the oscillation signal uncover that the physical origin of this oscillation is the coherent resonance effect of the transverse and longitudinal phonon modes, which is induced by the mode coupling in core-shell NWs. The phonon resonance causes the localization of the longitudinal phonon modes and consequently hinders thermal transport along the core-shell NWs. As a result, thermal conductivity of Ge/Si core-shell NWs can be tuned by the strength of the coherent resonance effect. Moreover, as the coherence of phonons can be better preserved at lower temperature, it is found that the reduction of thermal conductivity in core-shell NWs is more significant with the decrease of temperature. Our study suggests that the conventional phonon diffusive picture is not sufficient to describe thermal transport in core-shell NWs, and atomistic approaches without assumptions about the nature of phonon transport are suggested. More importantly, our study reveals a coherent mechanism to tune thermal conductivity in core-shell NWs by engineering phonon resonance.

Chapter 6

A Universal Gauge for Thermal Conductivity of Si Nanowires

In this chapter, we study thermal conductivity of silicon nanowires (SiNWs) with different cross sectional geometries. It is found that thermal conductivity decreases monotonically with the increase of surface-to-volume ratio (SVR). More interestingly, a simple universal linear dependence of thermal conductivity on SVR is observed for SiNWs with modest cross sectional area (larger than 20 nm^2), regardless of the cross sectional geometry. As a result, among different shaped SiNWs with the same cross sectional area, the one with triangular cross section has the lowest thermal conductivity. Our study provides not only a universal gauge for thermal conductivity among different cross sectional geometries, but also a designing guidance to tune thermal conductivity by geometry.

6.1 Motivation

Silicon nanowires (SiNWs) have shown tremendous promising applications in electronics, such as high-performance field-effect transistors (FETs) [38], logic gates [39], and nano sensors [42]. They have also attracted wide attention in thermo-electric applications because of the remarkably improved thermoelectric figure of merit, which is mainly caused by the significant reduction of thermal conductivity in SiNWs [44, 45]. Many approaches have been proposed to further reduce thermal conductivity of SiNWs, such as introduction of impurity scattering [81, 146] and holey structure [58, 59, 158].

The effect of orientations on thermal transport in SiNWs has been studied by Markussen *et al.* [29]. In their work, they found the thermal conductance is strongly anisotropic for pristine SiNWs: nanowires oriented along [110] direction have 50-75% larger thermal conductance than those oriented along [100] and [111] directions. Furthermore, by calculating phonon dispersion curves for SiNWs with different orientations, they found that nanowires in [110] direction have larger phonon group velocity compared to other two directions, which gives rise to the larger thermal conductance in [110] direction.

The well-developed fabrication technologies have offered a quite flexibility in the synthesis of nanowires with controllable diameter and cross sectional geometry [26, 167, 168]. Theoretical studies have revealed that different geometries are associated with different dynamics [169], which leads to completely different transport of elastic wave in phononic crystal at macroscopic level [170]. Although theoretical [151] and experimental [55] studies have shown that thermal conductivity of

SiNWs increases with the increase of transverse dimension, only fixed cross sectional geometry is considered so far. The effect of cross sectional geometry on thermal conductivity of nanostructures has not yet been explored.

In this chapter, we systematically study thermal conductivity of [100] SiNWs with different cross sectional geometries, including rectangle (square), circle and triangle. For simplicity, SiNWs with rectangular, circular, and triangular cross sectional shapes are named as rect-SiNWs, cir-SiNWs, and tri-SiNWs, respectively.

6.2 Universal Gauge Above Threshold

In our study, the longitudinal direction of SiNWs is set along x axis, and the transverse direction is cut into specific geometry with the cross sectional size controlled by the diameter, which is defined for all geometries as the maximum distance between the surface atoms in the cross sectional plane. The maximum cross sectional area considered in this study is 806 nm^2 . For cir- and tri-SiNWs, there exists certain discrepancy between the actual lattice structure and ideal geometry (Fig. 6.1) due to the discrete stacking of Si atoms. Compared to the ideal geometry, there are more surface atoms in the actual lattice structure of cir- and tri-SiNWs. However, these additional surface atoms are not included in the conventional definition of SVR (ratio of surface area to volume) based on ideal geometry. To take into account this discrepancy, here we define SVR at atomic level as the ratio of the number of surface atoms to the total number of atoms, which can accurately describe the surface morphology.

We use non-equilibrium molecular dynamics (NEMD) simulations with SW

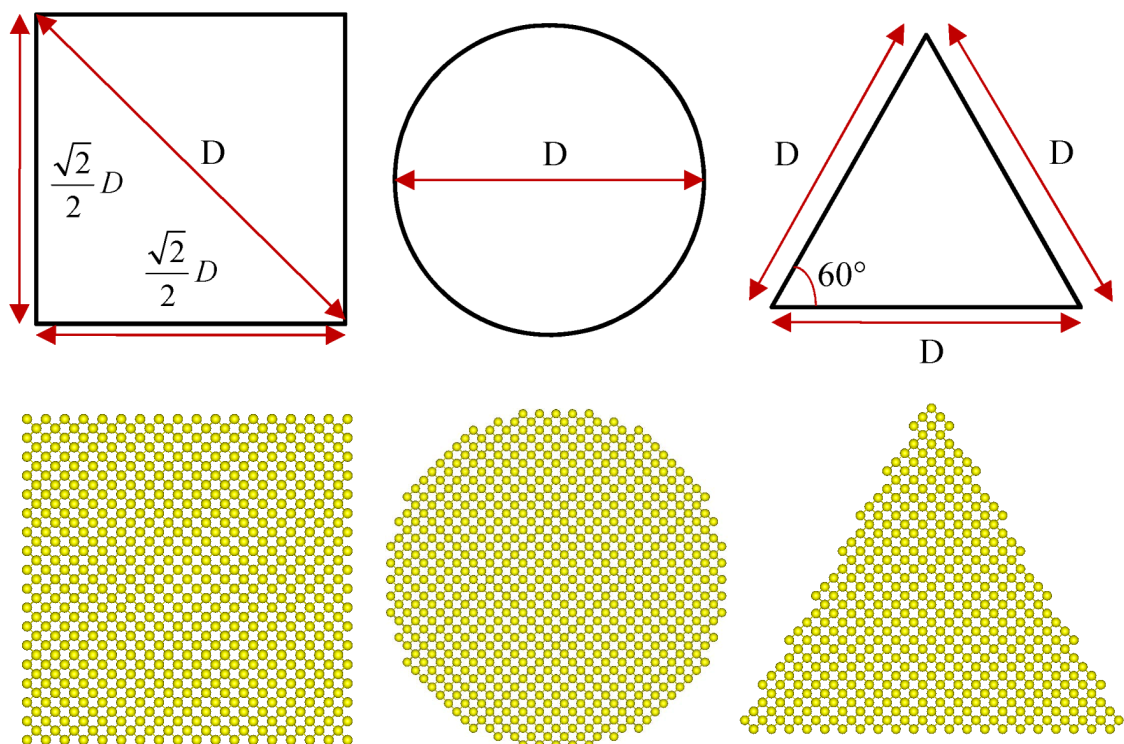


Figure 6.1: **Cross sectional view of the ideal geometry and actual lattice structure of [100] SiNWs.** The diameter D is defined for all geometries as the maximum distance between the surface atoms in the cross sectional plane.

potential (Chap. 2.2) and Langevin heat reservoir to calculate the thermal conductivity. The velocity Verlet algorithm (Chap. 2.3) is employed to integrate Newton's equations of motion numerically, and each MD step is set as 0.8 fs. Since quantum effect on thermal conductivity of SiNWs is quite small at room temperature [81], we do not adapt quantum correction in our study as we mainly concentrate on the cross sectional effect on thermal conductivity of SiNWs above room temperature.

We first calculate thermal conductivity of [100] SiNWs with different cross sectional areas and geometries at fixed length $L=3.26$ nm in the longitudinal direction. Fig. 6.2a-c shows the thermal conductivity κ versus SVR at different temperature. At each temperature, thermal conductivity decreases monotonically with the increase of SVR for any given cross sectional geometry, which is a consequence of the enhanced surface scattering when SVR increases. More interestingly, for different cross sectional geometries, thermal conductivity follows the same linear dependence on SVR when the cross sectional area is greater than certain threshold of about 20 nm^2 . This important feature suggests that SVR can serve as a universal gauge for thermal conductivity of SiNWs with modest cross sectional area, regardless of the specific cross sectional geometry. For very thin SiNWs with cross section area below the threshold, the dependence of thermal conductivity on SVR deviates from the universal linear fitted line, but depends also on the specific cross sectional geometry. In the following part of this chapter, we refer to the cross sectional area above and below this threshold as the “universal region” and “non-universal region”, respectively.

In the universal region, the linear dependence of thermal conductivity on SVR holds for all temperature above 300 K, with the absolute value of the slope for the

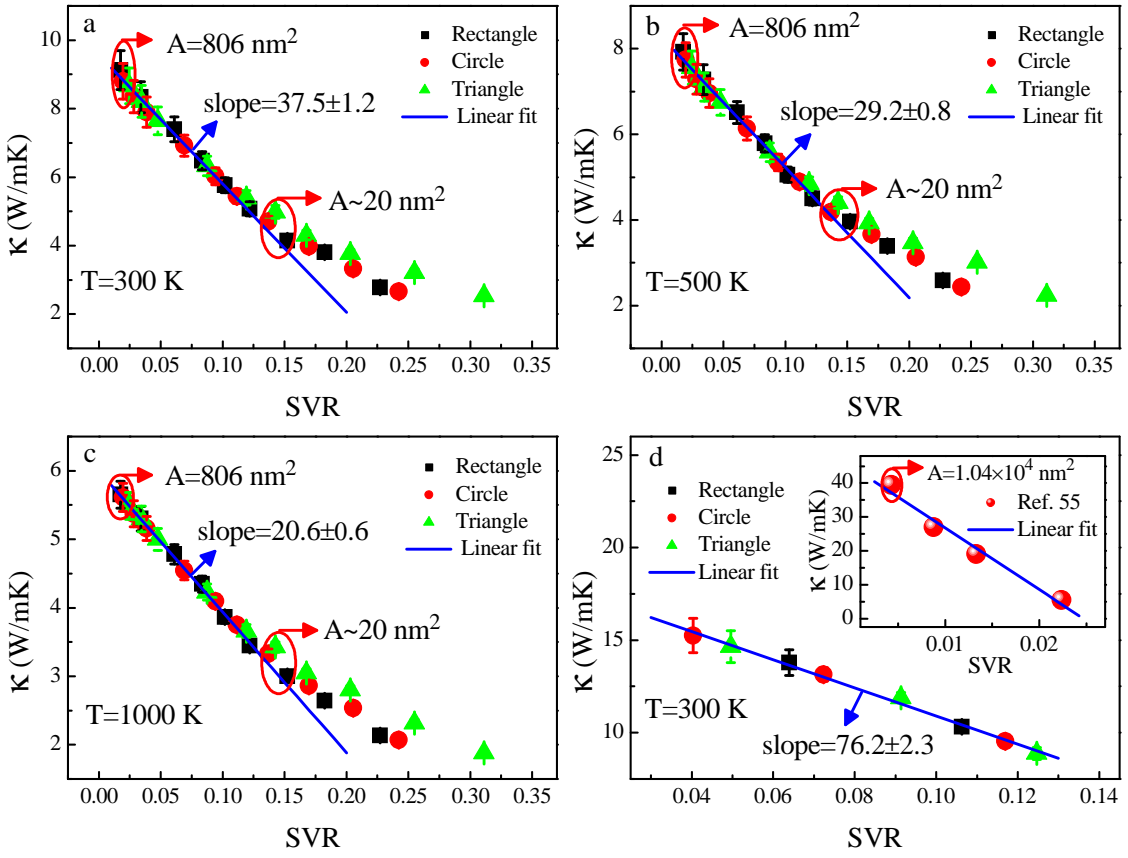


Figure 6.2: Thermal conductivity (κ) of [100] SiNWs versus surface-to-volume ratio (SVR) at different temperature. a 300 K, b 500 K, and c 1000 K. The nanowire length is fixed at $L=3.26$ nm. The black square, red circle and green triangle denote thermal conductivity of rect-SiNWs, cir-SiNWs and tri-SiNWs, respectively. d Thermal conductivity of SiNWs for different cross sectional geometries at 300 K. The nanowire length is $L=6.52$ nm. The inset shows experimental results at 300 K from Ref. [55]. In all figures, the blue lines are the best-fitting ones, and A is the cross sectional area.

linear best-fit decreases with the increase of temperature. This temperature dependence of the slope is mainly due to the temperature dependent phonon excitation in SiNWs. The increase of temperature will excite more high frequency phonons. However, surface scattering of high frequency (short wavelength) phonons in SiNW is weaker than that of low frequency phonons [44]. This is responsible for the decreased absolute value of the slope for the thermal conductivity versus SVR curve when temperature increases.

Another factor that influences the slope is the length of SiNWs. Fig. 6.2d shows the room temperature thermal conductivity versus SVR for SiNWs with length $L=6.52$ nm. Compared to Fig. 6.2a, the universal linear dependence of thermal conductivity on SVR holds as well at longer length, with an increased absolute value of the slope. Thermal conductivity of low dimensional materials is quite different from that of their bulk counterparts in the sense that it is usually length dependent. For instance, Chang *et al.* experimentally discovered the length dependence of thermal conductivity in carbon and boron-nitride nanotubes at room temperature [171]. Moreover, Yang *et al.* numerically studied thermal conductivity of SiNWs with length up to $1.1\text{ }\mu\text{m}$. They found that the length dependence of thermal conductivity persists even when the length is much longer than the phonon mean free path [70]. The phonon wavelength in a nanowire ranges from the lattice constant to the system length. For a short SiNW, with the increase of length, more and more long wavelength phonons are excited, which are sensitive to surface scattering [70] and correspond to the strong SVR dependence of thermal conductivity. This results in the increased absolute value of the slope for the thermal conductivity versus SVR curve when nanowire length increases.

To further check the validity of this linear dependence at much larger dimensional scale, in the inset of Fig. 6.2d, we also show the thermal conductivity versus SVR relation based on the experimental results from Ref. [55] for cir-SiNWs. The SiNWs used in Ref. [55] are single crystalline with the length of several microns and cross section area up to $1.04 \times 10^4 \text{ nm}^2$. A good linear SVR dependence also appears from their results (in Ref. [55], they showed the thermal conductivity vs diameter relation). The good agreement of experimental results with the linear fit line further supports the fact that the linear relation between thermal conductivity and SVR is an intrinsic phenomenon in nanowires.

One important application of the present study is to tailor thermal conductivity by geometry. For the same cross sectional area, SVR associated with different geometries is intrinsically different, leading to different thermal conductivity. For instance, Fig. 6.3 shows the normalized thermal conductivity of SiNWs with different cross sectional geometries above room temperature. For all cross sectional geometries, the cross sectional area is the same of about 33 nm^2 , which is in the universal region. Due to the intrinsically lowest SVR associated with rectangle, thermal conductivity of SiNW with rectangular cross section is the highest among all geometries, which is used as the reference at each temperature, respectively. The triangular cross section has the highest SVR, leading to about 18% reduction of thermal conductivity compared to the rectangular cross section. In addition, this reduction ratio is robust above room temperature.

The threshold in cross sectional area, above which SVR can serve as a universal gauge for thermal conductivity, is found to be about 20 nm^2 in our study, which only corresponds to about 5 nm in diameter for cir-SiNW. This dimensional

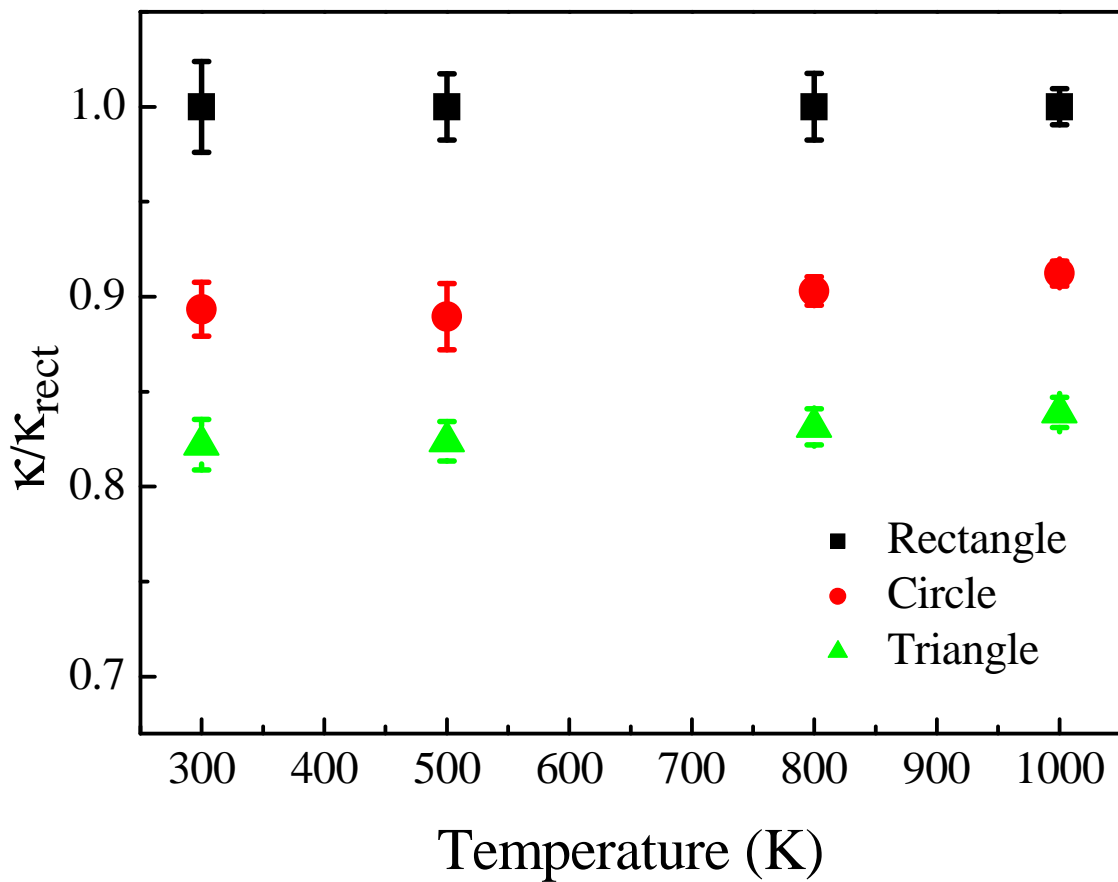


Figure 6.3: **Normalized thermal conductivity of SiNWs versus temperature for different cross sectional geometries.** Thermal conductivity of rect-SiNWs at each temperature is used as reference. The black square, red circle and green triangle denote thermal conductivity of rect-SiNWs, cir-SiNWs and tri-SiNWs, respectively. The cross sectional area is the same (about 33 nm^2) for all cross sectional geometries.

scale for the threshold is very close to the smallest diameter that current experimental fabrication can achieve [26]. Therefore, from practical point of view, SVR can be used as a universal gauge without any restriction of cross sectional area in experiment. However, from theoretical point of view, it is still of great interest to understand the physical origin that causes deviation from the universal linear dependence of thermal conductivity on SVR below the threshold. The non-universal region differs from the universal region mainly in the following two aspects. First, thermal conductivity is less sensitive to SVR in non-universal region than that in universal region. Second, in the non-universal region, thermal conductivity depends not only on SVR, but also on the specific cross sectional geometry: the trend of κ versus SVR for rect-SiNW and cir-SiNW is similar to each other, but notably different from that of tri-SiNW. Moreover, in this region, given the same SVR, tri-SiNW has a slightly higher thermal conductivity than that of the other two geometries.

6.3 Deviation Below Threshold

To explore the underlying physical mechanism, we carry out a vibrational eigen-mode analysis by using lattice dynamics simulation package, "General Utility Lattice Program" (GULP) [128]. The phonon participation ratio can provide detailed information about localization effect for each phonon mode in a given structure (Chap. 4.3). When considering the overall influence of structure change on localization effect, the averaged phonon participation ratio (P_{ave}) defined in Eq. (3.4) is a very useful quantity to characterize the overall localization effect, with a smaller P_{ave} indicating a stronger phonon localization effect [81]. Fig. 6.4

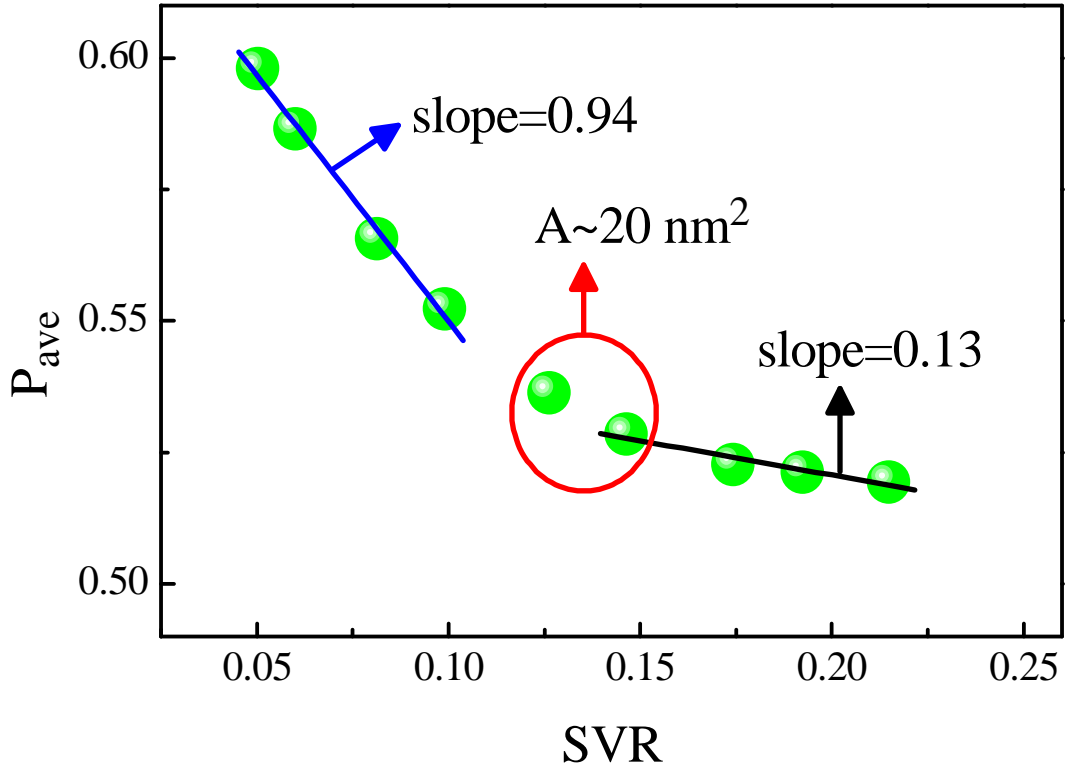


Figure 6.4: **Averaged phonon participation ratio (P_{ave}) versus surface-to-volume ratio (SVR) in SiNWs.** The blue and black lines are the best-fitting ones. The red circle highlights the threshold region of about 20 nm^2 in cross sectional area.

shows the calculation result of P_{ave} versus SVR. The blue and black lines draw the linear fit line of P_{ave} in universal and non-universal region, respectively. In both universal and non-universal region, P_{ave} decreases monotonically with the increase of SVR. In heat transport, the contribution to thermal conductivity mainly comes from the delocalized modes rather than the localized modes. The reduced P_{ave} means that the percentage of delocalized mode decreases, leading to the reduction of thermal conductivity. Furthermore, the decreasing slope of P_{ave} with respect to SVR is greater in the universal region than that in the non-universal region.

This difference of the decreasing slope is the origin that thermal conductivity is less sensitive to SVR in non-universal region than that in universal region.

To further identify the important factor that causes the cross sectional geometry dependence of thermal conductivity in the non-universal region, we study the spatial distribution of the localized phonon modes. As demonstrated in Chap. 4.3, the spatial distribution of the localized phonon modes can be effectively visualized by the local energy E_i defined in Eq. (4.2). To select the localized phonon modes, the summation in Eq. (4.2) only includes phonon modes with participation ratio less than 0.2.

Fig. 6.5 plots the normalized energy distribution for localized phonon modes on the cross sectional plane of SiNWs with cross sectional area greater than the threshold (in the universal region). Due to the dangling bond atoms on the surface which break the otherwise perfect lattice periodicity, phonon modes are localized on the surface with mode amplitude exponentially decaying with the distance from the surface [92]. This is well depicted in Fig. 6.5 that the localized phonon modes reside close to the boundary of the cross sectional plane with only a few layers in thickness, which corresponds to the surface of SiNWs and can be accurately described by SVR. Moreover, since the corner atoms are obviously different from other surface atoms due to their lower coordination number, they can induce a stronger localization effect. This is indeed manifested in Fig. 6.5 by a higher local energy at corner atoms compared to that at other surface atoms. Similar enhancement of the local energy at the sharp corner is also found in the study of electronic properties of thin SiNWs [35, 172]. However, this difference between corner atoms and other surface atoms is not taken into account by SVR which can only measure the percentage of surface atoms in the whole system. On the other

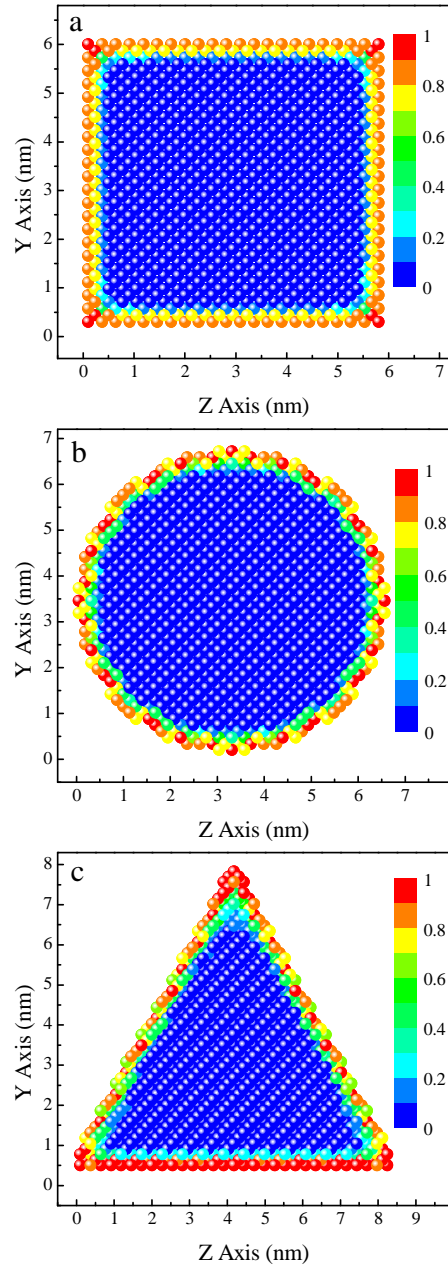


Figure 6.5: **Normalized energy distribution for the localized phonon modes on the cross sectional plane of SiNWs with large cross sectional area at 300 K.** Positions of the circles denote the different locations on the plane, and intensity of the energy is depicted according to the colour. a Rect-SiNW with $A = 32.5 \text{ nm}^2$. b Cir-SiNW with $A = 33.4 \text{ nm}^2$. c Tri-SiNW with $A = 28.8 \text{ nm}^2$.

hand, as shown in Fig. 6.5, the weight of corner atoms in the surface atoms is quite small when the cross sectional area is large. Meanwhile, the local energy is only about 20% higher at the corner atoms than that at other surface atoms. Therefore, when the cross sectional area is larger than the threshold value of about 20 nm^2 , the influence of corner atoms can be neglected, and SVR can effectively describe the phonon localization effect on the surface, thus there is a universal dependence of thermal conductivity on SVR among different cross sectional geometries.

However, the situation is quite different when the cross sectional area is less than the threshold value. Fig. 6.6 shows the normalized energy distribution for localized phonon modes in the small cross section case. When cross sectional area is smaller than the threshold, the enhancement of the local energy at the corner persists, and the contrast in local energy between corner atoms and other surface atoms is much larger than that shown in Fig. 6.5. Furthermore, the ratio of corner atoms on the surface is enhanced a lot compared to the large cross section case. Due to these reasons, the influence of corner atoms can no longer be neglected at small cross sectional area. As a result, in addition to SVR, the corner atoms which have a stronger localization effect compared to other surface atoms, also play an important role in determining thermal conductivity. As shown in Fig. 6.6, tri-SiNW has only three corners, while rect-SiNW and cir-SiNW have four corners. Therefore, in the non-universal region, the trend of κ versus SVR with rect-SiNW and cir-SiNW is similar to each other, but different from that with tri-SiNW. Because of the fewer corner atoms, thermal conductivity of tri-SiNW is slightly higher than that of rect-SiNW and cir-SiNW in the non-universal region, given the same SVR. Thus the cross sectional geometry dependence of thermal conductivity in the non-universal region is caused by the stronger phonon localization effect at

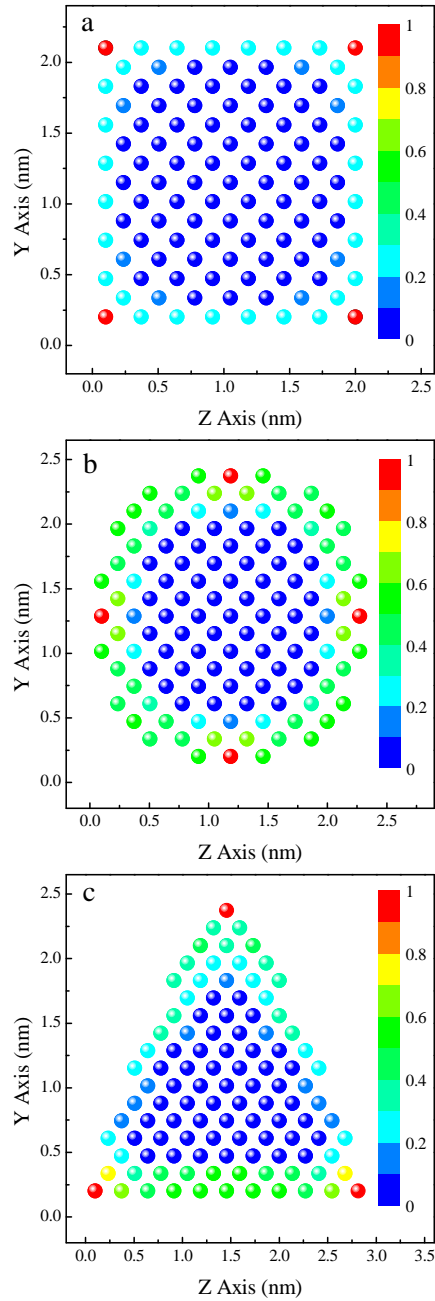


Figure 6.6: Normalized energy distribution for the localized phonon modes on the cross sectional plane of SiNWs with small cross sectional area at 300 K. Positions of the circles denote the different locations on the plane, and intensity of the energy is depicted according to the colour. a Rect-SiNW with $A = 3.6 \text{ nm}^2$. b Cir-SiNW with $A = 3.7 \text{ nm}^2$. c Tri-SiNW with $A = 3.2 \text{ nm}^2$.

the corner atoms and their increasing significance in thin SiNWs.

6.4 Discussion and Summary

Finally, we discuss the validity of other conventionally used gauge quantities for thermal conductivity, such as diameter and cross sectional area. Strictly speaking, the diameter is well defined only for circular cross section, but is ambiguous for other cross sectional geometries. Therefore, diameter is not suitable to serve as the universal gauge for thermal conductivity among different geometries. For the cross sectional area A , it can be defined for all geometries, and thermal conductivity usually increases monotonically with the increase of A for any given cross sectional geometry. In principle, it can be used as the gauge for thermal conductivity of nanowires with the same cross sectional geometry. But it is definitely not a universal gauge among different geometries, as it cannot take into account the specific surface morphology, which is a crucial factor in determining thermal conductivity at nanoscale. For example, we have demonstrated in Fig. 6.3 that even with the same cross section area, thermal conductivity of SiNWs with different geometries can differ by as large as 18% due to the intrinsically different SVR. Another example is that thermal conductivity of SiNWs with different cross sectional geometries can be quite close to each other due to the similar SVR, even if the cross sectional area differs by several times. For instance, we found in our simulations that room temperature thermal conductivity of rect-SiNW with $A = 62 \text{ nm}^2$ (thermal conductivity is $7.5 \pm 0.4 \text{ W/mK}$) is very close to that of the tri-SiNW with $A = 213 \text{ nm}^2$ (thermal conductivity is $7.6 \pm 0.4 \text{ W/mK}$), while the cross sectional area differs by more than a factor of 3. Therefore, SVR as the gauge for thermal conductivity

has its advantage over other conventionally used gauge quantities in the sense that it is a universal one among different geometries, when the cross sectional area is greater than the threshold.

In summary, we have studied thermal conductivity of SiNWs with different cross sectional geometries and cross sectional area up to 806 nm^2 . A universal linear dependence of thermal conductivity on surface-to-volume ratio is found for SiNWs with modest cross sectional area larger than about 20 nm^2 , regardless of the specific cross sectional geometry. Moreover, we found the absolute value of the slope for the linear fit line depends on both temperature and length, due to the temperature and length dependence of thermal conductivity of SiNWs. In addition, with the same cross sectional area (larger than 20 nm^2), tri-SiNW has the lowest thermal conductivity due to its intrinsically highest SVR, which might be favorable in thermoelectric applications. Our study provides not only a universal gauge for thermal conductivity among different cross sectional geometries, but also a simple approach to tune thermal conductivity by geometry.

Chapter 7

Conclusions

7.1 Contribution

In this thesis, we have investigated some critical aspects of the molecular dynamics (MD) methodology. We have examined the impact of heat bath in the non-equilibrium molecular dynamics (NEMD) simulations of nanostructures, including heat bath type, number of layers, and heat bath parameter. Using silicon nanowires (SiNWs) as an example, we have studied the effect of heat bath on calculated thermal properties. We found when applying Nosé-Hoover (NH) heat bath to the two ends of SiNWs, the localized edge modes (LEMs) at the boundary can accumulate over time due to the deterministic nature of NH heat bath, and induce large temperature jump at the boundary. As a result, multiple layers of NH heat bath are required in order to reduce the temperature jump. While with Langevin heat bath, it can eliminate the accumulation of LEMs due to its stochastic excitation of all modes, giving rise to a small temperature jump at the

boundary, regardless of heat bath layers applied. In addition, in order to obtain the correct temperature profile, intermediate values of heat bath parameters are recommended for both NH and Langevin heat bath. We further demonstrate through silicon-germanium nanojunctions that in the study of heat current rectification in heterogeneous materials, Langevin heat bath is recommended because it can give consistent results with experiment, regardless of the heat bath parameter. On the contrary, NH heat bath may induce the artifact which shows remarkable dependence on the heat bath parameter.

Moreover, we have also examined different implementations of Green-Kubo formula in equilibrium molecular dynamics (EMD) simulations. Due to the finite number of ensemble average, heat current autocorrelation function (HCACF) is only reliable up to a cut-off time and thus the thermal conductivity can only be calculated from the truncated HCACF. We have proposed an efficient quantitative method (first avalanche) to accurately estimate the cut-off time. Using the cut-off time, direct integration method can make a successful computation of thermal conductivity of crystalline silicon and germanium. In addition, we have demonstrated that because of the finite cut-off time, a small nonzero correction term can significantly improve the accuracy of EMD calculations based on the double-exponential-fitting of HCACF. Excluding this term in the calculation gives rise to an underestimated value of thermal conductivity due to the partial exclusion of contribution from low-frequency phonons, while including it one can make a correct prediction in good agreement with experimental value. Since the two-stage exponential decaying characteristic of HCACF has been found in various materials and has profound underlying physical mechanism, our method is quite general and can have wide applications in accurate thermal conductivity estimations of

different materials and systems.

In addition to the study of MD methodology, we have demonstrated various strategies that can efficiently reduce thermal conductivity of SiNWs, which might be helpful towards developing high-efficiency thermoelectric devices based on silicon. By using NEMD simulations, we have studied thermal conductivity of randomly doped $\text{Si}_{1-x}\text{Ge}_x$ NWs and found it depends on the composition remarkably. Its thermal conductivity reaches the minimum, which is about 18% of that of pure SiNWs, when Ge content is 50%. More interesting, with only 5% Ge atoms, thermal conductivity of SiNWs can be reduced 50%. This composition dependence of thermal conductivity is explained by phonon participation ratio. In addition, we have also investigated the thermal conductivity of superlattice structured Si/Ge NWs. The dependence of thermal conductivity on the period length is explained by the overlap of phonon power spectrum of different layers.

Besides random doping and superlattice structure, we have proposed to reduce thermal conductivity of SiNWs by introducing small hole at the center, i.e., construct silicon nanotube (SiNT) structures. EMD simulations results demonstrate that a very small hole which accounts for only 1% of cross sectional area can induce 35% reduction of room temperature thermal conductivity. Moreover, with the same cross section area, thermal conductivity of SiNT is only about 33% of that of SiNW at room temperature. The enhanced surface-to-volume ratio in SiNTs reduces the percentage of delocalized modes, which is believed to be responsible for the reduction of thermal conductivity.

In addition to these conventional incoherent mechanisms to reduce thermal conductivity, we have observed in core-shell NWs a remarkable oscillation effect in heat current autocorrelation function, while the same effect is absent in pure

silicon nanowires, nanotube structures and randomly doped nanowires. Detailed characterizations of the oscillation signal have shown that this intriguing oscillation is caused by the coherent resonance effect of the transverse and longitudinal phonon modes. This phonon resonance results in the localization of the longitudinal modes, which leads to the reduction of thermal conductivity in core-shell nanowires. Our study reveals a coherent mechanism to tune thermal conductivity in core-shell nanowires by engineering phonon resonance.

Finally, we have studied thermal conductivity of SiNWs with different cross sectional geometries and cross sectional area up to 806 nm^2 . A universal linear dependence of thermal conductivity on surface-to-volume ratio (SVR) is found for SiNWs with modest cross sectional area larger than about 20 nm^2 , regardless of the specific cross sectional geometry. Moreover, we found the absolute value of the slope for the linear fit line depends on both temperature and length, due to the temperature and length dependence of thermal conductivity of SiNWs. In addition, with the same cross sectional area (larger than 20 nm^2), tri-SiNW has the lowest thermal conductivity due to its intrinsically highest SVR, which might be favorable in thermoelectric applications. Our study provides not only a universal gauge for thermal conductivity among different cross sectional geometries, but also a simple approach to tune thermal conductivity by geometry.

7.2 Future Work and Outlook

In this thesis, we have demonstrated various strategies that can independently reduce thermal conductivity of SiNWs. It is interesting to know to what extent a combination of these strategies can further reduce the thermal conductivity.

Moreover, with such complex design, it is worth further study to see whether it is possible to approach the minimum thermal conductivity (amorphous limit) of Si that is insensitive to the system parameters (e.g., temperature) while still preserving the basic crystal structure. This is the ideal case for high-efficiency thermoelectrics as the material is now so-called electron-crystal and phonon-gas.

In Chapter 6, we have found a universal relation between the thermal conductivity and SVR in SiNWs with modest cross sectional area, regardless of the specific cross sectional geometry. In our study, only pristine SiNWs with outer surface have been considered. As an extension, one can check whether this relation still holds when inner surface is introduced, such as the SiNT structure in Chapter 4, or even multiple holes with different shapes in the middle of SiNWs. This study might provide more insights to the theoretical design of thermal properties by surface engineering.

In Chapter 6, we have qualitatively discussed the temperature-dependence of the slope for the linear fitting. A further analysis of the slope data reveals that the slope goes linearly with $1/\sqrt{T}$ quite well, which might have underlying physical significance. This inversely square root dependence on temperature seems interesting and its underlying mechanism is worth further exploration. More simulations at different temperature are needed to verify this inversely square root dependence of the slope on temperature.

The universal relation between thermal conductivity and SVR discussed in Chapter 6 suggests that the surface scattering is a more important factor in thermal transport than the specific cross sectional geometry. As discussed in Chapter 5, the interface is different from the surface as it can induce mode coupling which can be used to tune thermal conductivity. On the other hand, the interface can also

Chapter 7. Conclusions

cause scattering, and thus it is more complex than the surface. In the presence of interface, one can further study whether there exists any nontrivial geometry effect on thermal transport in core-shell structure.

In this thesis, we have only studied the thermal properties of individual nanostructures. The periodic arrangement of individual nanostructures into the phononic crystals with nanoscale features is a very interesting research area, and is becoming available with the continuous development of micro-fabrication technique. Future study on the thermal properties of the phononic crystals with nanoscale features is promising, and might stimulate research interest in both communities of phononic crystals and thermal transport.

Bibliography

- [1] S. Iijima, *Nature* **354**, 56 (1991).
- [2] M. Brandbyge, J. Schiotz, M. R. Sorensen, P. Stoltze, K. W. Jacobsen, J. K. Norskov, L. Olesen, E. Laegsgaard, I. Stensgaard, and F. Besenbacher, *Phys. Rev. B* **52**, 8499 (1995).
- [3] S. F. Hu, W. Z. Wong, S. S. Liu, Y. C. Wu, C. L. Sung, T. Y. Huang, and T. J. Yang, *Adv. Mater.* **14**, 736 (2002).
- [4] A. H. Castro Neto, F. Guinea, N. M. R. Peres, K. S. Novoselov, and A. K. Geim, *Rev. Mod. Phys.* **81**, 109 (2009).
- [5] W. Lu, and C. M. Lieber, *J. Phys. D: Appl. Phys.* **39**, R387 (2006).
- [6] C. M. Lieber, *MRS Bull.* **28**, 486 (2003).
- [7] Y. Wu, and P. Yang, *J. Am. Chem. Soc.* **123**, 3165 (2001).
- [8] A. M. Morales, and C. M. Lieber, *Science* **279**, 208 (1998).
- [9] J. L. Liu, S. J. Cai, G. L. Jin, S. G. Thomas, and K. L. Wang, *J. Cryst. Growth* **200**, 106 (1999).
- [10] C. Yang, Z. Zhong, and C. M. Lieber, *Science* **310**, 1304 (2005).

Bibliography

- [11] Y. Wu, Y. Cui, L. Huynh, C. J. Barrelet, D. C. Bell, and C. M. Lieber, *Nano Lett.* **4**, 433 (2004).
- [12] L. J. Lauhon, M. S. Gudiksen, D. Wang, and C. M. Lieber, *Nature* **420**, 57 (2002).
- [13] W. Lu, J. Xiang, B. P. Timko, Y. Wu, and C. M. Lieber, *Proc. Natl. Acad. Sci. USA* **102**, 10046 (2005).
- [14] F. Qian, S. Gradecak, Y. Li, C. Y. Wen, and C. M. Lieber, *Nano Lett.* **5**, 2287 (2005).
- [15] M. S. Gudiksen, L. J. Lauhon, J. Wang, D. C. Smith, and C. M. Lieber, *Nature* **415**, 617 (2002).
- [16] Y. Wu, R. Fan, and P. Yang, *Nano Lett.* **2**, 83 (2002).
- [17] C. C. Chen, and C. C. Yeh, *Adv. Mater.* **12**, 738 (2000).
- [18] X. Duan, and C. M. Lieber, *Adv. Mater.* **12**, 298 (2000).
- [19] X. Duan, J. Wang, and C. M. Lieber, *Appl. Phys. Lett.* **76**, 1116 (2000).
- [20] W. S. Shi, Y. F. Zheng, N. Wang, C. S. Lee, and S. T. Lee, *J. Vac. Sci. Technol. B* **19**, 1115 (2001).
- [21] M. Yazawa, M. Koguchi, A. Muto, and K. Hiruma, *Adv. Mater.* **5**, 577 (1993).
- [22] Y. Wang, L. Zhang, C. Liang, G. Wang, and X. Peng, *Chem. Phys. Lett.* **357**, 314 (2002).
- [23] Y. Wang, G. Meng, L. Zhang, C. Liang, and J. Zhang, *Chem. Mater.* **14**, 1773 (2002).

Bibliography

- [24] M. Lopez-Lopez, A. Guillen-Cervantes, Z. Rivera-Alvarez, and I. Hernandez-Calderon, *J. Cryst. Growth* **193**, 528 (1998).
- [25] Y. Zhao, and B. I. Yakobson, *Phys. Rev. Lett.* **91**, 035501 (2003).
- [26] D. D. D. Ma, C. S. Lee, F. C. K. Au, S. Y. Tong, and S. T. Lee, *Science* **299**, 1874 (2003).
- [27] R. He, and P. Yang, *Nat. Nanotechnol.* **1**, 42 (2006).
- [28] R. Rurali, and N. Lorente, *Phys. Rev. Lett.* **94**, 026805 (2005).
- [29] T. Markussen, A. -P. Jauho, and M. Brandbyge, *Nano Lett.* **8**, 3771 (2008).
- [30] A. J. Read, R. J. Needs, K. J. Nash, L. T. Canham, P. D. J. Calcott, and A. Qteish, *Phys. Rev. Lett.* **69**, 1232 (1992).
- [31] X. Zhao, C. M. Wei, L. Yang, and M. Y. Chou, *Phys. Rev. Lett.* **92**, 236805 (2004).
- [32] P. W. Leu, B. Shan, and K. Cho, *Phys. Rev. B* **73**, 195320 (2006).
- [33] M. -F. Ng, L. Zhou, S. -W. Yang, L. Y. Sim, V. B. C. Tan, and P. Wu, *Phys. Rev. B* **76**, 155435 (2007).
- [34] R. Rurali, *Rev. Mod. Phys.* **82**, 427 (2010).
- [35] D. Yao, G. Zhang, and B. Li, *Nano Lett.* **8**, 4557 (2008).
- [36] T. Vo, A. J. Williamson, and G. Galli, *Phys. Rev. B* **74**, 045116 (2006).
- [37] A. R. Guichard, D. N. Barsic, S. Sharma, T. I. Kamins, and M. L. Brongersma, *Nano Lett.* **6**, 2140 (2006).

Bibliography

- [38] Y. Cui, Z. Zhong, D. Wang, W. Wang, and C. M. Lieber, *Nano Lett.* **3**, 149 (2003).
- [39] Y. Huang, X. Duan, Y. Cui, L. J. Lauhon, K. -H. Kim, and C. M. Lieber, *Science* **294**, 1313 (2001).
- [40] X. Duan, Y. Huang, and C. M. Lieber, *Nano Lett.* **2**, 487 (2002).
- [41] B. Tian, X. Zheng, T. J. Kempa, Y. Fang, N. Yu, G. Yu, J. Huang, and C. M. Lieber, *Nature* **449**, 885 (2007).
- [42] Y. Cui, Q. Wei, H. Park, and C. M. Lieber, *Science* **293**, 1289 (2001).
- [43] Z. Zhong, D. Wang, Y. Cui, M. W. Bockrath, and C. M. Lieber, *Science* **302**, 1377 (2003).
- [44] A. I. Hochbaum, R. Chen, R. D. Delgado, W. Liang, E. C. Garnett, M. Najarian, A. Majumdar, and P. Yang, *Nature* **451**, 163 (2008).
- [45] A. I. Boukai, Y. Bunimovich, J. T. Kheli, J. -K. Yu, W. A. Goddard III, and J. R. Heath, *Nature* **451**, 168 (2008).
- [46] Y. Xia, P. Yang, Y. Sun, Y. Wu, B. Mayers, B. Gates, Y. Yin, F. Kim, and H. Yan, *Adv. Mater.* **15**, 353 (2003).
- [47] F. Patolsky, and C. M. Lieber, *Mater. Today* **8**, 20 (2005).
- [48] Y. Li, F. Qian, J. Xiang, and C. M. Lieber, *Mater. Today* **9**, 18 (2006).
- [49] G. J. Snyder, and E. S. Toberer, *Nat. Mater.* **7**, 105 (2008).
- [50] D. M. Rowe, and G. Min, *J. Mater. Sci. Lett.* **14**, 617 (1995).

Bibliography

- [51] Website of the Thermoelectrics group at Caltech Material Science.
<http://www.thermoelectrics.caltech.edu/thermoelectrics/index.html>
- [52] C. J. Vineis, A. Shakouri, A. Majumdar, and M. G. Kanatzidis, *Adv. Mater.* **22**, 3970 (2010).
- [53] G. S. Nolas, D. T. Morelli, and T. M. Tritt, *Annu. Rev. Mater. Sci.* **29**, 89 (1999).
- [54] M. S. Dresselhaus, G. Chen, M. Y. Tang, R. Yang, H. Lee, D. Wang, Z. Ren, J. -P. Fleurial, and P. Gogna, *Adv. Mater.* **19**, 1043 (2007).
- [55] D. Li, Y. Wu, P. Kim, L. Shi, P. Yang, and A. Majumdar, *Appl. Phys. Lett.* **83**, 2934 (2003).
- [56] L. Weber, and E. Gmelin, *Appl. Phys. A* **53**, 136 (1991).
- [57] D. G. Cahill, S. K. Watson, and R. O. Pohl, *Phys. Rev. B* **46**, 6131 (1992).
- [58] J. -K. Yu, S. Mitrovic, D. Tham, J. Varghese, and J. R. Heath, *Nature Nanotech.* **5**, 718 (2010).
- [59] J. Tang, H. -T. Wang, D. H. Lee, M. Fardy, Z. Huo, T. P. Russell, and P. Yang, *Nano Lett.* **10**, 4279 (2010).
- [60] A. Rahman, *Phys. Rev.* **136**, A405 (1964).
- [61] K. M. Glassford, J. R. Chelikowsky, and J. C. Phillips, *Phys. Rev. B* **43**, 14557 (1991).
- [62] R. Ochoa, T. P. Swiler, and J. H. Simmons, *J. Non-Crystalline Solids* **128**, 57 (1991).

Bibliography

- [63] F. F. Abraham, and J. Q. Broughton, *Phys. Rev. Lett.* **56**, 734 (1986).
- [64] U. Landman, W. D. Luedtke, R. N. Barnett, C. L. Cleveland, M. W. Ribarsky, E. Arnold, S. Ramesh, H. Baumgart, A. Martinez, and B. Khan, *Phys. Rev. Lett.* **56**, 266 (1986).
- [65] B. P. Feuston, R. K. Kalia, and P. Vashishta, *Phys. Rev. B* **35**, 6222 (1987).
- [66] D. W. Brenner, B. I. Dunlap, J. A. Harrison, J. W. Mintmire, R. C. Mowrey, D. H. Robertson, and C. T. White, *Phys. Rev. B* **44**, 3479 (1991).
- [67] H. J. C. Berendsen, *Comp. Phys. Commun.* **44**, 233 (1987).
- [68] H. Peelaers, B. Partoens, and F. M. Peeters, *Nano Lett.* **9**, 107 (2009).
- [69] L. Yang, and M. Y. Chou, *Nano Lett.* **11**, 2618 (2011).
- [70] N. Yang, G. Zhang, and B. Li, *Nano Today* **5**, 85 (2010).
- [71] J. Chen, G. Zhang, and B. Li, *J. Chem. Phys.* **135**, 204705 (2011).
- [72] J. P. Hansen, and I. R. McDonald, *Theory of Simple Liquids* 2nd Ed., Academic Press (1986).
- [73] K. Huang, *Statistical Mechanics* 2nd Ed., Jonh Wiley & Sons (1987).
- [74] J. E. Turney, A. J. H. McGaughey, and C. H. Amon, *Phys. Rev. B* **79**, 224305 (2009).
- [75] P. N. Keating, *Phys. Rev.* **145**, 637 (1966).
- [76] F. H. Stillinger, and T. A. Weber, *Phys. Rev. B* **31**, 5262 (1985).
- [77] M. D. Kluge, J. R. Ray, and A. Rahman, *J. Chem. Phys.* **85**, 4028 (1986).

Bibliography

- [78] J. Q. Broughton, and X. P. Li, *Phys. Rev. B* **35**, 9120 (1987).
- [79] J. S. Kallman, W. G. Hoover, C. G. Hoover, A. J. DeGroot, S. M. Lee, and F. Wooten, *Phys. Rev. B* **47**, 7705 (1993).
- [80] K. Ding, and H. C. Andersen, *Phys. Rev. B* **34**, 6987 (1986).
- [81] J. Chen, G. Zhang, and B. Li, *Appl. Phys. Lett.* **95**, 073117 (2009).
- [82] V. I. Arnold, *Mathematical Methods of Classical Mechanics* 2nd Ed., Springer (1989).
- [83] M. P. Allen, and D. J. Tildesley, *Computer Simulation of Liquids* Oxford University Press (1989).
- [84] R. Kubo, *Rep. Prog. Phys.* **29**, 255 (1986).
- [85] F. Müller-Plathe, *J. Chem. Phys.* **106**, 6082 (1997).
- [86] T. Ikeshoji, and B. Hafskjold, *Mol. Phys.* **81**, 251 (1994).
- [87] G. Wu, and B. Li, *Phys. Rev. B* **76**, 085424 (2007).
- [88] S. Nosé, *J. Chem. Phys.* **81**, 511 (1984).
- [89] W. G. Hoover, *Phys. Rev. A* **31**, 1695 (1985).
- [90] A. Dhar, *Adv. Phys.* **57**, 457 (2008).
- [91] D. Donadio, and G. Galli, *Phys. Rev. Lett.* **102**, 195901 (2009).
- [92] J. -W. Jang, J. Chen, J. -S. Wang, and B. Li, *Phys. Rev. B* **80**, 052301 (2009).
- [93] S. Y. Kim, and H. S. Park, *Nano Lett.* **9**, 969 (2009).

Bibliography

- [94] M. P. Lima, A. Fazzio, and A. J. R. da Silva, *Phys. Rev. B* **79**, 153401 (2009).
- [95] L. Yang, M. L. Cohen, and S. G. Louie, *Phys. Rev. Lett.* **101**, 186401 (2008).
- [96] A. Bermudez, D. Patane, L. Amico, and M. A. Martin-Delgado, *Phys. Rev. Lett.* **102**, 135702 (2009).
- [97] H. J. C. Berendsen, J. P. M. Postma, W. F. van Gunsteren, A. DiHola, and J. R. Haak, *J. Chem. Phys.* **81**, 3684 (1984).
- [98] P. H. Hünenberger, *Adv. Polymer. Sci.* **173**, 105 (2005).
- [99] A. L. Cheng, and K. M. Merz, *J. Phys. Chem.* **100**, 1927 (1996).
- [100] V. L. Golo, and K. V. Shaitan, *Biofizika* **47**, 611 (2002).
- [101] A. Mor, G. Ziv, and Y. Levy, *J. Comput. Chem.* **29**, 1992 (2008).
- [102] E. Rosta, N. V. Buchete, and G. Hummer, *J. Chem. Theory Comput.* **5**, 1393 (2009).
- [103] N. Yang, G. Zhang, and B. Li, *Appl. Phys. Lett.* **95**, 033107 (2009).
- [104] B. Li, L. Wang, and G. Casati, *Phys. Rev. Lett.* **93**, 184301 (2004).
- [105] C. W. Chang, D. Okawa, A. Majumdar, and A. Zettl, *Science* **314**, 1121 (2006).
- [106] E. S. Landry, and A. J. H. McGaughey, *Phys. Rev. B* **80**, 165304 (2004).
- [107] M. S. Green, *J. Chem. Phys.* **22**, 398 (1954).
- [108] R. Kubo, *J. Phys. Soc. Jpn.* **12**, 570 (1957).

Bibliography

- [109] R. Kubo, M. Yokota, and S. Nakajima, *J. Phys. Soc. Jpn.* **12**, 1203 (1957).
- [110] J. Li, and L. Porter, *J. Nucl. Mater.* **255**, 139 (1998).
- [111] J. Che, T. Cagin, W. Deng, and W. A. Goddard, *J. Chem. Phys.* **113**, 6888 (2000).
- [112] Y. H. Lee, R. Biswas, C. M. Soukoulis, C. Z. Wang, C. T. Chan, and K. M. Ho, *Phys. Rev. B* **43**, 6573 (1991).
- [113] S. G. Volz, and G. Chen, *Phys. Rev. B* **61**, 2651 (2000).
- [114] Z. Yao, J.-S. Wang, B. Li, and G.-R. Liu, *Phys. Rev. B* **71**, 085417 (2005).
- [115] R. Zwanzig, *Ann. Rev. Phys. Chem.* **16**, 67 (1965).
- [116] R. Kubo, M. Toda, and N. Hashitsume, *Statistical Physics* Vol. II, Springer-Verlag: Berlin (1985).
- [117] A. Kundu, A. Dhar, and O. Narayan, *J. Stat. Mech. Theor. Exp.* L03001 (2009).
- [118] P. K. Schelling, S. R. Phillpot, and P. Kebblinski, *Phys. Rev. B* **65**, 144306 (2002).
- [119] L. W. Couch, *Digital and analog communications systems* 6th Ed., Prentice Hall (2001).
- [120] J. Dong, O. F. Sankey, and C. W. Myles, *Phys. Rev. Lett.* **86**, 2361 (2001).
- [121] A. J. H. McGaughey, and M. Kaviany, *Int. J. Heat Mass Transfer* **47**, 1783 (2004).

Bibliography

- [122] R. J. Hardy, *Phys. Rev.* **132**, 168 (1963).
- [123] M. G. Holland, *Phys. Rev.* **132**, 2461 (1963).
- [124] C. J. Glassbrenner, and G. A. Slack, *Phys. Rev.* **134**, A1058 (1964).
- [125] Y. B. Magomedov, and G. G. Gadjiev, *High Temp.* **46**, 422 (2008).
- [126] A. S. Henry, and G. Chen, *J. Comput. Theor. Nanosci.* **5**, 1 (2008).
- [127] M. T. Dove, *Introduction to Lattice Dynamics* Cambridge University Press (1993).
- [128] J. D. Gale, *J. Chem. Soc., Faraday Trans.* **93**, 629 (1997).
- [129] Website of GULP. <https://projects.ivec.org/gulp/>
- [130] A. Bodapati, P. K. Schelling, S. R. Phillpot, and P. Keblinski, *Phys. Rev. B* **74**, 245207 (2006).
- [131] J. -E. Yang, C. -B. Jin, C. -J. Kim, and M. -H. Jo, *Nano Lett.* **6**, 2679 (2006).
- [132] R. Venkatasubramanian, E. Siivola, T. Colpitts, and B. O'Quinn, *Nature* **413**, 597 (2001).
- [133] L. D. Hicks, and M. S. Dresselhaus, *Phys. Rev. B* **47**, 16631 (1993).
- [134] T. Vo, A. J. Williamson, V. Lordi, and G. Galli, *Nano Lett.* **8**, 1111 (2008).
- [135] R. N. Musin, and X. -Q. Wang, *Phys. Rev. B* **74**, 165308 (2006).
- [136] D. B. Migas, and V. E. Borisenko, *Phys. Rev. B* **76**, 035440 (2007).

Bibliography

- [137] L. Yang, R. N. Musin, X. -Q. Wang, and M. Y. Chou, *Phys. Rev. B* **77**, 195325 (2008).
- [138] L. H. Shi, D. L. Yao, G. Zhang, and B. Li, *Appl. Phys. Lett.* **95**, 063102 (2009).
- [139] A. Skye, and P. K. Schelling, *J. Appl. Phys.* **103**, 113524 (2008).
- [140] J. P. Dismukes, L. Ekstrom, E. F. Steigmeier, I. Kudman, and D. S. Beers, *J. Appl. Phys.* **35**, 2899 (1964).
- [141] X. Y. Yu, G. Chen, A. Verma, and J. S. Smith, *Appl. Phys. Lett.* **67**, 3554 (1995).
- [142] S. T. Huxtable, A. R. Abramson, C. -L. Tien, A. Majumdar, C. LaBounty, X. Fan, G. Zeng, J. E. Bowers, A. Shakouri, and E. T. Croke, *Appl. Phys. Lett.* **80**, 1737 (2002).
- [143] L. Wang, and B. Li, *Phys. Rev. B* **74**, 134204 (2006).
- [144] G. Chen, D. Borca-Tasciuc, and R. G. Yang, *Encyclopedia of Nanoscience and Nanotechnology* Vol. 7, pp. 429-459, American Scientific Publishers, Valencia (2006).
- [145] M. V. Simkin, and G. D. Mahan, *Phys. Rev. Lett.* **84**, 927 (2000).
- [146] N. Yang, G. Zhang, and B. Li, *Nano Lett.* **8**, 276 (2008).
- [147] B. Li, L. Wang, and G. Casati, *Phys. Rev. Lett.* **93**, 184301 (2004).
- [148] J. H. Lan, and B. Li, *Phys. Rev. B* **74**, 214305 (2006).

Bibliography

- [149] G. Zhang, Q. Zhang, C. -T. Bui, G. -Q. Lo, and B. Li, *Appl. Phys. Lett.* **94**, 213108 (2009).
- [150] G. Zhang, Q. -X. Zhang, D. Kavitha, and G. -Q. Lo, *Appl. Phys. Lett.* **95**, 243104 (2009).
- [151] S. G. Volz, and G. Chen, *Appl. Phys. Lett.* **75**, 2056 (1999).
- [152] D. Donadio, and G. Galli, *Phys. Rev. Lett.* **102**, 195901 (2009).
- [153] D. Donadio, and G. Galli, *Nano Lett.* **10**, 847 (2010).
- [154] J. L. Feldman, M. D. Kluge, P. B. Allen, and F. Wooten, *Phys. Rev. B* **48**, 12589 (1993).
- [155] J. L. Feldman, and N. Bernstein, *Phys. Rev. B* **70**, 235214 (2004).
- [156] M. Park, M. Kim, J. Joo, K. Kim, J. Kim, S. Ahn, Y. Cui, and J. Cho, *Nano Lett.* **9**, 3844 (2009).
- [157] C. B. Vining, *Nature* **451**, 132 (2008).
- [158] J. Chen, G. Zhang, and B. Li, *Nano Lett.* **10**, 3978 (2010).
- [159] J. Xiang, W. Lu, Y. J. Hu, Y. Wu, H. Yan, and C. M. Lieber, *Nature* **441**, 489 (2006).
- [160] J. Xiang, A. Vidan, M. Tinkham, R. M. Westervelt, and C. M. Lieber, *Nature Nanotech.* **1**, 208 (2006).
- [161] Y. Hu, H. O. H. Churchill, D. J. Reilly, J. Xiang, C. M. Lieber, and C. M. Marcus, *Nature Nanotech.* **2**, 622 (2007).

Bibliography

- [162] J. Chen, G. Zhang, and B. Li, *Phys. Lett. A* **374**, 2392 (2010).
- [163] E. S. Landry, M. I. Hussein, and A. J. H. McGaughey, *Phys. Rev. B* **77**, 184302 (2008).
- [164] Z. Liu, X. Zhang, Y. Mao, Y. Y. Zhu, Z. Yang, C. T. Chan, and P. Sheng, *Science* **289**, 1734 (2000).
- [165] R. Yang, G. Chen, and M. S. Dresselhaus, *Nano Lett.* **5**, 1111 (2005).
- [166] D. P. Sellan, E. S. Landry, J. E. Turney, A. J. H. McGaughey, and C. H. Amon, *Phys. Rev. B* **81**, 214305 (2010).
- [167] Y. Cui, L. J. Lauhon, M. S. Gudiksen, J. Wang, and C. M. Lieber, *Appl. Phys. Lett.* **78**, 2214 (2001).
- [168] F. Qian, Y. Li, S. Gradecak, D. Wang, C. J. Barrelet, and C. M. Lieber, *Nano Lett.* **4**, 1975 (2004).
- [169] S. W. McDonald, and A. N. Kaufman, *Phys. Rev. Lett.* **42**, 1189 (1979).
- [170] J. Chen, J. -C. Cheng, and B. Li, *Appl. Phys. Lett.* **91**, 121902 (2007).
- [171] C. W. Chang, D. Okawa, H. Garcia, A. Majumda, and A. Zettl, *Phys. Rev. Lett.* **101**, 075903 (2008).
- [172] J. X. Cao, X. G. Gong, J. X. Zhong, and R. Q. Wu, *Phys. Rev. Lett.* **97**, 136105 (2006).